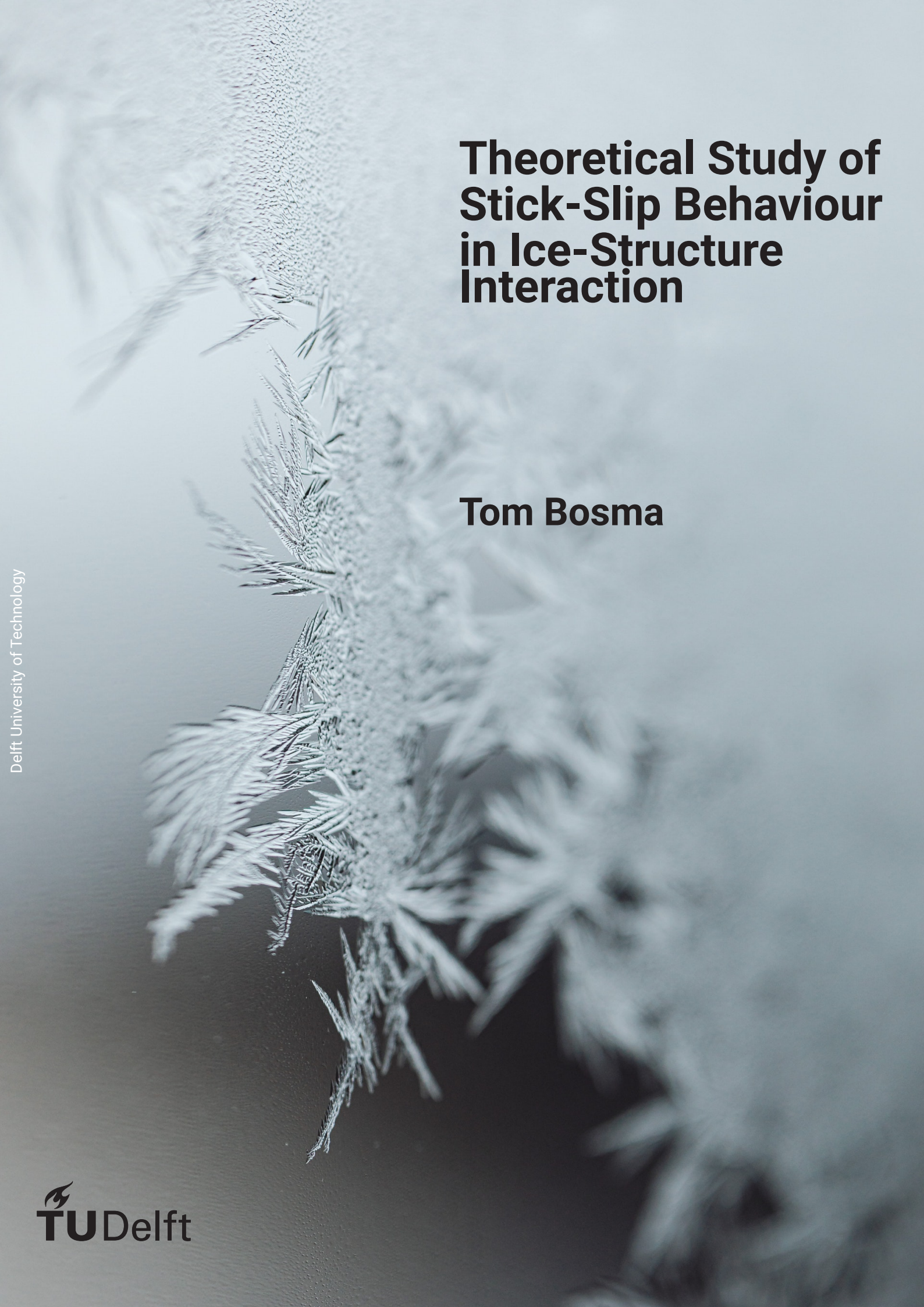

Theoretical Study of Stick-Slip Behaviour in Ice-Structure Interaction

Tom Bosma

Delft University of Technology

TU Delft

Theoretical Study of Stick-Slip Behaviour in Ice-Structure Interaction

by

Tom Bosma

To obtain the degree of Master of Science
at the Delft University of Technology

Section Offshore Engineering (CEG)

Student number:	4440471
Project duration:	May 2021 - January 2022
Graduation Committee:	Andrei Metrikine (chair)
	Jeroen Hoving (daily supervisor)
	Cody Owen
	Marnix van den Berg

TU Delft

Executive Summary

Structures built in lakes and rivers or at sea are under huge forces induced by ice. These cause friction at the ice-structure interface that may pose a threat to the structural integrity of the construction. For the detailed design and realisation of structures in such regions an understanding is required of this friction process. The friction process at the ice-structure interface is driven by a phenomenon called the stick-slip phenomenon, where during stick mode the structure and the ice move simultaneously with the same velocity, and during slip mode the ice and structure interface slide over one another. This phenomenon has been observed and researched extensively, yet the corresponding static and kinetic friction coefficients reported show a wide range and the relation between the involved parameters and the friction coefficients is inconclusive. The most common theory used in describing general friction processes is Coulomb's Law of Friction. This thesis aims to determine whether and when ice-structure interaction can or cannot be described by Coulomb's Law of Friction in particular cases.

For this graduation project, first an analysis of several test set-ups was carried out to determine which set-up was best suited for experiments with stick-slip behaviour. The chosen test set-up consists of a one-dimensional rotating conveyor belt made from sandpaper on which an ice sample would be placed. This sample would be held in place by four springs attached to the back and front of the sample. This would allow the ice sample to move over the rotating belt, but remain relatively in its place. This would enable to the ice to displace in one direction, the direction of the rotating conveyor belt. This test set-up would be compact and it would be easy to switch the belt or ice sample if they had deteriorated too much. However, the use of a 1D conveyor belt prohibits construction materials such as steel or concrete to be used. Using sandpaper with similar roughness as concrete or steel would serve as a substitute to overcome this problem.

Ultimately, it proved to be impossible to realise the set-up and the focus of this thesis switched towards modelling the two-dimensional stick-slip behaviour based on data from previous research. For this a three degree of freedom (3DOF) model was created. As the forces exerted by the springs on the mass act under an angle that is depending on the position of the mass four different approaches were tested to see how this angle could best be incorporated. Furthermore, the friction force acting on the ice-structure interface was modelled using the friction coefficients found by previous research, and using two different approaches to find out whether the friction force should be modelled using the relative sliding velocity at the interface or not. It proved that the angle between the springs' original position and it's instantaneous position should be updated every step during slip mode, and that the friction force should be modelled using the relative sliding velocity. Both are cause for higher computational time. When validating this model against the experimental data it was found that friction coefficients were overestimated substantially for the 3DOF model. Using this the 3DOF model was updated and it was found that it now matches with the experimental data.

After analysing the output of the model, it was found that the kinetic friction coefficients are now in the range of 0.05-0.11 for the used parameters (mass 0.67 kg – 2.03 kg, slab velocity 0.15 m/s – 0.82 m/s, stiffness 20.17 N/m – 68.22 N/m). Also, the friction coefficients show a linear dependency with mass, and an slight inverse linear relationship with the slab velocity. Furthermore, with a low stiffness varying friction coefficients were found when varying the slab velocity, but when increasing the stiffness the friction coefficients converge and this variation decreases. Although further improvements can be made to create a better model, in general it is concluded that under the made assumptions, the 3DOF model describes the two-dimensional behaviour well, and shows how research into friction can be carried out while still using construction materials in an experimental set-up.

List of Figures

List of Tables

Contents

Chapter 1

Thesis Introduction

In the arctic regions structures built at sea or in rivers and lakes experience huge forces and stresses induced by ice. These cause friction at the ice-structure interface that the structures have to withstand. In Figure 1.1 such a structure can be seen. This mechanism of ice sliding against a structure has been observed for years, and a lot of research has been dedicated to understand this friction process. However, this process is not fully understood yet. This thesis research is a contribution to that, and aims to answer whether the underlying theory that is used in various research, is actually correct to assume, or whether there may be other theories to describe ice-structure friction.

In Section 1.1 the relevance and scope of this research is described. It gives a small overview of what has been done so far. In Section 1.2 the problem that this thesis focuses on is elaborated on, and in Section 1.3 the objectives of this research are described. In Section 1.4 the approach to answer the problem is stated. In Section 1.5 the outline of this thesis is described.

Figure 1.1: Ice pushing against bridge pillar

1.1 Scope & Relevance

Over the past decades a lot of research has been conducted in describing the friction process occurring when ice and structures come into contact with each other. Most researchers agree that the normal force applied on the interface has significant impact on the occurring friction force along the sliding plane. Some assume that ice-structure friction can be described by Coulomb Friction, and that a friction coefficient can relate the normal force to the friction force. It has been shown that this coefficient of friction of ice-structure interaction varies significantly as can be seen by the scatter visible in Figure 1.2a (Nakazawa, 1986). Also, in Figure 1.2b the range in which certain friction coefficients can be found is rather large. The static friction coefficient for uncoated steel according to Møen, Høiseth, Leira, and Høyland (2015) is around 0.13 (1.2b), whereas for the same temperature, ice sample diameter and normal stress the static friction coefficient is ranging from 0.2-0.3 according to (Nakazawa, 1986) (Figure 1.2a). Though the Figures 1.2a and 1.2b only account for two studies it clearly indicates that there is a lack of coherence between what researchers find. It gives rise to the question whether or not the friction of ice on other materials can be described with the use of one single coefficient of friction. More on that in Section 1.2.

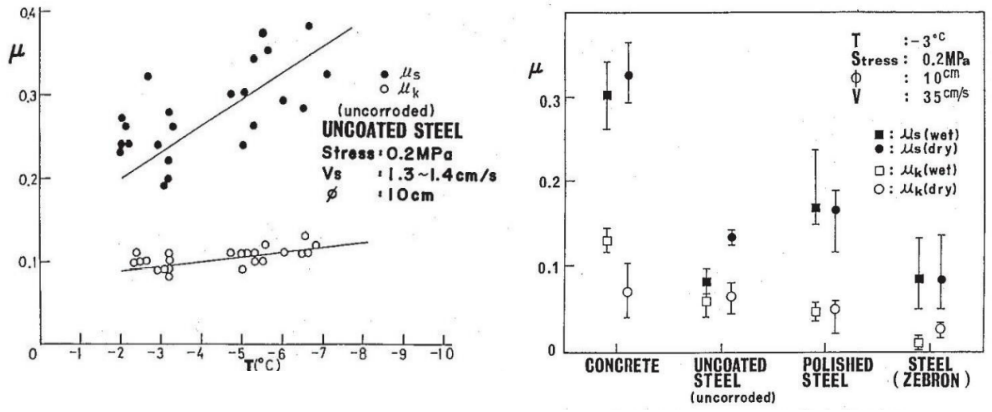

(a) (Nakazawa, 1986) (b) (Møen et al., 2015)

Figure 1.2: (a): Kinetic and Static COF for Ice-Steel interaction, (b): Kinetic and Static COF for 4 different materials interacting with ice

One of the studies carried out into better understanding the friction process occurring in ice-structure interaction was the research carried out by Nuus (2018). She performed experiments with an ice sample on a rotating disk made of concrete, see Figure 1.3. This ice sample was held in place with the use of four springs attached in parallel to the transverse motion (x-direction) of the ice block allowing it to show stick-slip behaviour. By placing the ice sample on the outer edge of the rotating disk it was assumed that the ice sample would only move back and forth in one-direction. This proved to be not true, and excitations in radial direction (y-direction) as well as rotations were found. After examining the data it was found that the ice sample rotates as a consequence of the rotation of the underlying disk. It was unclear to what extent this 2D behaviour only occurred because of the rotation of the disk, or to what extent this behaviour could also be attributed to the heterogeneity of the concrete interface, or that it was noise in the measurement equipment that caused this. Hence, no conclusive answer could be given (Nuus, 2018). One of the recommendations of Nuus (2018) was that if a test set-up was to be designed as such that it would only show 1D behaviour, and not the 2D behaviour that she found, the identification of the friction coefficients could be improved.

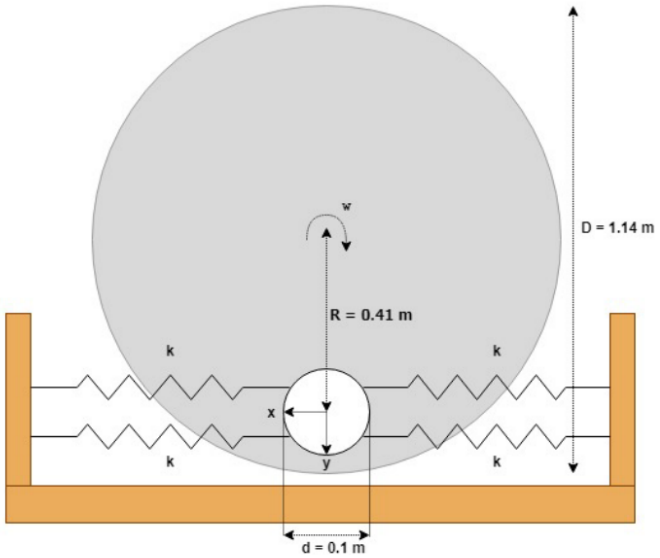

Figure 1.3: 2D Test Set-up as used by (Nuus, 2018)

1.2 Problem Statement

When two surfaces, one of ice and one of (construction) material, interact with one another friction occurs. The focus of this thesis is to better understand the physics behind this process, and the way this process is modelled. As of yet there is no conclusive relation between ice friction and all parameters involved, some being (among others): temperature of ice and surroundings, roughness of the structure material, pressure on the ice, the relative velocity at which one plane slides along the other, just to name a few. In addition, ice is a heterogeneous and anisotropic natural material, which makes the ice characteristics hard to predict.

Regardless of all the different parameters involved research so far has tried to describe ice-structure friction with a single coefficient static friction and one for kinetic friction, as according to Coulomb's Law of Friction, rather than splitting it up and determine a friction coefficient per parameter. So far, it is uncertain to what extent this generally accepted law is the best way to describe, and/or account for, friction in ice-structure interaction depending on the particular situation considered.

The efforts Nuus (2018) lead to friction coefficients determined with a 1 degree of freedom model that was fitted with the 2D data that she obtained from her experiments. It is unclear if this identification of coefficients of friction as accurate enough to properly describe the ice-structure friction.

1.3 Objectives

Based on the experimental results found by Nuus (2018) there are two options. The first option would be to focus on the 1D friction coefficients and design a test set-up that enables to better define the ranges of Coulomb friction coefficients. After that experiments could be carried out with this test set-up and the results could be compared to the results found by Nuus (2018). By focusing on this option the recommendation of Nuus (2018) is adhered to. The second option would be to develop a 2D numerical model that is an improved version of the 1D model that Nuus (2018) already created. The validation of the developed 2D model would be carried out using the 2D experimental data from Nuus (2018). Nuus (2018) already developed a 1DOF model and used 2D experimental data to determine the Coulomb friction coefficients.

In the beginning of this thesis the first option was chosen as the main objective of this study. However, the realisation of the designed test set-up took too long, and it was decided to switch to the second option. Nevertheless, before the switch was made a test set-up was already designed, and so this part remains part of the progress and therefore this thesis. That is why this part of the work is presented in this report. The main objective has therefore become twofold:

1. Define and design what theoretically would be the best 1D test set-up for 1D ice-structure friction.

2. Develop a 2D numerical model to identify the ranges of Coulomb friction coefficients that best mimic the 2D experimental results of Nuus (2018).

1.4 Approach

First the state-of-the-art research on ice-structure friction is reviewed. With this an overview of possible 1D test set-ups was created to identify the best possible test set-up given the boundary conditions of the available lab and the dynamics involved in ice-structure friction. This review concludes the objective about the identification of the best test set-up to determine the friction coefficient. Because the realisation of the test set-up took too long the focus of this thesis was shifted from experiments towards modelling. Nuus (2018) carried out an experiment that had similarities to the experiment that was to be conducted in this research. That experiment led to 2D behaviour of the ice sample under frictional sliding loading. To analyse this a 2D numerical model was set up with three degrees of freedom (3DOF). This 3DOF model concludes the second objective about the design of a mathematical model. This model is then also validated with the data provided by Nuus (2018) and a parameter study was done to assess the dependency of the friction on the influencing parameters.

1.5 Thesis Outline

The state-of-the-art research is presented in Chapter 2. In Chapter 3 the possible test set-ups are described, discussed and assessed based on criteria mentioned. Also, the test plan is described in this Chapter. The 3DOF model that applies to the experiment conducted by Nuus (2018) is described in Chapter 4 including a verification and validation. Chapter 5 presents the sensitivity analysis and how sensitive the modelled friction is to the involved parameters. In Chapter 6 the discussion of this research is given, and in Chapter 7 the conclusions and recommendations are presented.

Chapter 2

State-of-the-art Research Into Ice-Structure Friction

In this Chapter the state-of-the-art research is presented which pose as a framework in which the findings of this thesis should be seen. The Chapter starts on a general high level overview and ends in depth on the small scale influence of individual parameters. An introduction to abrasion due to ice loading is presented in Section 2.1. Section 2.2 describes the four different ice friction regimes, *dry friction*, *boundary friction*, *mixed friction* and *hydrodynamic friction*, that are occurring in ice-structure interaction. Sections 2.3 and 2.4 elaborate on the processes at work when the ice slides (Section 2.3) and when the ice is not sliding (Section 2.4). The alternation of sliding and not sliding, called the Stick-Slip phenomenon, is described in Section 2.5, along with models that mathematically describe this behaviour. In Section 2.6 the parameters of main influence on the ice-structure friction (roughness, normal force and relative sliding velocity) are discussed.

2.1 Abrasion due to ice loading

Ever since offshore constructions were realised in seas that frequently saw ice floating on its surface the abrasion of the building materials has been observed, and that abrasion was caused by friction. This abrasion process has been topic of many studies. The aim was to clarify which parameters play a role in this, but nowadays the process is far from completely understood.

One of the first to contribute to understanding this process were Itoh et al. (1988). They discovered that the abrasion of concrete could well be simulated with shearing apparatus. Furthermore, they concluded that the wear rate mainly depends on the temperature of the ice and the contact pressure on the ice-concrete interface. The other parameters they varied were the relative sliding velocity, compressive strength of the concrete and the aggregate type of the concrete. In addition, they found that surface treatment, such as resin mortar lining, reduce the friction between the structure and ice and is therefore very effective against wear. Lastly, the process of abrasion of concrete without any surface treatment can be divided into three stages:

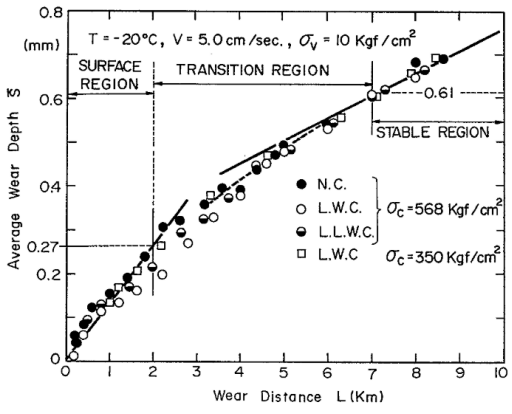

Figure 2.1: Relationship between wear distance and average wear depth (Itoh et al., 1988)

- Surface region; abrasion only occurs on the cement paste on the surface of the concrete.
- Transition region; abrasion is observed on the coarse aggregate, which is gradually becoming exposed.
- Stable region; abrasion of the coarse aggregate occurs over the whole surface.

The three stages can be observed in Figure 2.1. Clearly, this division in three stages is irrespective of the type of aggregate (indicated with the different squares and circles) and compressive strength (Itoh et al., 1988).

2.2 Ice Friction Regimes

When monitoring abrasion occurring in ice friction some literature has defined four different friction regimes that can be observed: dry friction, boundary friction, mixed friction and hydrodynamic friction (Kietzig et al., 2010). The Subsections 2.2.1 - 2.2.4 elaborate on the aforementioned concepts and when they appear.

2.2.1. Dry Friction

Dry friction occurs when two surfaces slide over one another without any kind of lubricating layer. Such a surface is never completely flat, but consists of tiny valleys and asperities. When two or more asperities of the different surfaces make contact adhesive bonds may be formed between them. This depends on the kind of materials that are touching, some materials form adhesive bonds, and some don´t. If either of the surfaces slide with respect to the other the bonds are sheared leading to a frictional force. Under atmospheric conditions and the existing temperatures on earth, the type of friction that is 100% Dry Friction can hardly exist. Even at very low temperatures that occur on earth a thin lubricating layer occurs between the sliding surfaces Kietzig et al. (2010). Bowden and Hughes (1939) showed that this lubricating layer exists for temperatures higher than -140 °C. So for Dry Friction to occur on earth the temperature should be at least lower than -140 °C.

Dry friction is often referred to as Coulomb friction (Kietzig et al., 2010). In this theory the friction coefficient is defined as described in Equation 2.1. It also states that this coefficient is independent of relative sliding velocity, meaning that the velocity at which two planes slides over each other has no influence on the occurring friction. More about the relative sliding velocity in Subsection 2.6.3.

$$\mu_{friction} = \frac{F_{friction}}{F_{normal}} \tag{2.1}$$

2.2.2. Boundary Friction

The second friction regime is boundary Friction on ice, and is characterised by a small film on the interface that serves as a lubricating layer. It occurs when the following conditions are met everywhere in the contact zone:

$$T < T_m \qquad \& \qquad h << R \tag{2.2}$$

Thus, the temperature (T) in the contact zone is everywhere smaller than the melting temperature (T_m), and the thickness of the lubricating layer (h) is far smaller than the surface roughness (R). Because of this lubricating layer the occurring friction is less compared to that occurring during dry friction (Kietzig et al., 2010).

2.2.3. Mixed Friction

Mixed friction is slightly different from boundary friction as described in subsection 2.2.2 because now in some points in the contact zone the temperature (T) rises above the melting temperature (T_m). The other condition mentioned in subsection 2.2.2 remains true, though the height of the layer is somewhat higher with respect to height of the asperities:

$$\text{at some points}: \qquad T > T_m \qquad \& \qquad h < R \tag{2.3}$$

In this friction regime the sliding interface partly supported by the lubricating layer and partly by the surface asperities. The larger the lubricating layer the lower the adhesion between the solids. With the increasing height of the lubricating layer also comes a rise in capillary bridges between asperities as can be seen in Figure 2.2. These bridges act as bonds between the surface and the slider. This results in a drag force being exerted on the slider, but only along the sliding plane: the capillary bridges do not carry the applied load. This latter phenomenon remains yet to be described by a model to be able to determine the exact contribution to the total frictional force (Kietzig et al., 2010).

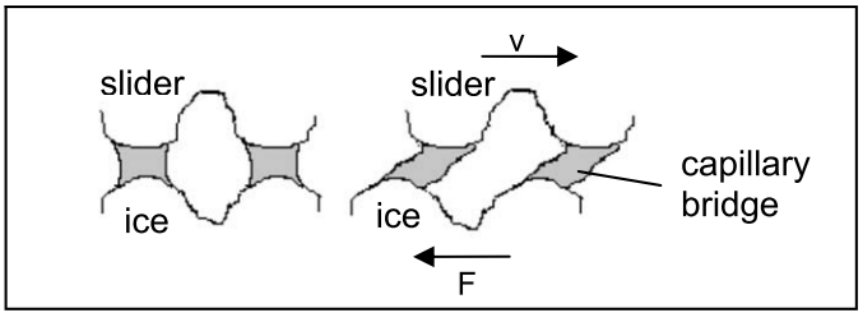

Figure 2.2: Capillary Bridges between Asperities (Kietzig et al., 2010)

2.2.4. Hydrodynamic Friction

The fourth and final friction regime, is the hydrodynamic friction regime. Herein, the temperature (T) is above the melting temperature (T_m) everywhere in the contact zone. In some literature this type of friction is referred to as hydraulic friction or fluid friction Furthermore, the lubricating layer is greater than the height of the asperities:

$$\text{at all points}: \qquad T > T_m \qquad \& \qquad h > R \tag{2.4}$$

In this regime the lubricating layer carries the applied load. This could lead to some lubricants leaking out if the applied load is too high; the lubricant is squeezed out. Because there is no contact between the opposing asperities no load is carried by the asperities, and so no solid-solid adhesion occurs. This means that the frictional force that is mobilised only depends on the shear strength of the lubricating layer (Kietzig et al., 2010).

An overview of the friction regimes in which a lubricant layer is involved (boundary, mixed and hydrodynamic friction) can be found below in Figure 2.3. Apparently the optimal friction coefficient lies in the mixed friction regime, meaning that a mixture of solid-solid adhesion between the asperities and the presence of the lubricant layer are both needed to have low friction (Kietzig et al., 2010).

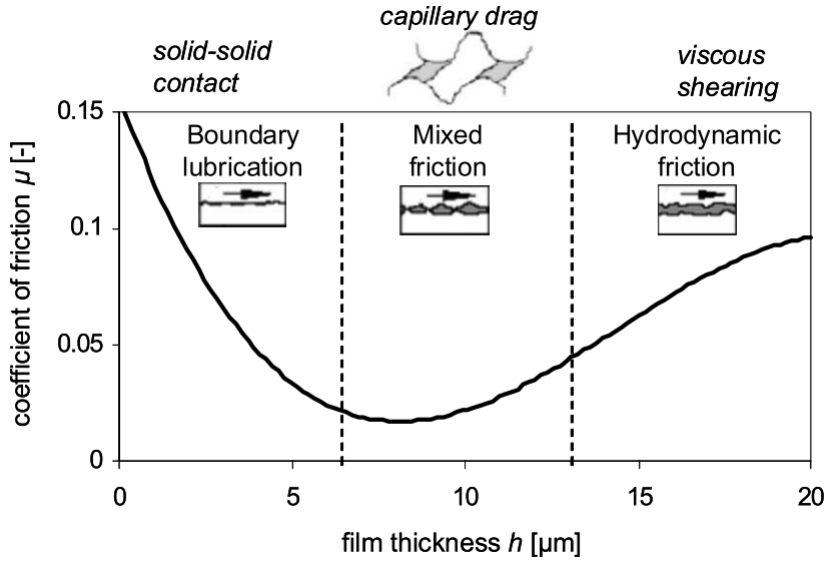

Figure 2.3: Overview Friction Regimes and the corresponding coefficient of friction (Kietzig et al., 2010)

2.3 Melting Due To Frictional Heating

In the previous section the four different ice friction regimes have been discussed. These regimes are influenced by processes that occur when there is relative sliding occurring. The first of such processes to be discussed is the melting due to frictional heating. For long it has been said that melting by applied pressure resulted in the lubricant layer (Reynolds, 1901). Nevertheless it was reported that few measurements of any sort have been made available to either prove or disprove this statement (Bowden & Hughes, 1939). Furthermore, they go on to show calculations that show that pressure alone cannot result in melting. For this to happen heat must be supplied. This heat must come from a source which is at higher temperature than that of the bulk melting temperature. All in all, based on theoretical grounds the pressure-melting theory cannot be ruled out (Bowden & Hughes, 1939). In addition to heating due to frictional heating another source of heating is due to the environmental conditions in which the temperature rises. The latter is assumed common knowledge and hence, not further discussed in this literature review.

Melting of ice is a phase transition where physical quantities like mass density and shear strength change suddenly at the transition temperature. This in turn might lead to a sudden change in the friction coefficient. Nevertheless, Persson (2015) showed that melting does not occur at all contact point simultaneously under friction heating. This means that the change in friction is not abrupt but rapid. Persson (2015) then goes on suggesting this may be a result of the following paradoxical phenomenon: before the first ice starts to melt the friction under ice-structure interaction may be high and high frictional heating may occur resulting in the melting of some ice. If this layer forms the friction becomes lower (see Subsection 2.2.4, Figure 2.3). This in turn leads to lower frictional heating and thus the water layer can freeze again. Another alternative Persson (2015) suggests is that heat-softening of the ice may be formed. This results in a layer of amorphous-like ice of which the shear strength decreases continuously as the ice surface temperature reaches the bulk melting temperature (Persson, 2015).

2.4 Static Strengthening

The second process to be discussed occurs during no relative sliding: static strengthening. Over the years numerous experiments have been conducted into the interaction between ice and structures when in contact. Lishman, Sammonds, and Feltham (2011) showed in recent research that the coefficient of friction increases with time. This was found when applying a low normal stress of 50 kPa for 10^3 s on an ice sample at -10 °C after sliding at a velocity of 10^{-4} m/s. It was found that this holding time more than doubles the static friction (Lishman et al., 2011). This effect, called static strengthening, was observed more closely by Schulson and Fortt (2013) when performing Slide-Hold-Slide tests, or SHS tests. They defined it as the difference between the kinetic and static friction coefficient: $\Delta\mu = \mu_s - \mu_k$ (Schulson & Fortt, 2013). These SHS tests were performed on both first year sea ice and freshwater ice and carried out with the use of a double shear device. The results can be seen in Figure 2.4. Here μ is defined as the ratio τ_p/σ_n, where τ_p is the peak stress at which the sliding resumes after the holding time, and σ_n is the normal stress of 60 kPa applied to the ice sample. The tests were carried out at sliding velocities V_s of 10^{-4} m/s, 10^{-5} m/s, 10^{-6} m/s.

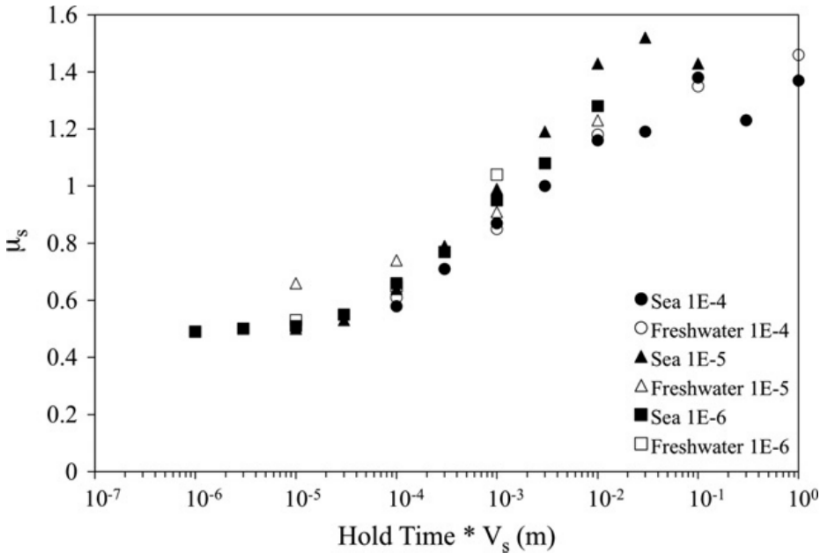

Figure 2.4: Coefficients of static friction versus holding time (Schulson & Fortt, 2013)

Static strengthening begins to be detected once the holding time exceeds a certain threshold t_t. The threshold period decreases with increasing velocity, from $t_t \approx 30$ s at $V_s = 10^{-6}$ m/s to $t_t \approx 3$ s at $V_s = 10^{-5}$ m/s. At the highest velocity a threshold was not detected in the shortest time explored, however, upon extrapolating to zero hardening we expect that $t_t \approx 0.3$ s at $V_s = 10^{-4}$ m/s. Furthermore, static strengthening increases with holding time by a factor of "$\beta * log_{10}(t_h)$", where $\beta = 0.30 \pm 0.03$ (independent of velocity) and t_h is the holding time. The effect of the holding time t_h appears to have an upper limit, and this upper limit appears to decrease with increasing velocity. Lastly, it appears there is little to no difference in the effect of static strengthening between sea ice and freshwater ice, under the conditions of the conducted experiments.

2.5 Stick-Slip Phenomenon

The last process to be discussed is a mixture of relative sliding and relative standstill, and is known as the stick-slip phenomenon. In Section 2.4 the difference between static and dynamic friction has been mentioned. The process of ice sliding, stopping, and resume sliding is called stick-slip (Fiorio et al., 1997; Schulson & Fortt, 2013). The Slide-Hold-Slide tests that were carried out by Fiorio et al. (1997) showed three distinct stages:

1. Adhesion between the ice and the concrete leading to a stationary phase, which is called stick.
2. During stick the tangential stress at the interface increases until the ice-structure bond fails.
3. The ice-structure bond breaks and the ice moves relative to the structure. This dynamic phase is referred to as slip.
4. During slip the tangential stress decreases and so will the relative sliding velocity. Once they become zero the ice resumes sticking to the structure surface, and the interaction is in stage 1 again.

This process keeps repeating itself leading to what is referred to as the stick-slip regime. See Figure 2.5 for a visualisation of the process. Here the tangential stress curve shows a fraction of a saw-tooth pattern. Just after the peak the tangential stress drop. During this drop the ice moves in this case leading to a small negative displacement displayed in the upper curve.

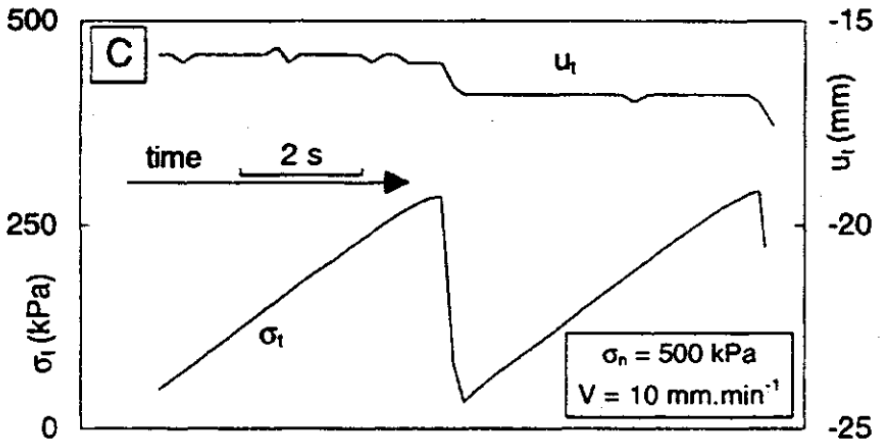

Figure 2.5: Tangential stress σ_t and displacement u_t observed during stick-slip phases. Horizontal axis represents the time lapsed in two cycles (Fiorio et al., 1997)

Stable stick-slip behaviour is influenced by the relative velocity of ice with respect to the structure, the roughness of the structure, and the normal stress of force on the sliding interface (Fiorio et al., 1997). For a low roughness, it was found that relatively high normal stress lead to a stable stick-slip regime. In addition, the velocity was of no influence on the occurrence of stick-slip, but it did influence the period of the stick-slip phases. For a high roughness, stable stick-slip behaviour was only found when both the relative velocity and the normal stress were high. More on the influence of different parameters in section 2.6. Under certain circumstances the slip phase is longer compared to Figure 2.5. This behaviour can be seen in Figure 2.6 where 10 cycles of stick-slip behaviour is shown (Fiorio et al., 1997). Here, constant load tests were carried out by prescribing a normal stress on an ice sample. When the tangential stress reached the prescribed load the displacement of the structure was started at a set velocity. When the end of it´s stroke was reached the movement of the structure was reversed to get back to the initial position. Hence, the graph for the tangential stress flips around the x-axis. In addition, the calculated friction coefficients have been plotted in Figure 2.6. It can be seen that the friction coefficient increased during the initial cycles and becomes stable over time. Additionally, just after the peak, so during slip, the tangential stress decreases to what is referred to as a dynamic friction stress. This indicates that there is a clear distinction between static friction and dynamic friction, something that was to be expected given Coulomb´s Law of Friction (Marghitu, 2001).

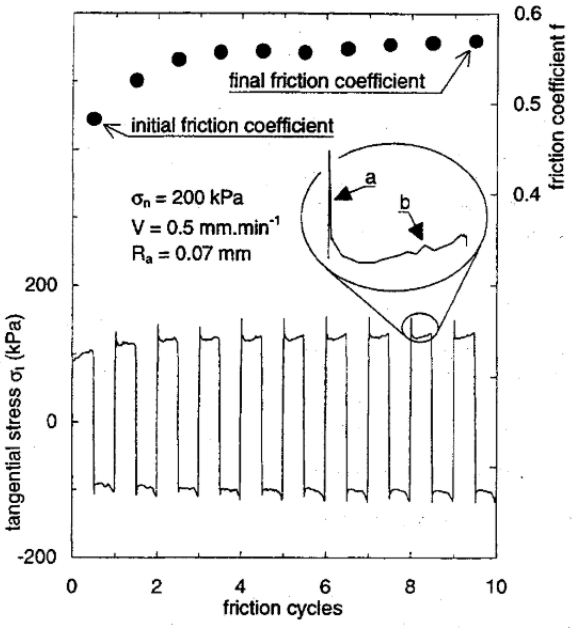

Figure 2.6: Tangential stress and calculated friction; a: stick peak and b: local perturbation of friction by geometric defect of the structure (Fiorio et al., 1997)

2.5.1. Modelling Stick-Slip Behaviour, 1DOF

The behaviour of stick-slip can be modelled as a 1 degree of freedom (or 1DOF) system with a dry friction element included (see Figure 2.7), and hence dry friction is assumed in the model. The dry friction element creates the division between the stages of stick and slip. During stick, the system behaves like a horizontal linear mass-spring system and the dry friction element is not activated. Once the force in the spring equals or exceeds a certain threshold value of the friction force, here called F_{dyn}, the dry friction element is activated. What follows is the slip stage is described in Section 2.5. In this stage the frictional force F_r is equal to the threshold value of the dry friction element. The two stages can be numerically described by the following state equations (Leine et al., 1998):

Stick:

$$\begin{bmatrix} \dot{y}_1 \\ \dot{y}_2 \end{bmatrix} = \begin{bmatrix} v_b \\ 0 \end{bmatrix} \tag{2.5}$$

$$F_r = k * y_1 \tag{2.6}$$

Slip:

$$\begin{bmatrix} \dot{y}_1 \\ \dot{y}_2 \end{bmatrix} = \begin{bmatrix} y_2 \\ -\frac{k}{m} y_1 + \frac{F_r}{m} \end{bmatrix} \tag{2.7}$$

$$F_r = F_{dyn} \tag{2.8}$$

Where y_1 and y_2 represent x and $\dot{x}$ respectively in Figure 2.7, vb is the belt velocity.

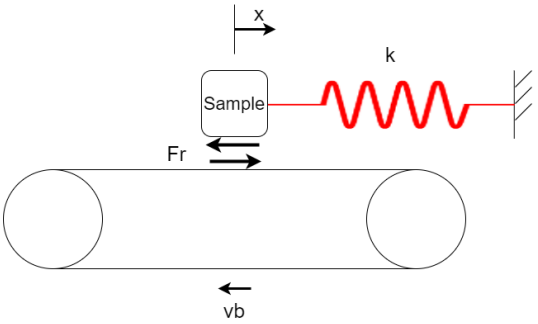

Figure 2.7: 1DOF model with dry friction: sample rests on the belt, and the belt is rotating with velocity vb causes friction on the sample-belt interface

For this system a full cycle of the response is shown, so at $\dot{x} = 0.2$ m/s the sample is in stick phase, and when the velocity $\neq 0.2$ m/s the sample is in slip phase. This is considered to be a 1D-phenomenon as the mass only moves back and forth in one direction.

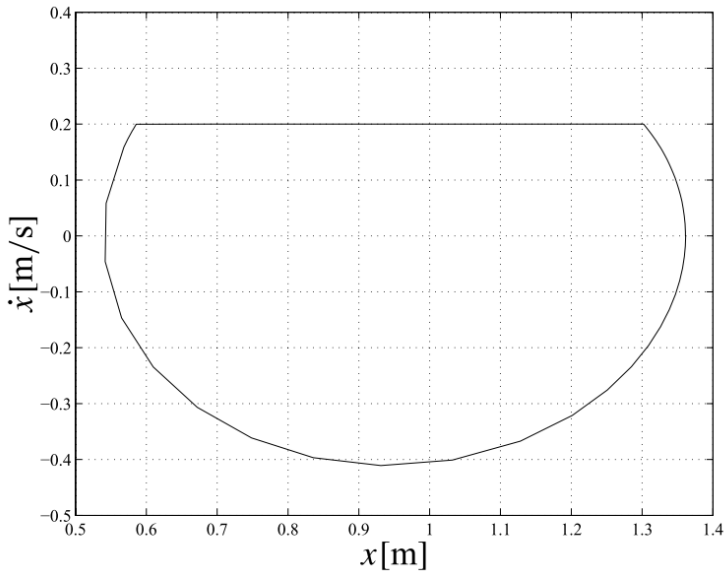

Figure 2.8: Phase portrait of 1DOF behaviour (Leine et al., 1998)

2.5.2. Modelling Stick-Slip Behaviour, 2DOF

In Subsection 2.5.1 it was assumed that the ice sample only has one degree of freedom, along the axis parallel to the conveyor belt. This behaviour would be exactly described by the model presented in Subsection 2.5.1 if the physical situation were ideal. Meaning, the friction force applied on the sample would be equal at every point across the sliding interface. Naturally, the physical situation is far from ideal which means that the ice sample will be able to rotate around a certain point. For now, we assume that point of rotation to be the geometric centre of the sample. Leine et al. (1998) propose a model in which this 2 degree of freedom (2DOF) behaviour can be numerically described. The visual representation of this model in the xy-plane can be seen in Figure 2.9. The state equations now read (Leine et al., 1998):

Stick:

$$\begin{bmatrix} \dot{y}_1 \\ \dot{y}_2 \\ \dot{\Phi}_1 r \\ \dot{\Phi}_2 r \end{bmatrix} = \begin{bmatrix} v_b \\ 0 \\ 0 \\ 0 \end{bmatrix} \tag{2.9}$$

Slip:

$$\begin{bmatrix} \dot{y}_1 \\ \dot{y}_2 \\ \dot{\Phi}_1 r \\ \dot{\Phi}_2 r \end{bmatrix} = \begin{bmatrix} y_2 \\ -\frac{k}{m} y_1 + \frac{F_r}{m} \\ \Phi_2 r \\ -\frac{k_t}{J} \Phi_1 r + \frac{F_r r^2}{J} \end{bmatrix} \tag{2.10}$$

Where y_1, y_2, $\Phi_1 r$, and $\Phi_2 r$ are x, $\dot{x}$, φr, and $\dot{\varphi} r$ respectively in Figure 2.9. The friction force F_r is now the same in both states:

$$F_r = \frac{kx + k_t \frac{m}{J} \varphi r}{1 + r^2 \frac{m}{J}} \tag{2.11}$$

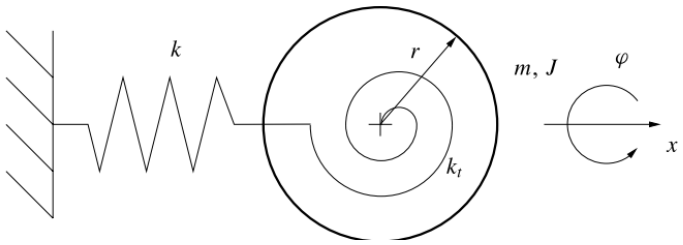

Figure 2.9: 2DOF model with dry friction (Leine et al., 1998)

In Figure 2.9 Leine et al. (1998) represented the sample as a circle, whereas this research will be based on square-shaped sample. Nevertheless, it is worthwhile to observe how such a system behaves. This is shown by Leine et al. (1998) in a phase portrait, which is displayed in Figure 2.10 below.

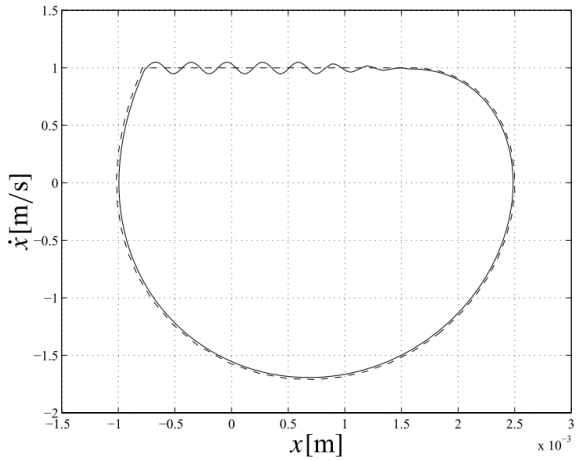

Figure 2.10: Phase portrait of 1DOF and 2DOF behaviour. The dashed line represents the 1DOF behaviour and the full black line represents the 2DOF behaviour (Leine et al., 1998)

For both systems a full cycle of the response is shown, so at $\dot{x} = 1$ m/s the sample is in stick phase, and when the velocity $\neq 1$ m/s the sample is in slip phase. Most striking is that in the 2DOF behaviour the sample's velocity swings about the belt velocity, in comparison to the 1DOF behaviour.

2.6 Influence Parameters On Ice-Structure Friction

All occurring processes have been discussed in the previous sections. This Section zooms in on the parameters involved in ice-structure interaction, and describes in short what the latest findings are on the influence of parameters surface roughness (Subsection 2.6.1), normal force (Subsection 2.6.2) and relative sliding velocity (Subsection 2.6.3) separately. These parameters will be varied in this research. A more thorough elaboration on which parameter is varied can be found in Section 3.4.1.

2.6.1. Roughness

Already in 1699 Amonton stated that roughness plays a pivotal role in friction (Dowson, 1998), and a number of studies has already established the nature of the correlation between roughness and friction (Calabrese et al., 1980; Ducret, Zahouani, Midol, Lanteri, & Mathia, 2005). However, it is far from certain as to what the exact relation is between friction of ice and the roughness of the structure. Generally, it is accepted to state that with increasing roughness the real surface contact area increases as well. More and more asperities interlock leading to a higher wear rate and overall, more friction. In addition, with more asperities interlocking the lubricating film, as described in Section 2.2, becomes thinner (Kietzig et al., 2010).

2.6.2. Normal Force

In literature, it is generally accepted that the coefficient of friction of ice-structure interaction decreases with increasing normal force, at a set relative sliding velocity and temperature (Bäurle et al., 2006; Calabrese et al., 1980; Akkok et al., 1987; Oksanen & Keinonen, 1982). Oksanen and Keinonen (1982) showed that at a temperature of -15°C and relative sliding velocity of 0.5 m/s that the coefficient decreases with increasing normal pressure. However, at a temperature of -1°C the decrease is less obvious. This is shown in Figure 2.11 below. In addition, there seems to be an upper limit as to the influence of a high normal force on the coefficient of friction. Calabrese et al. (1980). showed with experiments consisting of a steel slider and loads above 400 N that the coefficient of friction was entirely independent of the normal force. Note worthy: the independence of the normal force was found in experiments with high load sliders that consisted of high surface energy materials, and the experiments were conducted at relatively high velocities ($v \gtrapprox 0.5$m/s) and temperatures close to the melting temperature (-5°$\lessapprox$ T < 0°C).

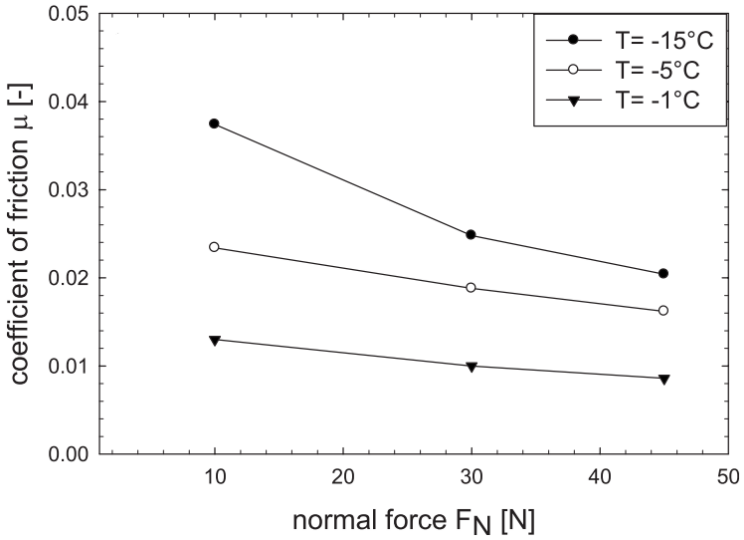

Figure 2.11: Normal force versus coefficient of friction (Kietzig et al., 2010; Calabrese et al., 1980)

2.6.3. Relative Sliding Velocity

Coulomb's Law of Friction states that the relative sliding velocity of the sliding interfaces has no influence on the occurring friction and the friction coefficient. However, this paragraph shows that this does not hold for ice-structure interaction. It was already in 1939 that Bowden and Hughes (1939) concluded based on mathematical derivations that friction against ice decreases when the relative sliding velocity was increased. A couple of decades later Evans et al. (1976). confirmed these findings through experimental and theoretical works. After that, many more studies confirmed these findings, as can be seen below in Figure 2.12. The data presented shows a clear descend with increasing sliding velocity, and a relation with $\mu \propto 1/\sqrt{v}$. The explanation for the mentioned relation lies in the fact that the higher the velocity the more frictional heat is generated, which in turn causes more ice to melt. Hence, the lubrication film is increased in size which results in lower friction along the sliding plane. This is the case in both boundary and mixed friction regimes. In the latter, this only upholds if the drag forces do not outweigh the benefits of a thicker lubricating layer. There is an upper boundary at which a thicker lubricating layer starts to result in a higher coefficient of friction. This increase in both lubricating film and friction happens midway through the mixed friction regime and continues to uphold in the hydrodynamic friction regime. The reason for this being that the drag forces outweigh the benefits of a thicker lubricating layer. The differences in the data presented in Figure 2.12 are caused due to different experimental setups.

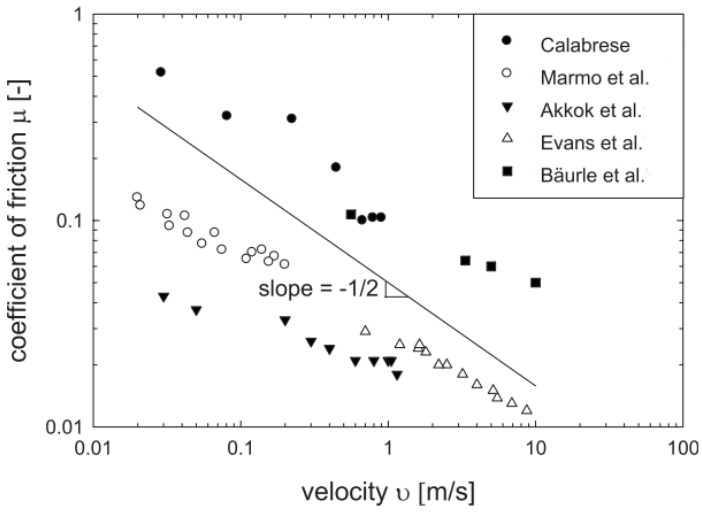

Figure 2.12: Coefficient of friction dependence on relative sliding velocity (enhanced lubrication) (Bäurle et al., 2006; Calabrese et al., 1980; Akkok et al., 1987; Evans et al., 1976; Marmo et al., 2005)

Once the drag forces do outweigh the benefits of a thicker lubricating layer in the mixed friction regime and in the hydrodynamic friction regime the relation, as observed in Figure 2.12, is no longer valid. In fact, the relation is reversed: the coefficient of friction increases with increasing sliding velocity. The relation between the two now scales with $\mu \propto \sqrt{v}$. This relation holds for temperatures close to the melting temperature. In the hydrodynamic friction regime the drag forces are increased because of the shearing of the lubricating layer, which leads to the higher friction. Again, the data presented here show differences among them due to different experimental setups. Also, the start of the increase in friction with increasing sliding velocity heavily depends on the weight and size of the ice, and the temperature and structural materials.

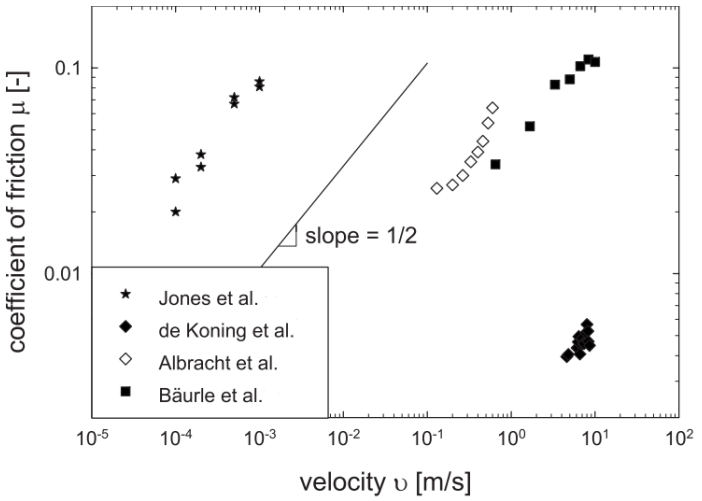

Figure 2.13: Coefficient of friction dependence on relative sliding velocity (Albracht et al., 2004; Bäurle et al., 2006; De Koning et al., 2000; Jones et al., 1994)

Chapter 3

Test Set-up for Identification 1D Ice-Structure Friction Coefficient

In this chapter the 1D test set-ups are discussed. In Section 3.1 possible test set-ups are discussed and assessed. This assessment serves as a rationale to come to the right set-up. This set-up should make it better to understand the friction process and should enable to determine the friction coefficient in ice-structure interaction under given circumstances. Those circumstances will be elaborated on in Section 3.1, and these are translated into the criteria for the assessment of the possible test set-ups. At the end of Section 3.1 the final test set-up will be chosen, and the full construction layout of this test set-up will be described in Section 3.3. It describes both the ideal construction layout, as well as the actual construction layout. The latter being the layout of how the set-up is ultimately to be constructed. Section 3.4 describes the test plan for the identification of the friction coefficient in 1D ice-structure interaction to be used in the experiment, and why these are selected. In Section 3.5 an update is given on the progress of the realisation of the test set-up and why the focus of the thesis shifted from carrying out 1D experiments towards 2D modelling of already existing experimental data.

3.1 Possible 1D Test Set-ups

In this section the possible 1D test set-ups are discussed. As already stated, the test set-up should make it possible to better understand the friction process of ice-structure interaction. This set-up could be used to generate data that should enable to better determine the coefficient of friction under certain circumstances. Those circumstances are bound by practicalities, such as the Coldroom at the Faculty of Civil Engineering and Geosciences. This Coldroom has a maximum temperature of -20°C and the limited floor space allocated for this experiment. Because of the tight space, a maximum floor space to be occupied by the test set-up is roughly 1 m^2. Other circumstances involve the desired behaviour of the ice-structure interaction process. As the interest lies in researching both static and kinetic friction it means that ice should be able to slide over another object. The dynamics this involves are easiest to be analysed if the motion of the ice relative to the other surface over which it slides is in one direction. This means that the test set-up must enable 1D displacement, and must prevent 2D behaviour as much as possible. And so the main goal of this review of possible test set-ups is to find a test set-up that isolates 1D displacements, as that give best insights into the parameters (see Subsection 2.6) involved in the friction process. This does not mean that 2D test set-ups cannot provide meaningful insights into how a test set-up can be designed, but it remains outside the scope of this Chapter. Furthermore, the 1D test set-up should give proper and constant results to enable a thorough analysis of the friction process. The minimum amount of time needed to conduct a single experiment run is set at 20 s. This minimum amount of time is needed to get enough data to carry out the study of the data.

The set-ups discussed in the following Subsections 3.1.1 - 3.3 are either introduced by the author, or taken from existing research. The assessment of the test set-ups is carried with the following indicators: a '(+)' indicates a positive assessment, a '(-)' indicates a negative assessment and a '(+/-)' indicates a neutral assessment. The set-ups are assessed based on the criteria already mentioned, with the exception of the surrounding temperature. Each criterion has the same weight in the assessment. The possible test set-ups are chosen as such that they at least adhere to this criterion. Theoretically, temperatures lower than -27°C make it impossible to

carry out experiments, as the available coldroom has a temperature limit at -27°C. It is noteworthy that the given test set-ups in this section are not the only test set-ups that one can think of, or that can be found in literature. There are more test set-ups than the three set-ups given in this Section, but to some extent the test set-ups *not* in this Section have similarities with the test set-ups that *are* in this Section. That is why only the following three test set-ups are described.

3.1.1. 1D Set-up With Concrete Caterpillar Belt

The first possible set-up is a set-up with a concrete caterpillar belt, and is visualised in Figure 3.1. The ice sample will be placed on the caterpillar belt, which in turn is stabilised by a railing underneath the belt. It is to prevent the belt from bending downwards, and to keep the sample at a constant elevation. The caterpillar belt should be made of concrete as the friction of ice over concrete best resembles the friction process we're interested in. In fact, any other material that is often used in construction can be used, like steel, but in this case concrete is preferred as it is cheaper. In a caterpillar belt the concrete panels lie on top of each other, but are not fixed to each other. This enables the caterpillar to bend at the left and right end (see Figure 3.1). The weight of the caterpillar will be significant because it is partly made of concrete. This makes it time consuming to change the caterpillar belt with a new belt if the quality of the belt is not sufficient anymore. However, the set-up can be made as such that it does not occupy more than 1 m^2 floor space, which is considered to be compact.

The ice sample will be held in place using springs on either side as indicated in Figure 3.1. The springs hold the ice sample in place, so it does not reach the ends where the ice sample would fall of the caterpillar belt. Furthermore, the springs enable the ice sample to move. These displacements can be tracked with the use of a high speed camera. With the displacements known the friction force occurring on the sliding interface can be retrieved. In addition, a thermal vision camera can be used to measure the temperature at the sliding interface. This can be used to make sure that possible frictional heating does not cause for too high temperature risings.

Although the springs make sure that the ice sample only moves in x-direction, so 1D behaviour, the overlapping of the concrete panels also cause the ice sample to bounce on the concrete panel. This means that the ice sample will also move in z-direction, so the behaviour of the ice sample is 2D ultimately. In addition, the bouncing of the ice sample on the concrete panels causes the ice sample as well as the concrete panels to deteriorate fast during a experiment run. Especially the deterioration of the ice sample is a cause for concern, because to get proper experimental data the ice sample is required to be approximately unscathed.

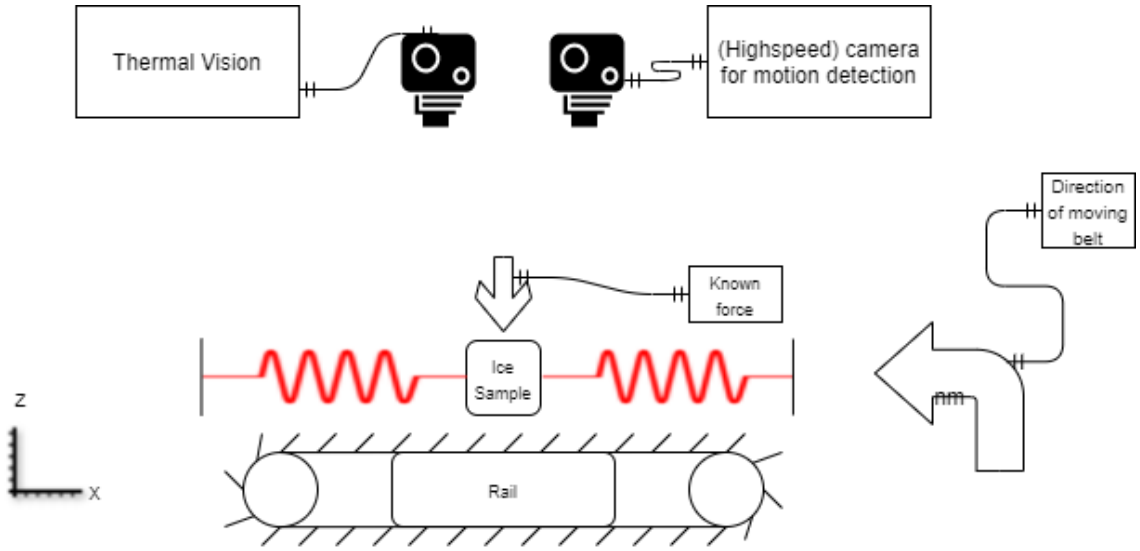

Figure 3.1: Illustration of 1D set-up with concrete caterpillar belt sketched in *xz*-frame

The background colors in Table 3.1 indicate whether this test set-up meets the criteria as described in the introduction of Section 3.1. A green color indicates that the criterion is met, a red color indicates that the criterion is not met, and a orange color indicates that the criterion is only half met. The same indication applies to the colors used in all tables in this Chapter.

Table 3.1: Advantages and disadvantages of 1D set-up with moving concrete caterpillar belt

Test Set-up	Can concrete or steel be used as sliding surface?	Easy to change material/ice?	1D or 2D displacements	Dimensions of experiment
Concrete Caterpillar Belt	Yes, (+)	No, (-)	2D (x and z), (-)	Compact, (+)

3.1.2. 1D Set-up With Sandpaper Conveyor Belt

The second possible set-up is similar to the set-up with the concrete caterpillar belt as discussed in Subsection 3.1.1. Again, the ice sample is placed on a moving belt, and the belt is held in place with a railing. This is illustrated in Figure 3.2. The difference with this set-up is that with this set-up the concrete caterpillar belt is removed, and instead a belt made from sandpaper is introduced. This conveyor belt has the same advantage as the caterpillar as it can bend. Again, with the use of springs this enables the ice sample to only move in x-direction, so 1D behaviour. Because the belt is flat the ice sample will not bounce, as with the caterpillar belt in Subsection 3.1.1, and so the 1D behaviour sustains. Disadvantageous is that the belt cannot be made from construction material like concrete because materials such as concrete cannot bend. To overcome this problem sandpaper with a known roughness similar to concrete or steel can be used to mimic the surface of the concrete. The findings are summarised in Table 3.2.

Again the dimensions of this set-up are of the same size as the set-up discussed in Subsection 3.1.1, and therefore considered to be compact. The same goes for the measuring equipment. These can consist of a high speed camera for tracking of displacements and a thermal vision camera to measure the temperature at the sliding interface.

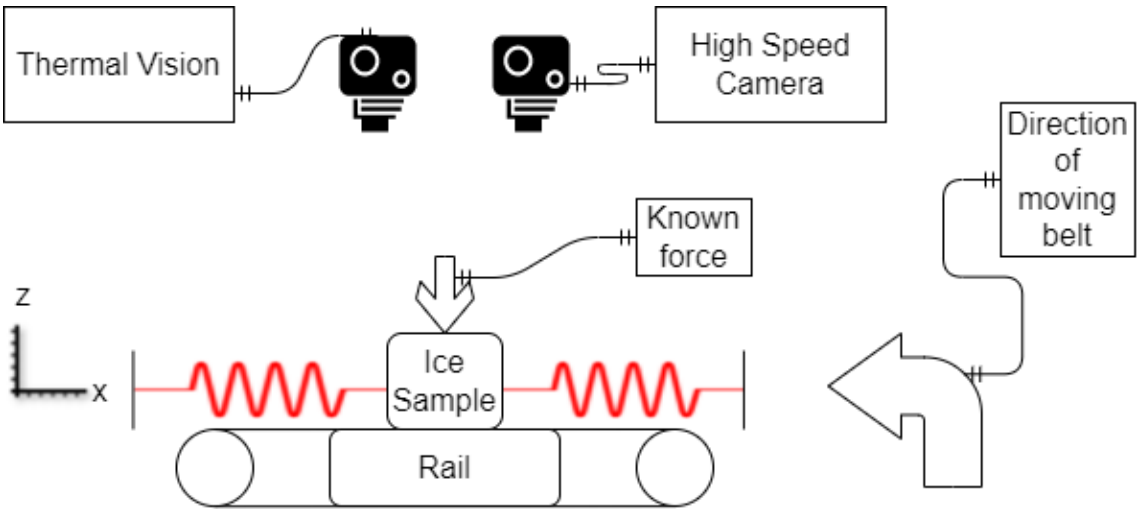

Figure 3.2: Illustration of 1D set-up with sandpaper conveyor belt sketched in *xz*-frame

Table 3.2: Advantages and disadvantages of 1D set-up with sandpaper conveyor belt

Test Set-up	Can concrete or steel be used as sliding surface?	Easy to change material/ice?	1D or 2D displacements	Dimensions of experiment
Sandpaper Conveyor Belt	No, (-)	Yes, (+)	1D (x), (+)	Compact, (+)

3.1.3. 1D Set-up With Pulling Concrete Sample Over Ice

The last possible test set-up to discuss is 1D test set-up illustrated in Figure 3.3. In this set-up a concrete sample is placed on a long ice rink with length *B*. This sample of concrete is than slid over the ice with the held of a pulley *A*. This pulley functions as such that a constant relative sliding velocity of the concrete sample is maintained. Furthermore, this pulley should measure the force needed to overcome first the static friction, when the concrete sample is stationary, and the kinetic friction when the concrete sample is sliding towards the pulley *A*. To make sure that the concrete sample moves only in x-direction, and not in y-direction, beams can be placed on either side of the sample. These beams can be made with one side covered in teflon or another material with low friction, to ensure that the interface with the mass barely has any friction. This ensures 1D behaviour, and because the sample only moves in one direction the amount of rope that is pulled on by the pulley *A* is also the displacement of the concrete sample.

The distance *B* between the sample and the pulley *A* is the limiting factor in this set-up. With a velocity of 0.5 m/s (more on the testing parameters in Subsection 3.4.1) and a desired experiment duration of 20 s, the length of the ice rink must at least be 10 m. This is too large for the space available in the Coldroom at the Faculty of Civil Engineering and Geosciences.

The concrete sample can be easily substituted for a new sample, and also other materials, such as steel, can be used in this set-up. This cannot be said for the ice rink. The needed length to get proper results makes changing of the ice hard. Also, creating such a long ice rink requires a fridge of dimensions that are not present at the faculty. A way to overcome this problem is to carry out the experiments at an ice rink nearby. An ice rink could enable to carry out experiments with a smooth ice surface (after it has been prepared with an ice machine like a Zamboni) and with a rougher ice surface (after the ice-skates have used the rink and the ice is carved into). Another way to carry out the same experiment is when pulling the mass with an ice machine over the ice, and connect the mass to the ice machine by means of a loadcell. Difference with this set-up is that in the latter set-up the ice machine moves compared to the first set-up discussed in this Section.

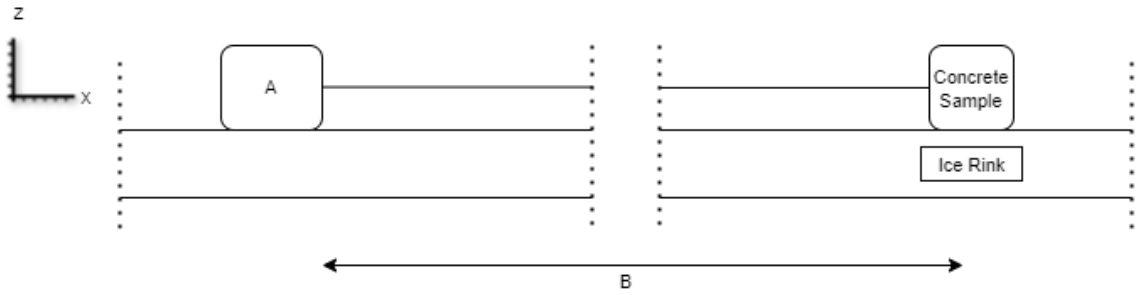

Figure 3.3: Illustration of 1D set-up with a concrete sample being pulled over ice sketched in *xz*-frame

Table 3.3: Advantages and disadvantages of 1D set-up with a concrete sample being pulled over ice

Test Set-up	Can concrete or steel be used as sliding surface?	Easy to change material/ice?	1D or 2D displacements	Dimensions of experiment
Sample pulled over ice	Yes, (+)	Yes/No, (+/-)	1D (x), (+)	Not Compact (-)

3.2 Best 1D Test Set-up

The 3 possible test set-ups considered have been discussed and their advantages and disadvantages are summarised in Table 3.4. The set-ups were analysed based on the criteria of 1D behaviour, limited floor space, accessibility and easy to change materials, and whether or not construction material could be used for the sliding interface. Furthermore, all possible test set-ups had to met the criteria of being able to withstand freezing temperatures of up to -20°C and relative sliding velocity ranges from 0.1 m/s - 0.5 m/s. When counting the positive indicators per test set-up, the test set-up with the sandpaper conveyor belt comes out on top. This is because it meets the three out of the four criteria used in the assessment. There is one criterion on which this test set-up is assessed negatively: this test set-up cannot use concrete or steel as a sliding interface. For this the substitute of sandpaper is believed to mimic the roughness of concrete or steel, though it is unclear if the mimicking of the concrete and steel works out in the experiment. For instance, the sandpaper might get wet due to occurring frictional heating during the experiment. This could affect the integrity of the sandpaper causing it to be unuseful for the experiment. Sandpaper is a kind of material that is used often in construction works. That is why it is assumed at this stage that the sandpaper is strong enough and can therefore be used to carry out this experiment.

The 1D test set-up with the sandpaper conveyor belt is worked out further, including the ideal construction layout and the actual construction layout, in Section 3.3.1.

Table 3.4: Advantages and disadvantages of all possible set-ups

Test Set-up	Can concrete or steel be used as sliding surface?	Easy to change material/ice?	1D or 2D displacements	Dimensions of experiment
Concrete Caterpillar Belt	Yes, (+)	No, (-)	2D (x and z), (-)	Compact, (+)
Sandpaper Conveyor Belt	No, (-)	Yes, (+)	1D (x), (+)	Compact, (+)
Sample pulled over ice	Yes, (+)	Yes/No, (+/-)	1D (x), (+)	Not Compact (-)

3.3 Construction Details of Chosen 1D Test Set-up

3.3.1. Ideal Construction Layout

As described in Section 1.1 in previous research a set-up was used that resulted in 2D behaviour of the sample. Therefore, a set-up is presented that will only exert forces in one direction. The ideal construction sketched in Figure 3.4 below displays a conveyor belt that is only moving in one direction; clockwise. It resembles the ideal overall layout of the set-up that can be used for the experiment. The conveyor belt should be made of a material of which the roughness is known, and multiple materials should be used to research the influence of different roughnesses on the friction coefficient. Overhanging cameras should be used to track the movements of the ice sample and to detect the temperature fluctuations along the interface between the ice sample and the conveyor belt.

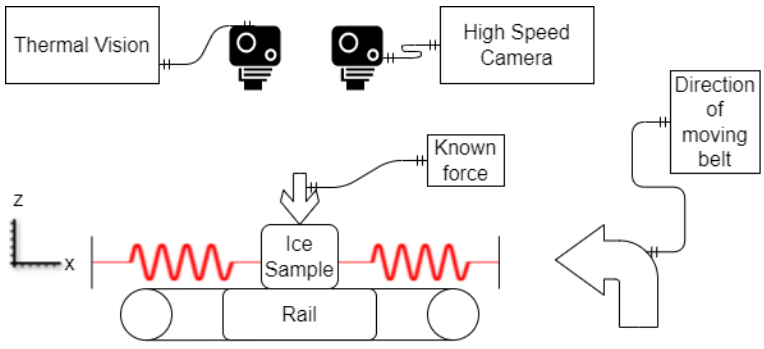

Figure 3.4: Construction Layout sketched in *xz*-frame

Conveyor Belt System

The conveyor belt will be held in place by the frame as shown in Figure 3.5. The conveyor belt should be held in place by 4 sets of 2 rolling cylinders that are squeezed together. This ensures that the belt does not slip over the cylinders. As the moving direction of the conveyor belt is clockwise the upper right set of cylinders must be driven by a motor to ensure stable tension in the upper section of the belt, which is where you would want to know the occurring friction force. Because the ice sample in the middle of the upper section of the belt will push down on the belt, a secondary railing should be used to keep the conveyor belt in the correct vertical position.This railing should also be covered in teflon to avoid wear on the back side of the conveyor belt. A schematic overview of the motor-belt connection is shown on below in Figure 3.5.

Full dimensions of all to be constructed parts are displayed in Figure C.1 in Appendix C. Next to that the full dimensions of the poles holding the cylinders can also be found in Appendix C, Figure C.2.

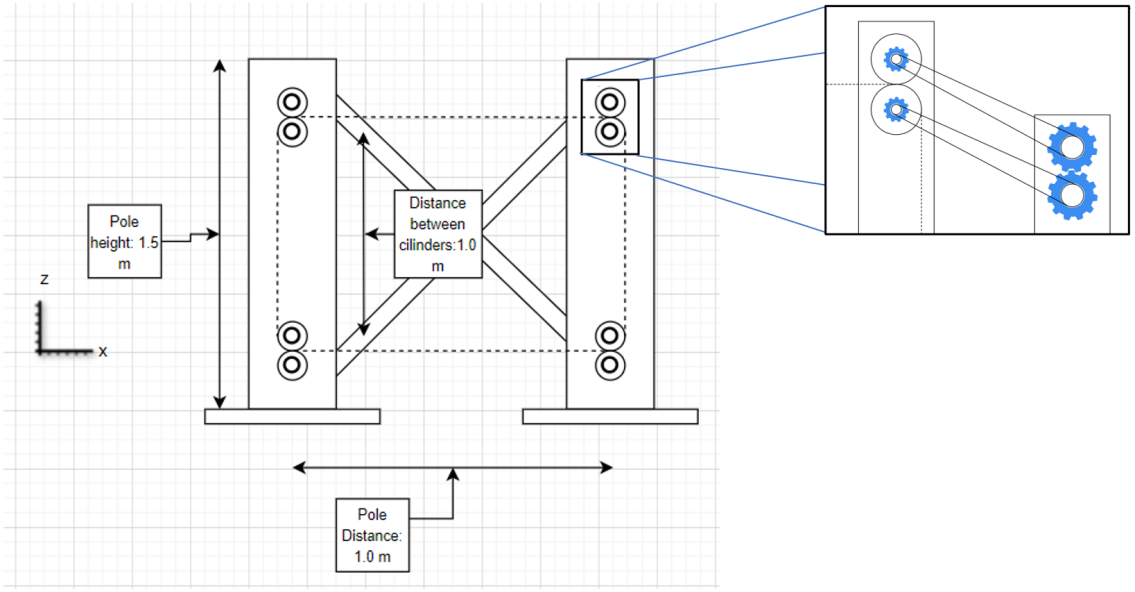

Figure 3.5: Conveyor Belt System sketched in in *xz*-frame

Ice Holding Structure (1D)

The ice sample can be a cylinder with a diameter of 8 cm, and can be held in place with the help of a square shaped frame. The height of the cylinder can initially be set at 10 cm. This height may be varied. More on that in Section 3.4.1. This frame will be able to move back and forth under the friction from the conveyor belt, as can be seen in Figure 3.6. It will be held in place with the use of the four springs attached to the top and bottom side, and the railings that are on the left and right side of the frame. The interfaces between the square shaped frame and the railings should be coated with Teflon to ensure as little friction as possible while still maintaining the upright position of the square shaped frame. This in turn assures that only 1D displacements occur. The upper and lower horizontal beam will provide the connection to the table poles, as will be further explained in Section 3.3.1. The full dimensions of all to be constructed parts displayed in Figure C.3 are shown in Appendix C.

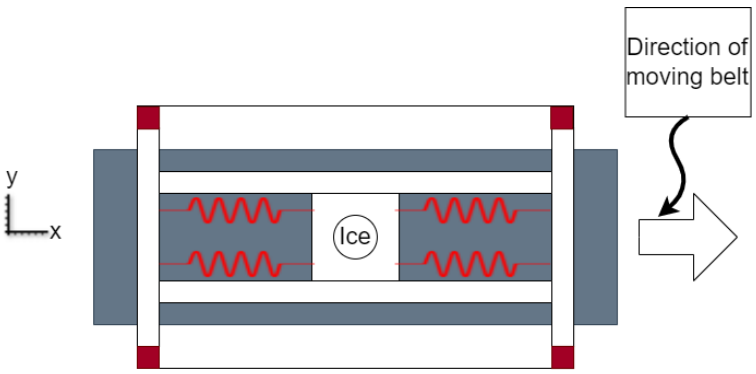

Figure 3.6: Ice Holding Structure 1D sketched in *xy*-frame

Supporting Frame
To stabilise all the equipment needed two tables can be placed over each other. At the long ends the Ice Holding Structure should be connected to the table poles of the upper table. Secondly, the two cameras can be attached to the bottom side of the upper table. These are attached at the aforementioned place because the motion camera needs to be exactly on top to detect the displacements. The two tables may not touch each other because during the experiments the lower table will vibrate due to moving belt and ice sample. If the two tables would touch each other the vibrations from the experiment could cloud the measurements from the cameras. The thermal imaging camera can be placed next to high speed camera to be able to show the temperature at the ice-belt interface. It is herein assumed that when placing the thermal imaging camera above the sample the camera can see through the ice and measure the temperature at the ice-belt interface. This assumption will have to be tested in a physical set-up to see whether this is a valid assumption or not. Lastly, the railing supporting the belt will be attached on the top side of the lower table. This is schematically shown in Figure 3.7a below, looking from the front to the back, so in x-direction. The full dimensions of all to be constructed parts displayed in Figure C.4 are shown in Appendix C.

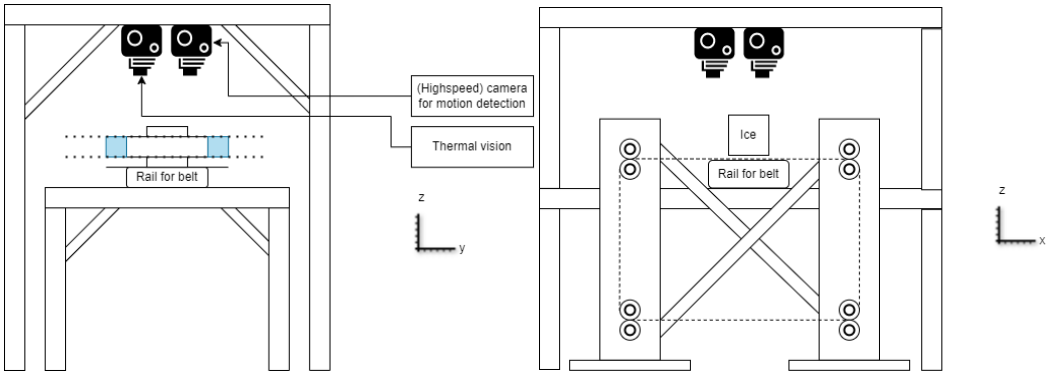

(a) Supporting Frame sketched in *yz*-frame (b) Overall sketch in *xz*-frame

Figure 3.7: (a,b): Sketches of the Supporting Frame and how that Supporting Frame is build around the conveyor belt system

Length of Belt
As a result of the ice sample making contact with the belt the temperature in the belt will drop. A prerequisite of the experiment to give stable output is that the temperature of the belt when it moves underneath the ice sample again after a full rotation should be the same. To ensure this a thermodynamic calculation has been made for the extreme values that will be used during this research. An ice sample with a mass 0f 461 g plus an added mass of 910 g will be used (see also Subsection 3.3.3 for the mass and Subsection 3.4.1 for the added mass) and The initial friction coefficient is set at 0.3 (Nakazawa, 1986). The frictional force is calculated as follows:

$$F_{friction} = \mu_k * \text{mass} * g = 0.3 * (461 + 910) * 9.81 = 4.1261N \tag{3.1}$$

This friction force acts over a distance of 0.08 m, which is the length of the ice-structure interface. This results in a amount of heat that is generated, and is calculated as follows:

$$\Delta E_t = F_{friction} * \text{distance} = 4.1261 * 0.08 = 0.3301J \tag{3.2}$$

The full belt has a given mass of 28 g and a length of 53.3 cm (Gamma NL, 2021). This sandpaper is primarily made of sand. The mass of the part of the belt underneath the ice sample is calculated as follows:

$$m_{belt} = 28\text{g} * \frac{10\text{cm}}{53.3\text{cm}} = 5.3g \tag{3.3}$$

With a specific heat capacity of sand of c_p of 0.84 $\frac{J}{g°C}$ (*World of Physics*, 2000) this results in a temperature rise of:

$$\Delta T = \frac{\Delta E_t}{c_p m_{belt}} = \frac{0.3301}{0.84 * 5.3} = 0.0748°C \tag{3.4}$$

This gives the belt a new temperature T_1 = -7.9252 °C. Ideally, the temperature at the ice-structure interface must be constant, so equal to the ambient temperature of -8 °C. Therefore, the belt must cool down. The

length of the belt is initially set at 4 m, and it will be determined whether that length is long enough for the material to cool down to the ambient temperature.
At a belt velocity of 0.82 m/s (maximum value, see Subsection 3.4.1) the amount of time it takes for the belt to travel from the end of the sample all the way round to the front of the specimen, is calculated as follows:

$$t = \frac{L_{belt} - L_{sample}}{v} = \frac{4.0 - 0.08}{0.82} = 4.78s \tag{3.5}$$

Newton's law of Cooling is given below, and calculates the temperature at a given time after it starts cooling down:

$$T_2(t) = T_{ambient} + (T_{heatedbelt} - T_{ambient})e^{-kt} \tag{3.6}$$

A thermal conductivity of k = 0.25 $\frac{W}{mK}$ (*Thermal Conductivity - selected Materials and Gases*, 2003) is chosen as the belt will become wet as a consequence of the frictional heat that will melt parts of the ice sample. The extremest value was chosen, in a range varying from 0.25 - 2, to determine the normative values. At t = 4.78 *s*, this results in a T_2 of -7.9774 °C. Given that the parameters used are the extreme values (as proposed later on in this thesis in Section 3.4.1) it is concluded that the difference between the ambient temperature and the temperature rise of the belt material is within acceptable limits to be able to say that the temperature rise has no significant influence on the data that will be obtained during the experiment. Hence, the belt is long enough. Also, to measure this small temperature difference it would require extremely precise and expensive thermal measuring equipment, which we cannot afford. Doing the same calculations for a shorter belt length gives higher temperatures, as presented in Table 3.5 below. Even for the shortest belt length considered the temperature increase is minor. Hence, a belt of 1 metre length can be used during this experiment.

Length belt [m]	T_2
1	-7.9435 °C
2	-7.9583 °C
3	-7.9693 °C
4	-7.9774 °C

Table 3.5: Belt temperature after one rotation before it slides again under the ice sample

Ice Holding Structure (2D, optional)
To determine 2D displacements and the effect of uneven friction forces along the sliding plane therein the railings to each side (as can be seen in Figure 3.8, Section 3.3.1) can be removed. This releases the square shaped frame of its boundaries and creates the possibility of being able to move laterally. The research of the 2D behaviour is optional, and of 2nd priority. Again, the upper and lower horizontal beam should be attached to the table poles, as explained in Section 3.3.1. The full dimensions of all to be constructed parts displayed in Figure C.5 are shown in Appendix C.

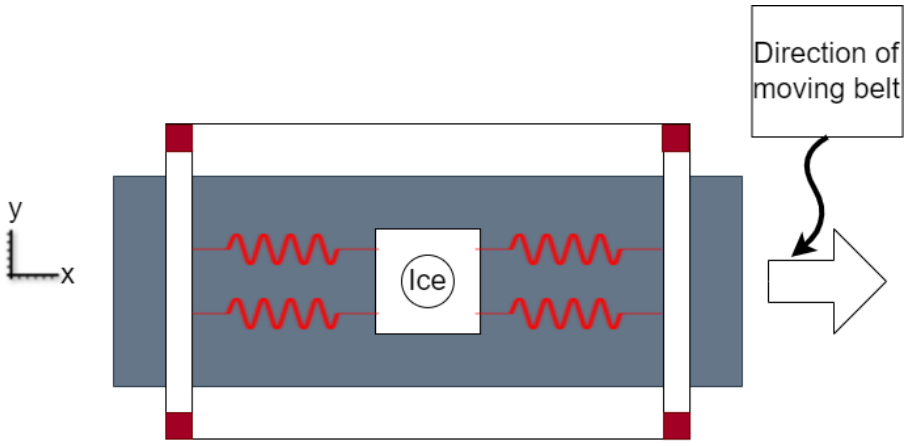

Figure 3.8: Ice Holding Structure 2D, sketched in in *xy*-frame

3.3.2. Actual Construction Layout

After consultation with the graduation committee it was decided to make some adjustments to the layout and a construction company was searched for and called in for help. Again, due to construction delays it was decided to not further pursue a physical experiment and put the emphasis of this thesis on the realisation of a numerical model.

Belt Sanding Machine

After a thorough search a belt sanding machine was selected that best resembled the ideal construction as proposed in Section 3.3.1. This machine comprises of a horizontal belt over two rolling cylinders, and has a total length of 2 metres. The complete structure is presented below in Figure 3.9. The belt is free of any attachments on the side so it is convenient for the use of the Ice Holding Structures as described in Subsections 3.3.1 and 3.3.1. Furthermore, the construction is compact so it will easily fit in a laboratory. The latter was especially convenient because the laboratory in which the experiment would have been conducted is small, and more experiments beside the one proposed have to be carried out simultaneously.

Figure 3.9: Actual Belt Sanding Machine (Heejan, 2021). Actual machine to be used in the test set-up. The sandpaper conveyor belt is the brawn element that can be seen in the top of the figure, the motor of the conveyor belt consists of the black objects on the left, and the grey surrounding table can be used to place equipment on

In addition, this set-up enables to quickly change the belt if the conditions need to be altered. In Subsection 3.3.1 it was proposed to install cylinders in pairs to ensure the belt would not slip. After consultation with the construction company it was decided that this was not necessary and that slip would not occur during the experiment as long as the tension in the belt would be high enough. How high this tension should be, is still unknown and must be looked into when performing the physical experiment. Also, the motor-belt connection is built within the cylinder on the left in Figure 3.9, so no external connection needs to be realised as was proposed in Subsection 3.3.1.

Because the realisation process of the full set-up was stopped no further efforts were done to realise the Ice Holding Structures (Subsections 3.3.1 and 3.3.1) nor the Supporting Frame for the overhanging cameras (Subsection 3.3.1).

3.3.3. Equipment Needed

Conveyor Belt Material

The conveyor belt materials that can be used should differ per experiment. These form the basis for this research. The belts can be purchased in the desired length (Gamma NL, 2021), so there is no need to create the belts and have them stitched together. These stitches would impose more wear and tear on the ice sample, which would be inconvenient for the purpose of the experiment. It is advised to use sanding paper as a substitute for concrete and steel as the roughness of sanding paper is known, and can be easily changed by using other kinds of sanding paper. Furthermore, the roughness of the sanding paper can be related to the roughness of concrete, which enables to compare them (Feng, xue Shen, dong Peng, & kai Meng, 2017). The idea of comparing the sandpaper with concrete could also have been applied when using other materials, such as a type of cloth. These are not further discussed here, but it is up to new researchers to find similar approaches to be able investigate one-dimensional friction behaviour. More information regarding the different roughnesses advised in this thesis in Subsection 3.4.1.

Ice Sample

The ice sample advised here can have a diameter of 8 cm and an initial height of 10 cm. The dimensions were chosen as such because of the presence of a drill that has the capacity to drill a round ice sample with a diameter of 8 cm. With an estimated density of 0.92 g/cm^3 (Hayes, 2017) this leads to an initial weight of:

$$\text{mass} = \pi r^2 h\rho = \pi * 4^2 * 10 * 0.92\text{g/cm}^3 = 461g \tag{3.7}$$

The height of the ice sample can be varied to perform experiments with different weights. An additional reason to use a drill is to ensure that the samples will be as identical as possible.

Thermal Imaging Camera

To detect the temperature changes along the sliding plane the “Seek Thermal ShotPRO” can be used (Electronic, 2021). This thermal imaging camera has a bolometer matrix of 320 x 240 pixels. This resembles the resolution with which the camera can sense the temperature. Furthermore, it has a temperature range of -40 °C up to 330 °C, which is suitable for the cold rooms in which the experiments will be conducted. The temperature in the cold rooms are of around -8 °C and -16 °C. The sensitivity of the camera is 70 mK. All these factors enable for high quality output.

High Speed Camera

To detect the displacements of the sample during either 1D or 2D behaviour the “Photron SA3” can be used. This high speed camera has a resolution of 1024 x 1024 pixels at a frame-rate of 1,000 frames per second. This ensures that the minor displacements can be measured accurately. This same camera will also be used to determine the instantaneous velocity of the conveyor belt. More on the latter in Section 3.4.1.

3.4 Test Plan for Identification 1D Ice-Structure Friction Coefficient

In this Section the test plan will be introduced. In Subsection 3.4.1 all the testing parameters will be explained and a selection will be made which to include in the experiment, and which not. Furthermore, a differentiation is made prioritising which materials/settings/etc. are regarded to be more important than others. This is done to make sure the experiment remains work-able in view of time. In Subsection 3.4.3 the overall testing procedure is described including a total amount of experiment runs that will have to be conducted.

3.4.1. Testing Parameters

The experiment should be conducted for several testing parameters that can be adjusted. In the Subsubsections 3.4.1 – 3.4.2 the to be used parameters will be specified along with which parameters are of 1st, 2nd or 3rd priority. The parameters marked with the highest priority should be used 1st. If time permits the 2nd priority parameters can be used, and after that the 3rd priority parameters will be used.

Temperatures of Ice & Surroundings

The experiment should be conducted in the cold room at a temperature of -8°C. As the ice samples should be made in the same cold room, and the set-up will be in the cold room at all times, the temperature of the used materials will be the same. Only during the experiment run will the temperature of the ice sample and the conveyor belt material rise due to the heat that is generated due to friction at the interface. Insubsection 3.3.1 the temperature rise per rotation is determined. If time permits the temperature of the surroundings can be set at -16°C. This would mean that the 2nd priority experiments will be conducted in the other cold room at TU Delft's faculty of Civil Engineering and Geosciences. Again, all the materials and samples should have this temperature to create a temperature as consistent as possible.

Table 3.6: Experiment Temperatures

1st Priority	2nd Priority
-8°C	-16°C

Roughness

Different kind of sandpapers can be used differentiating the roughness. The lower the grid number, as specified in Table 3.7 below the coarser the grit of the sandpaper. In the 1st priority sandpapers will be used with a friction coefficient that resemble the coefficient of ice-concrete interaction (Feng et al., 2017).

The sandpapers of 2nd priority are coarser compared to the 1st priority. These should be used to create a better picture of the total influence of roughness of the material on the friction coefficient. The last priority materials will consist of metals as it may be interesting to see what happens with such materials.

Table 3.7: Conveyor Belt Material

1st Priority	2nd Priority	3rd Priority
Sandpaper:	Sandpaper:	Metals:
- K100	- K40	- Aluminium
- K120	- K60	- Steel
- K150	- K80	- Stainless Steel

Normal Force/Weight

As the friction force depends linearly on the applied normal force this experiment can only have meaningful conclusions if multiple values for the normal force are used (Marghitu, 2001). The initial case will have only the self-weight of the ice sample of 461 g, as shown in Equation 3.7. With the use of known masses the applied normal force will be increased. These known masses can be placed on the square shaped frame, the frame can be seen in Figure 3.6. To avoid an imbalance on the frame the weight will be equally distributed. In Table 3.8 the added masses are shown. To be able to check this data against the data previously found by (Nuus, 2018), the masses of the aforementioned research and this experiment should be the same. The 2nd priority masses can be used to create an even more comprehensive overview of the influence of speed on the coefficient of friction.

It is very likely that the samples will not be exactly the same in weight as the samples do not come in perfect cylinders. Hence, each sample should be weight before the test is being run. After a sample is used once it will be flipped upside down to use the unscathed side. Again, the sample will 1st be weighed to account for the loss of mass due to the wearing and frictional heating in the 1st run.

1st Priority	2nd Priority
- 0.00 kg	- 0.45 kg
- 0.20 kg	- 0.65 kg
- 0.40 kg	- 0.91 kg

Table 3.8: Normal Force/Weight

Relative Sliding Velocity

As can be seen in Figure 3.10 the coefficient of friction of ice-concrete interaction reduces when velocity of the sliding plane increases. Hence, it is important to look into the effect of the speed of the conveyor belt on the friction that the ice sample in the proposed set-up experiences. It is because of this influence, that has already been established, that this influence must be closely examined in this experiment. In Figure 3.10 it can be seen that the friction coefficient reduces with different paces along the velocity spectrum. That is why in this research different ranges of velocities will be used. The velocities labelled as 1st priority in Table 3.9 represent very low velocities that correspond to the extreme values in Figure 3.10. However, it may be impossible for the set-up to have a stable velocity that is as low as mentioned.

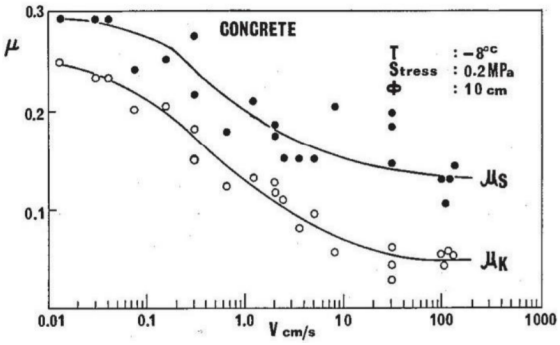

Figure 3.10: Effects of relative velocity on concrete (Nakazawa, 1986)

The motor-belt connection will experience friction when transferring the motion from the rollers to the conveyor belt. It is likely that this friction will not be completely stable and hence, the velocity of the belt will not be stable as well. To account for the instantaneous velocity of the conveyor belt and the impact this will have on the friction in the ice-belt interface the instantaneous velocity should be measured with the High Speed Camera as described insubsection 3.3.3.

If the aforementioned velocities are not feasible a switch should be made to the 2nd priority velocities which can been found in Table 3.9. Also, if the 1st set of velocities is feasible and time permits the 2nd set of velocities can be used. Both sets of velocities is chosen as they are the same as the velocities used by Nuus (2018). This gives the possibility to compare the data to be find in this research to the data found by the aforementioned research.

In the sets of velocities a high, medium and low value has been chosen to create a set of extreme values while still being relatively in the same range to be able to make proper conclusions. These ranges resemble linear as can be seen in the log graph in Figure 3.10. Because velocity is a parameter of high significance and the aim is to have a motor that is easily adjustable more velocities can be used in this experiment if time permits.

1st Priority	2nd Priority
- 0.15 m/s	- 0.50 m/s
- 0.25 m/s	- 0.63 m/s
- 0.37 m/s	- 0.82 m/s

Table 3.9: Velocities used

1D or 2D
Only if time permits can the 2D behaviour be researched. This is represented in Table 3.10. This data can be added to the data found by Nuus (2018) to create an improved comparison.

1st Priority	2nd Priority
- 1DOF	- 2DOF

Table 3.10: Degrees of freedom of set-up

3.4.2. Statistical Analysis
For one certain set of parameters a statistical analysis should be carried out to see how much the displacements and friction differ under the same circumstances. This set of parameters will be determined later on. 10 runs should be carried out with this set of parameters.

3.4.3. Overall Test Procedure
All in all, using the testing parameters as labelled as 1st priority combined the overall test procedure will include a total of 27 combinations of parameters, plus an additional 5 runs for the statistical analysis. It is estimated that one experiment run takes 30 seconds; 10 seconds to start moving the conveyor belt, and 20 seconds of constant conditions during which the sample can move freely and data is generated. It is estimated that it takes a 8-10 minutes to adjust the set-up to the new parameters (switch springs, new ice sample or switch the sandpaper belt). The time to carry out one run is around 15 minutes, taking into account some extra time to allow for time lost in case something goes wrong. Because of the temperature in the coldroom, someone cannot stay longer than 40 minutes in the coldroom at once, and it is advised to make no more than 3 visits to coldroom per day. This means that 2 experiments per visit can be carried out, and so per day a maximum of 6. So to carry out all experiments 6 days are required for the full experiment. This is provided that enough ice samples are created in advance. and so it should be able to carry out all experiments in a week. Taking all preparations and testing the set-up into account, the whole test procedure can be completed in three weeks.

If all testing parameters labelled as 2nd and 3rd priority will be used this will amount to a total of 1306 combinations. This vast amount of combinations is time consuming and it is unlikely to be able to be completed. Therefor, if time permits, a selection of the 2nd and/or 3rd parameters should be made to execute additional runs. Those are chosen at a later stage when, with the benefit of hindsight based on the runs already executed, it is known which parameter proves to be more interesting to execute additional runs with.

3.5 Discussion Regarding Realisation 1D Test Set-up & Switching Focus of Thesis to 2D Modelling

After selecting the best test set-up for the identification of 1D friction coefficients, a company was contacted that could realise the test set-up. This company was very eager at first to build the set-up and they believed it would be feasible to create the set-up within a reasonable amount of time, say two months. During those two months the numerical model could be made that could be used to analyse the experimental data with. Unfortunately, the realisation of the test set-up took too long. After four months there was still no test set-up. With the advice of the supervising committee it was decided to switch the focus of this thesis towards modelling a 3 degree of freedom system based on the experiment that Nuus (2018) already carried out. In hindsight it would have been better to focus on the manufacturability of the test set-up, which was not taken into account during the selection of a test set-up. Another good idea would have been to build a test set-up independently without a company.

The experiment that Nuus (2018) conducted had a test set-up as shown in Figures 3.11a & 3.11b. It consisted of an ice sample which was placed on the outer edge of a rotating concrete slab. It was assumed that by placing it on the outer edge the ice sample would only move in x-direction, and not in y-direction nor show rotations. However, she did find y-displacements and rotations. For the analysis of the data Nuus (2018) developed a 1 degree of freedom model. With this 1DOF model she fitted the experimental data of her experiment and identified the corresponding friction coefficients. But because of the two-dimensional (2D) behaviour she found the results that she obtained are not completely reliable. That is why she recommended to carry out experiments with a test set-up that would only show 1D behaviour to try and identify the friction coefficients using a 1DOF model (like Nuus (2018) developed). That was the first intention of this study.

Now that the realisation of the 1D test set-up took too long the switch was made to model the experiment Nuus (2018) with a 3DOF model. This model would be able to describe the 2D behaviour that Nuus (2018) found. With a model that is able to describe the 2D behaviour it is assumed that that would lead to a better identification of the friction coefficients. That way the 3DOF model would be an improvement in relation to the already developed 1DOF model by Nuus (2018). This 3DOF model is developed and elaborated in Chapter 4.

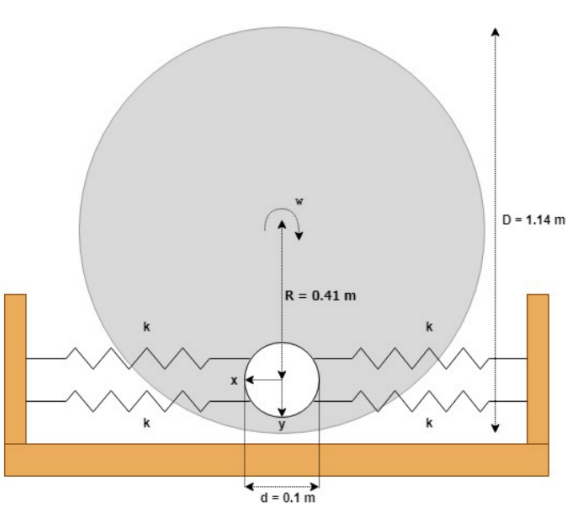

(a)

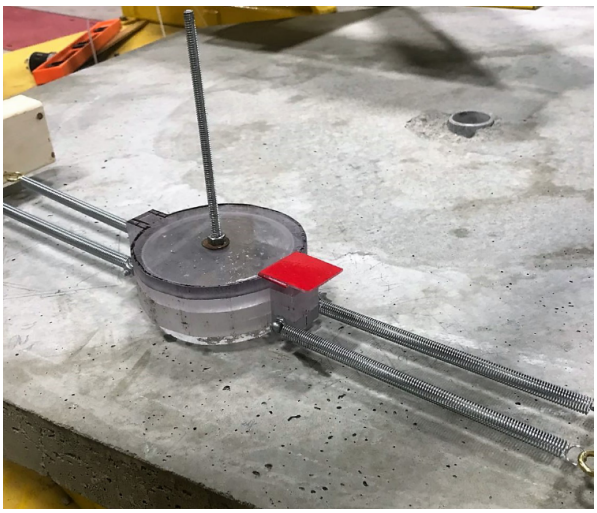

(b)

Figure 3.11: (a): illustration top view of 2D test set-up used by (Nuus, 2018) sketched in *xy*-frame, (b): ice holder structure with springs (Nuus, 2018)

Chapter 4

3DOF Numerical Model Of 2D Ice-Structure Friction

In this chapter the three degree of freedom (3DOF) numerical model is developed. Section 4.1 gives a brief overview of the stick-slip phenomenon, which has already been elaborated on in Section 2.5, including a way to model this phenomenon. In Section 4.2 the Equations of Motion are derived based on the Lagrangian approach. The angle α between the spring's current and instantaneous position during the dynamic behaviour has impact on the forces exerted by the springs on the mass. That is why four different approaches will be carried out. Each time the angle α is used differently, and a comparison is made to determine which approach best represents the actual behaviour. Section 4.3 then gives the State Equations which will be used in the model, and describes how the model is built. Furthermore, it presents a comparison between the four approaches established in Section 4.2. Section 4.4 shows two approaches on how to derive the friction forces and moments that will be provided to the numerical model as input. 4.5 presents verification checks to show that the output of the numerical model corresponds with simplified models such as a 1DOF mass-spring system. In Section 4.6 the validation of the model is done.

4.1 Modelling The Stick-Slip Phenomenon

The numerical model that was set up in this thesis is based on the 1DOF and 2DOF models used by Leine et al. (1998). The model used in this research will be a 3DOF model, and thus an extension of the models used by Leine et al. (1998). Figures 4.1a and 4.1b present a side and top view that illustrates on which the numerical model is based. It is an extension of the representations shown in Section 2.5.

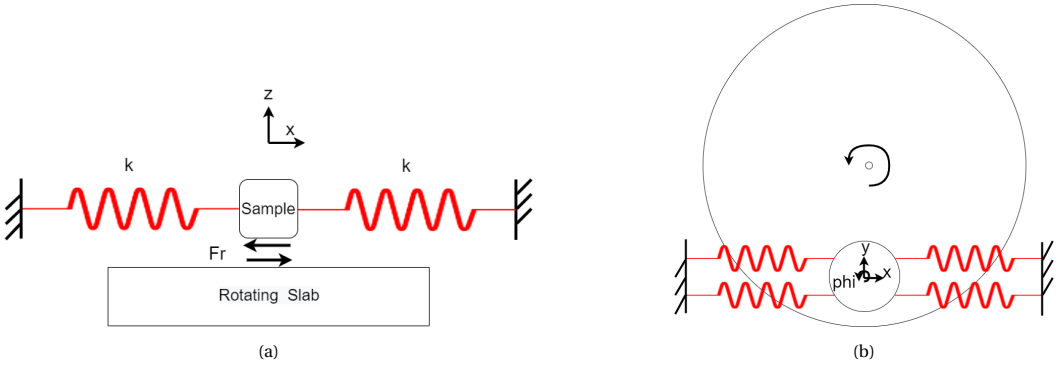

Figure 4.1: (a): Side view of Model, (b): Top view of Model. Both figures show the model in *xy*-frame

As can be seen in Figures 4.1a and 4.1b a block of mass is placed on a rotating slab. The mass is held in place with 4 springs, and is positioned as such that the mass is in equilibrium. Meaning that the springs are neither extended nor compressed. Once the table starts to rotate the slab will exert friction on the mass and the mass will start moving along the angular movement of the slab. When the velocities of the mass and

of the slab are equal in both size and direction the mass is considered to be in stick mode. This movement causes two springs to extend and two springs to compress leading to a build-up of forces in the springs. As long as the static friction force (based on Coulomb Law of Friction (Marghitu, 2001)) between the mass and slab is larger than the forces in the springs combined, the mass remains in stick mode and moves along with the slab. At a certain moment the forces in the springs become larger than the static friction force causing the mass to start sliding over the slab. This phase is called slip mode. During slip mode the mass is pushed backwards by the springs, moves through the equilibrium position, after which it slows down and is pulled again in positive x-direction, and the mass keeps moving back and forth. Somewhere during this alternating phase of forwards and backwards motion the relative sliding velocity of the mass and the rotating slab will be 0 and the mass switches to stick mode. A more thorough explanation of stick-slip can be found in Section 2.5.

4.2 Derivation of Equations of Motion

For the derivation of the Equations of Motion the Lagrangian approach is used, as presented in Equations 4.1 and 4.2 (Morin, 2007). Here K represents the kinetic energy of the system, and P represents the potential energy, and is written out in Equation 4.3. Here, the term ϵ_i refers to the four individual elongations of the springs, which is elaborated on in Equation 4.4. The full derivation of the spring elongation and the Equations of Motion concerning x, y and ϕ can be found in Appendix A.

$$\frac{d}{dt}\left(\frac{\delta L}{\delta \dot{q}_j}\right) - \frac{\delta L}{\delta q_j} = 0 \tag{4.1}$$

Where: $\dot{q}_j = \dot{x}, \dot{y}, \dot{\phi}$ and $q_j = x, y, \phi$.

$$L = K - P \tag{4.2}$$

$$L = \frac{1}{2}(m\dot{x}^2 + m\dot{y}^2 + J\dot{\phi}^2) - \frac{1}{2}k_i\epsilon_i^2 \tag{4.3}$$

$$\epsilon_i = \Delta x_i sin(\alpha_i) + \Delta y_i cos(\alpha_i) \tag{4.4}$$

$$\Delta x_i = x + rcos(\beta_i + \phi) - rcos(\beta_i) = x + r\left(cos(\beta_i)cos(\phi) - sin(\beta_i)sin(\phi)\right) - rcos(\beta_i) \tag{4.5}$$

$$\Delta y_i = y + rsin(\beta_i + \phi) - rsin(\beta_i) = y + r\left(sin(\beta_i)cos(\phi) + cos(\beta_i)sin(\phi)\right) - rsin(\beta_i) \tag{4.6}$$

Where i = 1,2,3,4 and it indicates the respective spring as shown in Figure 4.2a. Equations 4.3-4.6 mention the degrees of freedom x, y, ϕ. These are illustrated in Figures 4.2a and 4.2b (to clarify, α_i and ϕ are not necessarily the same as might be concluded from looking at Figure 4.2b):

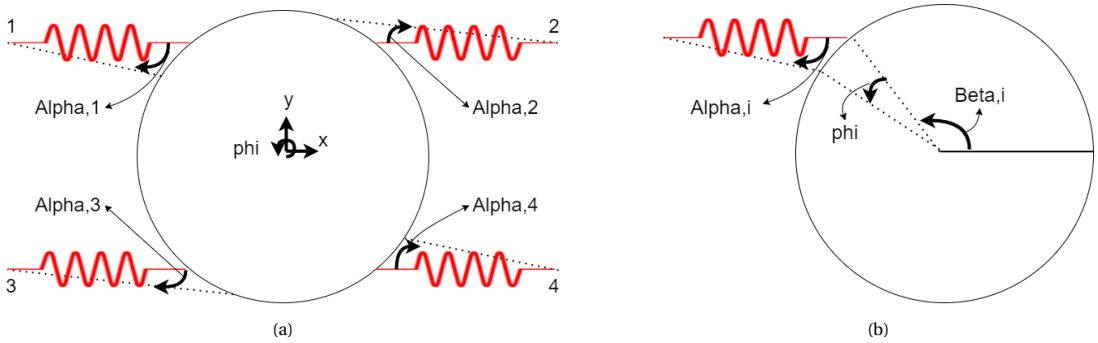

Figure 4.2: (a): Orientation of Axes and degrees of freedom. Full stripes indicate the springs in original position, and the dashed lines indicate the springs after rotation of the ice mass, (b): Orientation of α, β and ϕ. Both figures show the model in xy-frame

4.2.1. Kinetic Energy

For the derivation of the kinetic energy Equations 4.7 - 4.10 follow from Equations 4.1 - 4.3:

$$\frac{d}{dt}\left(\frac{\delta L}{\delta \dot{q}_j}\right) = \frac{d}{dt}\left(\frac{\delta K}{\delta \dot{q}_j}\right) \quad , \quad \dot{q}_j = \dot{x}, \dot{y}, \dot{\phi} \tag{4.7}$$

$$\frac{d}{dt}\left(\frac{\delta K}{\delta \dot{x}}\right) = m\ddot{x} \tag{4.8}$$

$$\frac{d}{dt}\left(\frac{\delta K}{\delta \dot{y}}\right) = m\ddot{y} \tag{4.9}$$

$$\frac{d}{dt}\left(\frac{\delta K}{\delta \dot{\phi}}\right) = J\ddot{\phi} \tag{4.10}$$

4.2.2. Potential Energy

For the derivation of the potential energy Equations 4.11 and 4.12 follow from Equations 4.1 - 4.3:

$$-\frac{\delta L}{\delta q_j} = \frac{\delta P}{\delta q_j} = \frac{\delta}{\delta q_j}\left(\frac{1}{2}k_i\epsilon_i^2\right) \qquad , \qquad q_j = x, y, \phi \tag{4.11}$$

Where:

$$\frac{1}{2}k_i\epsilon_i^2 = \frac{1}{2}k_i\left(\Delta x_i sin(\alpha_i) + \Delta y_i cos(\alpha_i)\right)^2 \qquad , \qquad i = 1,2,3,4 \tag{4.12}$$

The full derivation of the potential energy to retrieve the stiffness components of this system can be found in Appendix A. The general result for spring 1 is given below in Equations 4.13 - 4.15:

$$\frac{\delta P_1}{\delta x} = \frac{1}{2}k_1\left[2C^2x + 2CDy + \left(2ACD - 2BC^2\right)\phi\right] \tag{4.13}$$

$$\frac{\delta P_1}{\delta y} = \frac{1}{2}k_1\left[2CDx + 2D^2y + \left(2AD^2 - 2BCD\right)\phi\right] \tag{4.14}$$

$$\frac{\delta P_1}{\delta \phi} = \frac{1}{2}k_1\left[\left(2ACD - 2BC^2\right)x + \left(2AD^2 - 2BCD\right)y + \left(2A^2D^2 - 4ABCD + 2B^2C^2\right)\phi\right] \tag{4.15}$$

Where:

- A = $rcos(\beta_1)$
- B = $rsin(\beta_1)$
- C = $rcos(\alpha_1)$
- D = $rsin(\alpha_1)$

To get the expressions as presented in Equations 4.13 - 4.15 for the other springs the β can simply be changed to the β corresponding to the coordinates of the other points where the other springs are attached to the mass. The indices 1-4 correspond to the numbers as presented in Figure 4.2a. These βs are derived from pictures presented by Nuus (2018):

- β_1 = 160°
- β_2 = 20°
- β_3 = 200°
- β_4 = 340°

The incorporation of the βs is straightforward. However, this is not the case for the four different αs, because they change as the ice mass moves. This means another varying parameter is present in the model. To deal with this four different approaches have been carried out to see how to incorporate this change in α. In Subsubsections 5.2.2.1. - 5.2.2.4. this has been done, each time incorporating α differently. The modelling of the four different models is presented in Section 4.3, and a choice will be made which model best describes the 3DOF behaviour of the mass. Furthermore, it was previously stated that the spring stiffness differs between all springs. During the experiment carried out by Nuus (2018) all springs were the same. Therefor, the springs modelled herein are considered the same, and therefor have equal stiffness.

5.2.2.1. $\alpha_1 = \alpha_2 = \alpha_3 = \alpha_4$ = constant = 0

From Nuus (2018) it was derived that the displacement in x-direction was of a magnitude higher than the displacement in y-direction and the angular displacement. Therefor, it was assumed that for a numerical simulation the springs would not move in y-direction nor rotate, but only in x-direction. In this first approach α was set at 0 at t = 0. The resulting equations of motion can be found below in Equation 4.16: (the full derivation can be found in Appendix A)

$$\begin{bmatrix} m & 0 & 0 \\ 0 & m & 0 \\ 0 & 0 & J \end{bmatrix}\begin{bmatrix} \ddot{x} \\ \ddot{y} \\ \ddot{\phi} \end{bmatrix} + k * \begin{bmatrix} 4 & 0 & 0 \\ 0 & 0 & 0 \\ 0 & 0 & 0.00117 \end{bmatrix}\begin{bmatrix} x \\ y \\ \phi \end{bmatrix} = \begin{bmatrix} \sum F_r \\ 0 \\ \sum M_r \end{bmatrix} \tag{4.16}$$

On the right-hand side of Equation 4.16 the sum of forces in x-direction and the sum of moments about the z-axis can be found. It is assumed that because of the difference in relative sliding velocity or the difference in roughness of the sliding interface the friction differs along the interface. This leads to an uneven distributed friction force along the y-axis, hence the summation, and this unevenness causes a moment about the z-axis. The sum of forces in y-direction is assumed to have negligible impact because the relative sliding velocity is predominantly in x-direction, and therefor the y-component on the friction force is outside the scope of this numerical model. As a result of α = 0 at all times, no stiffness contribution to the motion in y-direction follows from this set of equations.

5.2.2.2. $\alpha_1 = \alpha_2 = \alpha_3 = \alpha_4 = \text{constant} \neq 0$

In the second approach the same assumptions as mentioned in Subsection 5.2.2.1. hold, with one adjustment. The springs were still assumed only to move in x-direction, but now under a slight angle. All αs are considered the same. This would effectively imply that the ice mass was given an initial displacement. as is illustrated on the right in Figure 4.3. This displacement in y-direction will result in y-direction displacements as the springs will intend to move back to their initial position. The resulting equations of motion can be found below in Equation 4.17: (the full derivation can be found in Appendix A)

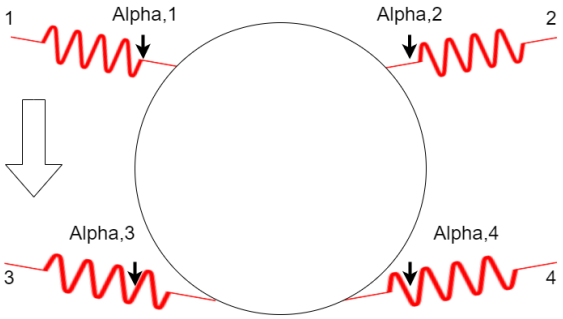

Figure 4.3: Initial Displacement in *xy*-frame

$$\begin{bmatrix} m & 0 & 0 \\ 0 & m & 0 \\ 0 & 0 & J \end{bmatrix} \begin{bmatrix} \ddot{x} \\ \ddot{y} \\ \ddot{\phi} \end{bmatrix} + k * \begin{bmatrix} 3.99878 & 0.06980 & 0 \\ 0.06980 & 0.00122 & 0 \\ 0 & 0 & 0.00117 \end{bmatrix} \begin{bmatrix} x \\ y \\ \phi \end{bmatrix} = \begin{bmatrix} \sum F_r \\ 0 \\ \sum M_r \end{bmatrix} \tag{4.17}$$

5.2.2.3. $\alpha_1 = \alpha_2 = \text{-}\alpha_3 = \text{-}\alpha_4 \neq 0$

In the third approach the same assumptions as mention in Subsection 5.2.2.1. hold, with again one adjustment. This time the distance a where the springs are attached to the mass, and the distance b between where the springs are attached to the *outside world* are not the same. This is illustrated in Figure 4.4 where $a \neq b$. The resulting equations of motion can be found below in Equation 4.18: (the full derivation can be found in Appendix A)

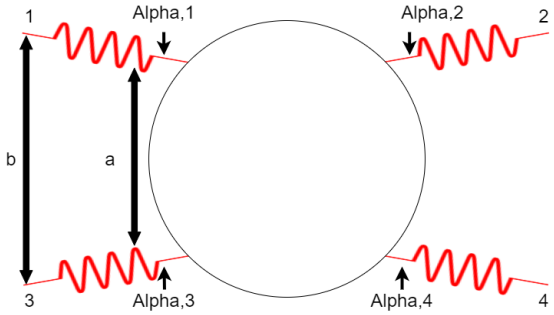

Figure 4.4: Springs attached to ice mass under opposing angles in *xy*-frame

$$\begin{bmatrix} m & 0 & 0 \\ 0 & m & 0 \\ 0 & 0 & J \end{bmatrix} \begin{bmatrix} \ddot{x} \\ \ddot{y} \\ \ddot{\phi} \end{bmatrix} + k * \begin{bmatrix} 3.99878 & 0 & 0 \\ 0 & 0.00122 & -0.00119 \\ 0 & -0.00119 & 0.00117 \end{bmatrix} \begin{bmatrix} x \\ y \\ \phi \end{bmatrix} = \begin{bmatrix} \sum F_r \\ 0 \\ \sum M_r \end{bmatrix} \tag{4.18}$$

The difference between the Equations of Motion in Subsections 5.2.2.2. and 5.2.2.3. is that in the former the motions in x-direction contribute to motions in the y-direction, whereas in the latter the rotations about the z-axis contribute to motions in the y-direction. This is due to the different sign in α_3 and α_4 between the two cases. In both cases α was considered to be ±1° to remain as close to reality as possible, because in reality the springs cannot have been placed perfectly horizontal.

5.2.2.4. Update α every iteration

In the fourth and last approach the αs are set at 0 at t = 0. In contrast to the three preceding approaches, where the αs were kept constant, the αs in this approach are updated every iteration. That means that the stiffness matrix in the Equations of Motion is not constant throughout the simulation. This results in high computation times. The resulting equations of motion can be found below in Equation 4.19: (the full derivation can be found in Appendix A)

$$\begin{bmatrix} m & 0 & 0 \\ 0 & m & 0 \\ 0 & 0 & J \end{bmatrix} \begin{bmatrix} \ddot{x} \\ \ddot{y} \\ \ddot{\phi} \end{bmatrix} + k * \begin{bmatrix} C_{xx} & C_{xy} & C_{x\phi} \\ C_{yx} & C_{yy} & C_{y\phi} \\ C_{\phi x} & C_{\phi y} & C_{\phi\phi} \end{bmatrix} \begin{bmatrix} x \\ y \\ \phi \end{bmatrix} = \begin{bmatrix} \sum F_r \\ 0 \\ \sum M_r \end{bmatrix} \tag{4.19}$$

As can be seen in Equation 4.19 the coefficients in the stiffness matrix are not predetermined. The full expressions for these coefficients can be found in Appendix A.

4.3 Modelling Equations Of Motions In State Space Form

The numerical model is set up using state-space modelling (*Dynamics and Control*, n.d.), as was also described in Section 2.5. Based on the general Equations of Motions presented in Subsection 5.2.2.4. this leads to the State Equations 4.20 and 4.22 written down below, as well as the respective friction forces as described by Equations 4.21 and 4.23:

Stick:

$$\begin{bmatrix} \dot{x}_1 \\ \dot{x}_2 \\ \dot{y}_1 \\ \dot{y}_2 \\ \dot{\phi}_1 \\ \dot{\phi}_2 \end{bmatrix} = \begin{bmatrix} v_b \\ 0 \\ 0 \\ 0 \\ 0 \\ 0 \end{bmatrix} \tag{4.20}$$

$$F_r = 4kx_1 \tag{4.21}$$

Slip:

$$\begin{bmatrix} \dot{x}_1 \\ \dot{x}_2 \\ \dot{y}_1 \\ \dot{y}_2 \\ \dot{\phi}_1 \\ \dot{\phi}_2 \end{bmatrix} = \begin{bmatrix} x_2 \\ -C_{xx}\frac{k}{m}x_1 - C_{xy}\frac{k}{m}y_1 - C_{x\phi}\frac{k}{m}\phi_1 + \frac{\sum F_r}{m} \\ y_2 \\ -C_{yx}\frac{k}{m}x_1 - C_{yy}\frac{k}{m}y_1 - C_{y\phi}\frac{k}{m}\phi_1 \\ \phi_2 \\ -C_{\phi x}\frac{k}{J}x_1 - C_{\phi y}\frac{k}{J}y_1 - C_{\phi\phi}\frac{k}{J}\phi_1 + \frac{\sum M_r}{J} \end{bmatrix} \tag{4.22}$$

$$F_r = F_{dyn} = \mu_{kin} mg \tag{4.23}$$

Where:

- k: individual spring stiffness of the four springs
- v_b: velocity of a point on the slab, in x-direction
- μ_{kin}: the kinetic friction coefficient
- C_{xx} - $C_{\phi\phi}$: can be found in Appendix A

Equations 4.20 and 4.22 were modelled in python, of which the full code can be found in Appendix B. During the slip mode a simulation tool that works as a Linear Time Invariant system (LTI) has been used. The use of this LTI requires the whole system of equations to be linear, which is why a linearisation was carried out as can be seen in Appendix A. During stick such an LTI-simulation was not necessary as the State Equations for stick (see Equation 4.20) are straightforward. This shortens the computation time needed to carry out the simulation. The model was programmed as such that it automatically alternates between stick and slip mode based on the occurring friction forces, the forces in the springs and the relative sliding velocity. This phenomenon has been explained in Section 4.1, and more extensively in Section 2.5. In the following Subsections 4.3.1 and 4.3.2 the output of the model for the four approaches as discussed in Sections 4.2.2-4.2.2 are shown and discussed. Each approach is modelled with the same parameters: an individual spring stiffness k of 20.17 N/m per spring, a mass of 0.67 kg, and a velocity of the slab in x-direction of 0.15 m/s. These are values used by Nuus (2018) as well.. Figure 4.5 below gives an overview of the output that the model generates. Upon reaching the threshold value of the static friction the model switches to slip mode indicated by the green background. Because of the uneven roughness of the rotating slab underneath the mass the friction force is not constant throughout the slip mode as can be seen in the graph in the top right corner in Figure 4.5. After the velocity of the mass matches with the velocity of the rotating slab in both direction and amount stick mode is resumed, and the process starts over again. This time the initial position P_t has changed with respect to the initial position P_{t-1} before this cycle.

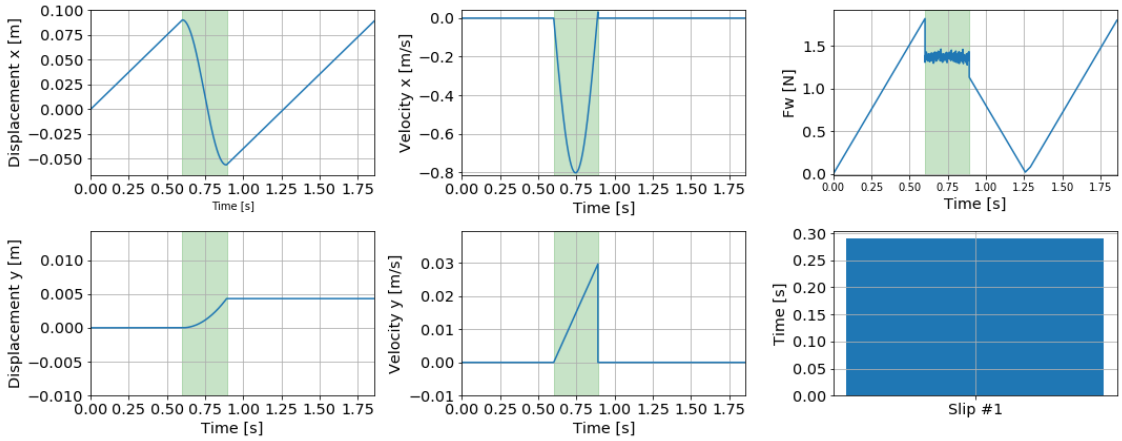

Figure 4.5: Generated output by numerical model. At t = 0s the mass starts in stick mode.

4.3.1. x-direction & rotation

The displacements in x-direction of the output of the derived model are presented in Figure 4.6a and the rotations ϕ in Figure 4.6b. The four labels correspond as such that *'Alpha1x'* represents the approach as described in Sub-subsection 4.2.2, etc. What becomes apparent from the comparison in 4.6a is that on the interval of t = [0 s,10 s] all four approaches show the same behaviour and there is no distinction between any of them. This verifies that when $\alpha = 0$ and constant the mass behaves as if it were a 1 DOF system (more about verification in Section 4.5). This again corresponds to the set of Equations 4.16 where the displacement in x is fully independent from the other two DOFs. In that system there is a minor contribution in the angular displacement due to the linearisation applied. All in all, this implies that the applied linearisation is justified and that no more alterations have to be made in order to make the numerical model comply with the experiment from Nuus (2018). When the mass does not rotate, and so $\alpha = 0$ and constant on this interval in all approaches, and only translates in both x- and y-direction, the mass and the springs remain aligned when disregarding the displacement in y-direction. The latter is justified as already explained in Sub-subsection 4.2.2. This explains why there is no rotation observed on that interval, which can be seen in Figure 4.6b. Nuus (2018) reported that a maximum rotation of 20°occurs, and that that is a significant enough rotation to not disregard it. Therefore, it is preferred to have a model that shows these significant rotations. Furthermore, she found that the rotations showed an oscillatory pattern. This pattern is only found in the fourth approach, with the updated αs, albeit that the amplitudes of the rotations are three times larger than the found rotations by Nuus (2018). The first three approaches do not show the oscillatory pattern, and also barely any rotations that match the maximum rotation found by Nuus (2018). On the interval t~[10s,15s] in Figure 4.6a the approach where the αs are updated shows a lower frequency of stick-slip occurrence, where the other three approaches remain almost identical. This can again be explained when looking at the rotations in Figure 4.6b. The rotation is initiated by uneven distributed friction forces caused by the uneven roughness of the slab (see Section 4.4 for how this is modelled). The first couple of cycles this unevenness did not cause enough imbalance, and so barely any rotation occurred, but after t = 10s this does cause an imbalance that is large enough and the mass starts to rotate. Now the mass rotates on top of the x- and y-displacements (for the latter, see Sub-section 4.3.2) which causes the springs and mass not to be aligned anymore. This results in uneven applied load by the springs. Hence, the imbalance is amplified, and so are the rotations. To clarify: the intervals in Figures 4.6a and 4.6b was chosen as such that it shows the behavioural differences that is of interest. If the interval of Figure 4.6a was set at the same interval of Figure 4.6b than no distinction between t~[0,10s] and t~[10s,40s] could have been observed. Secondly, the green background indicating slip mode in 4.5 has been left out in the Figures 4.6a - 4.6b as it would cloud the figures. This is done on purpose because these figures represent 40 cycles of stick-slip behaviour.

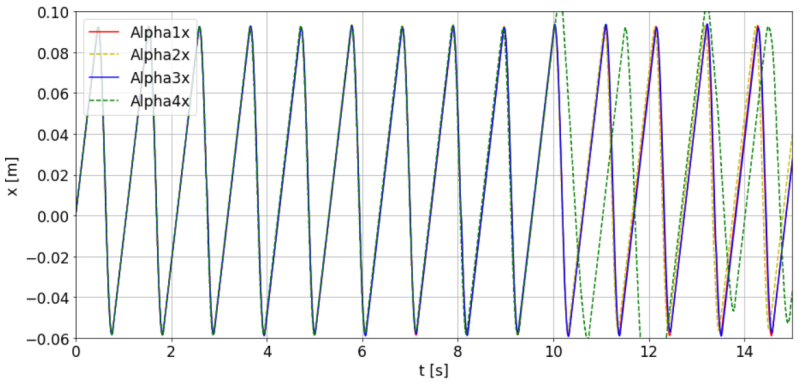

(a)

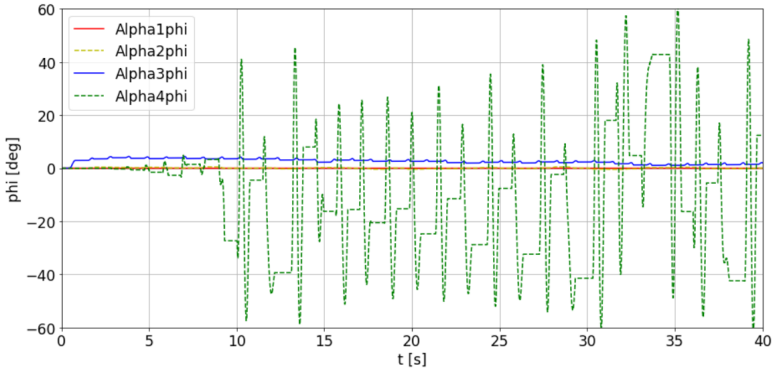

(b)

Figure 4.6: (a): Comparing x-direction of four different approaches, (b): Comparing rotation ϕ of four different approaches, with stiffness = 20.17 N/m, mass = 0.67 kg and slab velocity = 0.15 m/s

4.3.2. y-direction

In Sub-section 4.3.1 it was established that the behaviour in x-direction in the four approaches is the same on the interval t~[0,10s]. However, this similarity is completely not the case for the displacements in y-direction. Again the four labels correspond as such that *'Alpha1y'* represents the approach as described in Sub-subsection 4.2.2, etc. Naturally, for the approach where α = 0 and constant there is no displacement in y-direction. This is because when the α remains 0 no imbalance between the forces occurs, and so no vertical force component to push the mass in y-direction. When looking at the approaches with labels *'Alpha2y'* and *'Alpha3y'* it appears the mass keeps moving from the equilibrium and does not come back to it. From the set of Equations 4.17 and 4.18 it can be derived that the eigenfrequency in y-direction is much larger than the duration of slip mode during one stick-slip cycle. Because the αs in both approaches remain constant the springs keep exerting the same forces on the mass regardless of its position and angular orientation in the plane. Regarding the approach described in Sub-section 4.2.2 it becomes apparent in this approach the displacements in y-direction remain relatively close to the equilibrium position. This behaviour, in both frequency and amplitude, matches best the behaviour found by Nuus (2018). Unfortunately, the latter approach does require more computational time (5-8 minutes), compared to the former three approaches (all three around 20-30 seconds), as the set of Equations 4.19 has to be computed every timestep.

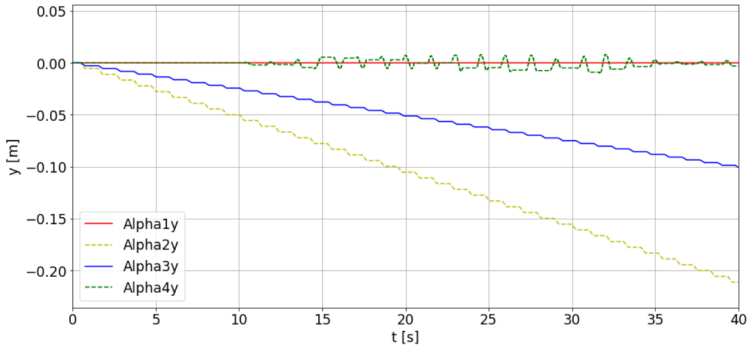

Figure 4.7: Comparing y-direction of four different approaches

4.3.3. Comparing Motion Modelling Approaches

To conclude this section the following remarks can be made:

- linearisation: as far as can be concluded at this stage the used linearisation in determining the Equations of Motions 4.16-4.19 is justified.
- x-direction: all four approaches show the same behaviour as long as the αs remain 0 and constant. When the latter no longer holds the approach in which the αs are updated shows a lower frequency and a slightly higher amplitude.
- y-direction: only the approach where the αs are updated shows the behaviour as expected.
- rotation: only the approach where the αs are updated shows significant rotations, whereas the other three approaches show little to no angular displacements. Based on the qualitative assessment of Nuus (2018) the significant rotations are likely to occur.
- The three approaches modelled in Subsections 4.2.2-4.2.2 took generally 20-30 seconds to run, whereas the approach modelled in Subsection 4.2.2 took generally 5-8 minutes to run.

All in all, the approach in which the αs are updates is the best approach to model the 3DOF behaviour that is researched. Hence, this model will be used in the remainder of this thesis. The additional computational time that comes along with this choice is taken for granted.

4.4 Modelling Friction Force

The friction force can be modelled in different approaches as well. This section outlines two approaches; in the first approach the friction force is modelled making use of the means and standard deviations found by Nuus (2018), and in the second approach the friction force is modelled based on the same data is mentioned in the former, but in this case the force is also based on the local instantaneous relative sliding velocity. Both approaches are modelled with the approach described in Sub-section 5.2.2.4..

4.4.1. Friction Force with Statistical Variation

To determine the friction force on the mass use has been made of the statistical data provided by Nuus (2018). With the provided means and standard deviations of the friction coefficients (both static and kinetic) a local friction pressure can be determined. According to statistical law the means and standard deviations of the friction coefficient can be linked to the means and standard deviations of the friction pressure as showed in Equations 4.24 and 4.25 (Dekking, 2005):

$$\mu_{force} = \mu_{stress} \frac{F_{normal}}{area} \qquad (4.24) \qquad\qquad \sigma_{force} = \sigma_{stress} \frac{F_{normal}}{area} \qquad (4.25)$$

The pressure is varied over the height of the mass and multiplied by its respective area. This gives a force per Δy. Figure 4.8 shows how the mass is divided into smaller areas and the distribution of the local friction force. Multiplying the local friction force with its respective area results in a higher friction force compared to the areas at the upper and lower edge of the mass. As the relative sliding velocity is in x-direction it was deliberately chosen to only divide the mass in parts along the y-axis instead of along both the y-axis *and* x-axis because it would save computation time without necessarily compromising the accuracy. In Figure 4.8 the mass is divided into 8 parts for illustration purposes, but in the numerical model the mass is divided into 100 parts to increase accuracy. The force distribution is summed up over the height to get the total friction force acting on the mass. In addition, the local friction force can be multiplied with its respective distance to the Centre of Gravity, and then summed up to get the moments about the z-axis. These summed up forces and moments are the input for the set of Equations of Motions, and can be found back on the right-hand sides in Equations 4.16-4.19 and 4.22.

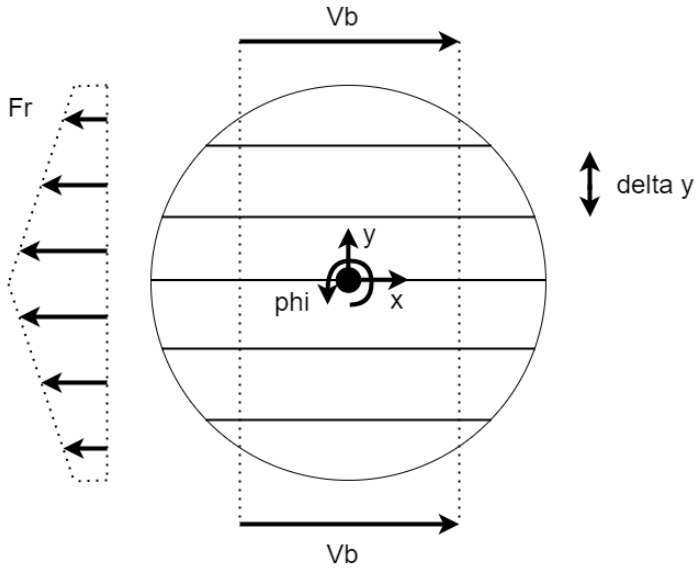

Figure 4.8: Force and Velocity Distribution over mass varying with standard deviation

4.4.2. Friction Force with Velocity Variation

The friction force can also be determined taking into account the difference in the relative sliding velocity along the y-axis. This difference occurs as a result of the rotating slab that the sample is on in the physical experiment conducted by Nuus (2018). As the upper edge of the sample is closer to the centre of rotation of the slab the local velocity is lower compared to the lower edge of the sample. This effect is mimicked in the second approach of modelling the friction force, and is schematised in Figure 4.9a. The linearly increasing velocity profile results in a decreasing friction coefficient over the height of the sample, and thus a decreasing friction pressure. When multiplying this with the respective area of the local force a force distribution shown on the right in Figure 4.9a results. The relation between kinetic friction and velocity is derived from findings from Nuus (2018), and is shown in Figure 4.9b. Because only four data points are provided an estimated guess had to be made as to the nature of the relation, hence a linear decreasing trend was chosen. The literature as presented in Sub-section 2.6.3 presents no clear relation between the velocity interval used in this thesis and the kinetic friction coefficient. This was already visualised in Figures 2.13 and 2.12. The disagreement among the different researchers and their work only amplifies that the current theoretical framework of dry friction is not conclusive.

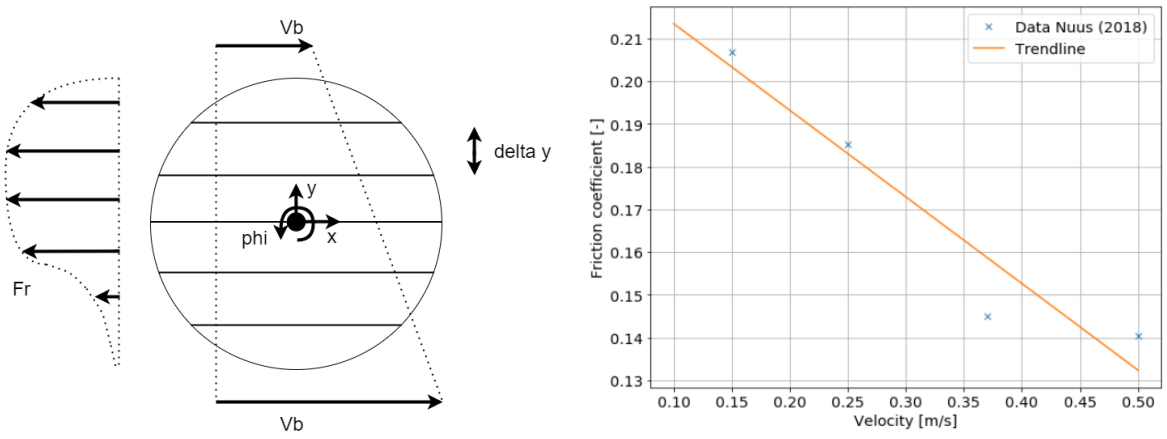

(a) (b)

Figure 4.9: (a): Force and velocity distribution over mass varying with velocity, (b): Inverse linear relation between slab velocity and kinetic friction coefficient (Nuus, 2018)

4.4.3. Comparing Friction Modelling Approaches

When comparing the two approaches as described in Sub-sections 4.4.1 and 4.4.2 both the friction force as input of the numerical model, as well as the occurring slip times as output of the numerical model will be looked at. In Figure 4.10 the input of the numerical model for both approaches is presented. The first approach where the friction force is determined based on statistics provided by Nuus (2018) is labelled *Fr(sigma)*, and the second approach where the friction force is determined based on the varying velocity over the y-axis is labelled *Fr(velocity)*. It appears that the static friction force threshold (before switching into slip mode) in the first approach is not consistent throughout all cycles. Hence, the static friction force threshold in the first approach is sometimes higher compared to the second approach. This is due to the fact that with each cycle the static friction coefficient is determined again based on the mean μ and standard deviation σ. Secondly, during slip the kinetic friction force in the first approach swings about the mean kinetic friction force, again due to the use of statistical determination of the friction force. In the output generated by the second approach the friction force decreases before it increases again towards the kinetic friction force as determined in the first approach. This is due to the decreasing and increasing relative sliding velocity of the mass over the slab. Upon initiation of the slip mode the mass slows down and starts moving in negative x-direction as the springs push/pull the mass into that direction. As it moves through the equilibrium position the total force exerted by the springs switch direction, again slowing down the mass and eventually pushing/pulling the mass again into positive x-direction. At a certain moment the velocity of the mass and the slab are equal in both direction and size, and the mass switches from slipping to sticking. The trajectory is presented in Figure 4.11.

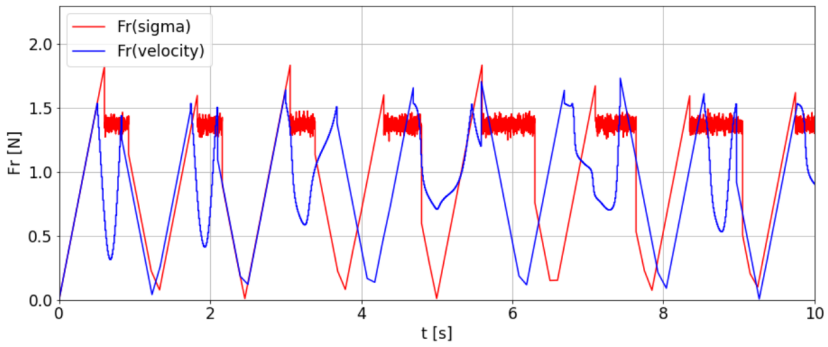

Figure 4.10: Comparing friction forces of the two different approaches

Thirdly, the friction force in both approaches reach a point where the friction is 0 N. That is because the mass passes its equilibrium position during stick, at which the springs exert no force on the mass and the mass and rotating slab move as one entity. During slip however, this does not hold. When the mass is moving through its equilibrium position and the springs exert no force on the mass, there is still a force imbalance due to the relative sliding velocity between the moving mass and rotating slab not being 0 m/s. Hence, the friction force does not reach a point where it is 0 N. In addition, because of the timesteps used in the numerical model the graphs in Figure 4.10 do not always reach 0 N exactly.

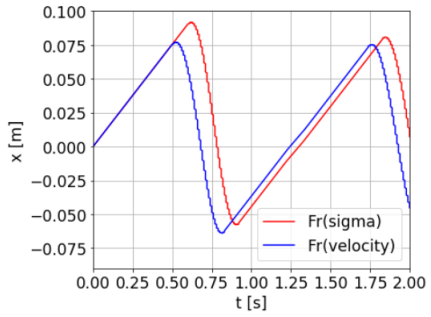

Figure 4.11: Comparing displacements in x-direction of the two different approaches

When comparing the slip times of both approaches in Figure 4.12 it appears that the second approach has generally longer slip times. The cause of this is again the downfall followed by the rise of the friction force as a consequence of the downfall and rise of the velocity in x-direction as already discussed. Again, this can be seen in Figure 4.10.

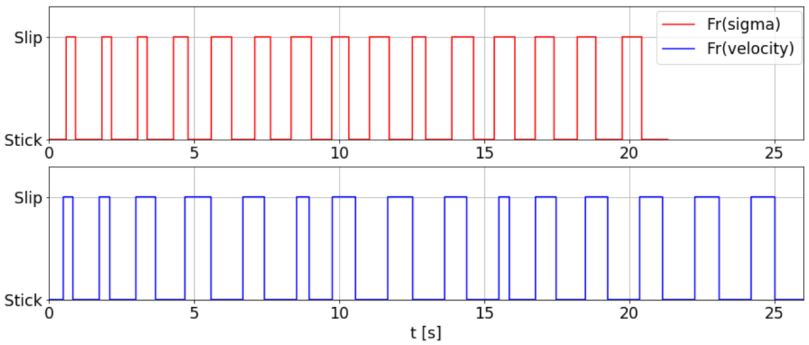

Figure 4.12: Comparing slip times of the two different approaches

4.5 Model Verification

To verify the established model simple checks have been carried out to see if the output of the model under simplified circumstances corresponds with what can be expected based on theory. These verifications have been carried out with for the slip mode simulation, since for the stick mode the model consists only of a straightforward force equilibrium in x-direction.
Figure 4.13 below presents the displacements in x-direction in slip mode when the stiffness of the springs is 0. The initial conditions for all three DOFs and their respective time derivatives have been set to 0. Due to the friction force in x-direction it is to be expected that the mass will move in positive x-direction towards infinity. Figure 4.13 shows that this is true.

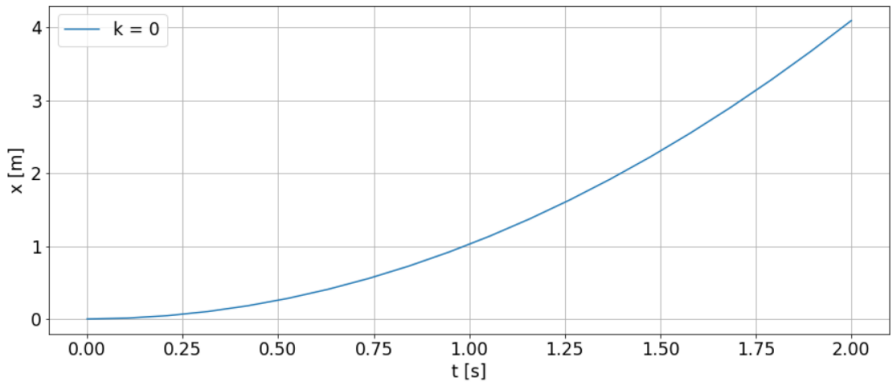

Figure 4.13: Model verification with k = 0

The opposite of what has been discussed above, and illustrated in Figure 4.13, should be true as well. Meaning that when $k \to \infty$ the displacements in x-direction should be 0. When the stiffness of the springs $k \to \infty$ the mass is kept in its equilibrium position at all times as no significant force is strong enough to overcome the restoring forces in the springs. Hence, no displacements are to be expected. Figure 4.14 shows that this is true. Due to the numerical calculations Figure 4.14 does show small variations around the equilibrium position, but these are not significant and can be regarded as 0. Again, the initial conditions of the model have been set at 0 and only the slip mode is considered. For this verification a stiffness of 9999 N/m was used, which is more than one hundred times larger compared to the maximum stiffness of 69.83 N/m used in this thesis and used by Nuus (2018).

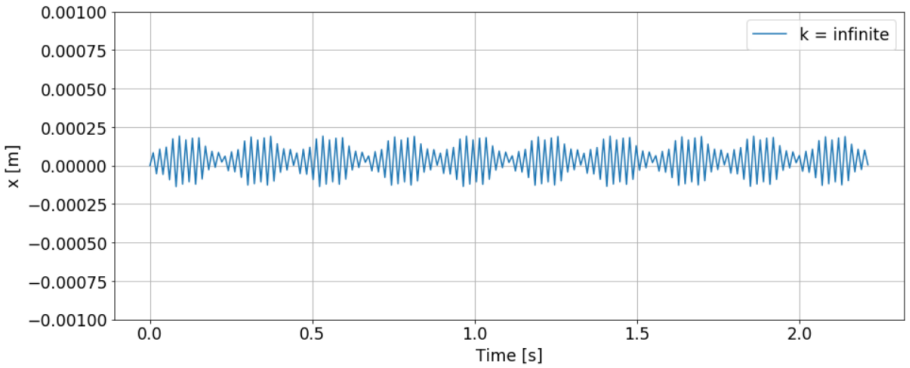

Figure 4.14: Model verification with $k \to \infty$

In the next verification step the mass was given an initial offset in x-direction and the remaining initial conditions were set at 0 as well as the friction force during slip. In this case the mass should move like a 1DOF mass-spring system, and remain in slip mode for $t \to \infty$. As there is no damper within the created model the mass should move with its natural frequency, and should continue to do so when $t \to \infty$. In y-direction there should not be any displacements as the mass does not leave its equilibrium position in y-direction, and does not experience a force in that direction as well. Figure 4.15 shows the output generated by the numerical model. It clearly shows that the output corresponds with the expectations.

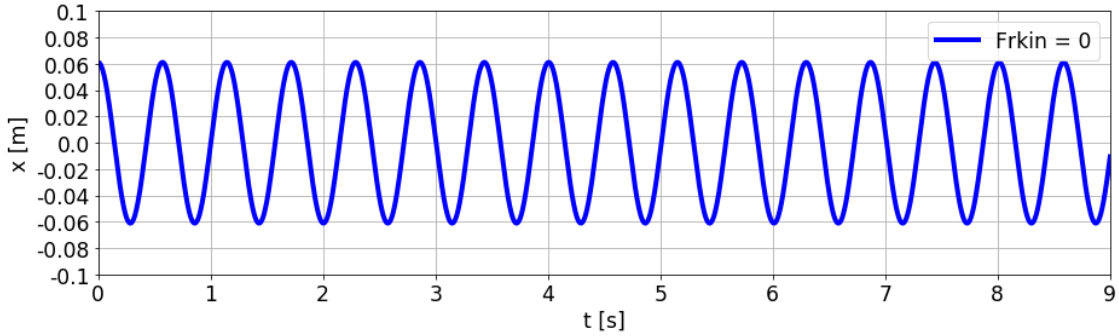

Figure 4.15: Model verification in x-direction with F_{kin} = 0 and k = 20.17 N/m.

All in all, all the described verifications show that the created numerical model generates output that is exactly what can be expected based on the theory of more simplified models.

4.6 Model Validation

4.6.1. Dry/Hydrodynamic Friction

The model as set up in this Chapter is based on the assumption that the occurring friction can be considered dry friction, as described in Sub-section 2.2.1. However, as explained in Section 2.3, melting of ice occurs due to frictional heating. In addition, as described in Sub-section 2.2.2 - 2.2.4, a lubricating layer exists on the ice-structure interface. This lubricating layer exists with and without frictional heating having occurred, and exists for temperature up to as low as -140°C. All these arguments reduce the validity of the dry friction assumption. During experiments conducted by Nuus (2018) the ice sample was inspected before and after the test run, and it was concluded that no surface melting had occurred. Furthermore, if friction heating would have had a significant impact, and as a result the interface would have been fully lubricated (*hydrodynamic friction*, Sub-section 2.2.4), no stick would have occurred during the test run. As was concluded by Nuus (2018), and also found in the preliminary results of the numerical model presented in this thesis, stick does occur frequently. This implies that the assumption of dry friction is valid for numerical modelling.

4.6.2. Static Strengthening

In Section 2.4 it was shown that when during stick the static friction increases. This is known as static strengthening. It was shown that this effect could be considerable when the holding time multiplied with the relative sliding velocity is larger than 10^{-4} m. With the lowest relative sliding velocity in this thesis being 0.15 m/s, the holding time would have been larger than or equal to $6.67 * 10^{-4}$ s to match that value. During experiments conducted by Nuus (2018), and the preliminary results of the numerical model presented in this thesis, it can be concluded that those holding times during stick do occur. This means that the static strengthening component discussed in Section 2.4 was wrongly not included in the modelling.

Assuming static strengthening does occur Nuus (2018) states that the friction coefficients resulting from the experiments and the presented numerical model, were determined based on the *final* friction coefficients. This means that, although the static strengthening component was not deliberately incorporated in the numerical model, the results are still valid due to the fact that static strengthening is implicitly taken into account.

4.6.3. Comparing Displacements

The numerical model as presented in this thesis has the results of the experiments and numerical 1DOF model of Nuus (2018) incorporated. This means that the μ_{static} and $\mu_{kinetic}$ determined by Nuus (2018) are used to determine the friction forces in the new 3DOF model. For the comparison between the aforementioned research, and this thesis, the friction force was modelled using the approach as discussed in Subsection 4.4.1 as this approach is similar to the approach used in the 1DOF model created by Nuus (2018). With this a comparison between the displacements and rotations of the 1DOF and 3DOF model can be made. Figures 4.16a & 4.16b show the mean displacements in x-direction of the 3DOF model and the experimt carried out by Nuus (2018). When comparing The 3DOF model (on the left) with the experimental data of Nuus (2018) (on the right) it can be seen that the 3DOF model overshoots the displacements in x-direction as the means are larger. This can be attributed to the following: with the rotations and y-displacements incorporated in the Equations of Motions the mass is not always completely aligned with the springs. That means that the springs exert their force under an angle, which leads to a lower force in x-direction. This results in lower resistance for the mass to move in x-direction during slip, and so larger means and standard deviations in x-direction occur compared to the experimental data. Also, because of the process that has just been described, the means of the 3DOF model seem more random, and the linear fashion in the experimental data of Nuus (2018) is less visible in the data from the 3DOF model. Only the mean displacements in x-direction in Figure 4.16b show more coherence. This is important as x-direction is the dominating degree of freedom in this system. This can be derived from the Equations of Motions 4.16-4.18.

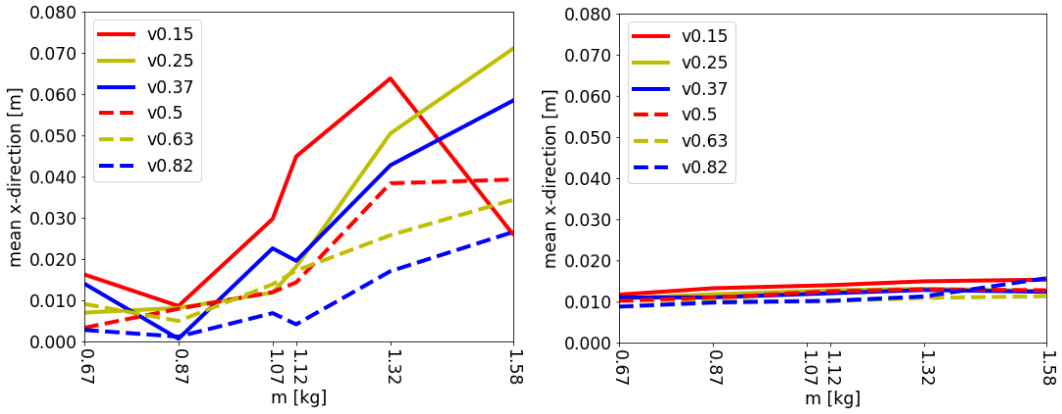

(a) 3DOF model x_{mean} displacements

(b) Nuus (2018) experimental data x_{mean} displacements

Figure 4.16: (a, b): Comparison between 3DOF model and experimental data from Nuus, with stiffness = 38.50 N/m. The label 'v0.15' corresponds to the dataset with 0.15 m/s slab velocity in x-direction, etc.

Results shown in Figures 4.16a & 4.16b clearly indicate that the created 3DOF model overshoots the experimental data. Nevertheless an upward trend is clearly visible in Figure 4.16a, and the same goes for the experimental data shown in Figure 4.16b, which means that there is some resemblance, but not enough to state that the model is validated. To see what causes the difference between the 3DOF model and the experimental data from Nuus (2018) a closer look is taken at a single run of the 3DOF model compared to a single run of the experiment.

When looking closer at a single run of the 3DOF model versus the experimental data (see Figure 4.18a) the overshoot is also visible. Apparently, there exist a Δ_x between the amplitudes of the two sets of data. The amplitude from the 3DOF model is higher than the amplitude of the experimental data. Also, there exists a Δ_t between the periods of the two sets of data; the period of the experimental data is smaller than the 3DOF model. A reason for this could be the kinetic and static friction coefficients that were used in the 3DOF model. The coefficients used in the 3DOF model were derived from the results provided by Nuus (2018), as was explained in Section 4.4. An explanation for these Δ_x and Δ_t could be that less friction occurs than was initially thought, which is also found in literature (Itoh et al., 1988). It states that there is a range in between which the static and kinetic friction coefficients of concrete lie. Lower friction would lead to lower excitations, and less built-up of forces in the springs. Lower forces in the springs would lead to a softer push-back of the mass from the excited position towards the equilibrium position, this would make the displacement curve less steep. In addition, lowering the friction would also extend the slip times that would occur. From the data provided by Nuus (2018) it is known the mass is in slip mode 90%-95% of the time. So all in all, lowering the friction coefficients should make the 3DOF model represent better the dynamic behaviour found in the experimental data. After lowering the friction coefficients by 75% (i.e. from μ_{static} = 0.28 to 0.065, $\mu_{kinetic}$ = 0.20 to 0.05) the 3DOF model provides output that better resembles the amplitudes and periods found in the experimental data, this is shown in Figure 4.18b. The focus of the validation is on the amplitudes and periods of the 3DOF model. To be able to closer examine the dynamics of the model the mean displacement of both the experimental data and the numerical data was subtracted. Also, the numerical data was shifted in time to better show the comparison between the numerical data and the experimental data. This results in Figure 4.18c. This figure shows how well the developed 3DOF numerical model fits the dynamics observed during the experiment.

It should be noted that the mean displacements of the 3DOF model does not coincide with the mean displacements found in the experiment, but the mean displacements of the 3DOF model are now closer to the mean displacements found in the experimental data (see Figures 4.17a & 4.17b) and this is considered an improvement. In Figures 4.16a & 4.16b the difference in mean displacements between the two datasets was much larger compared to the difference between the two datasets in Figures 4.17a & 4.17b. The 3DOF model with the new friction coefficients deviates the least from the experimental data in terms of the amplitudes and periods of the time series.

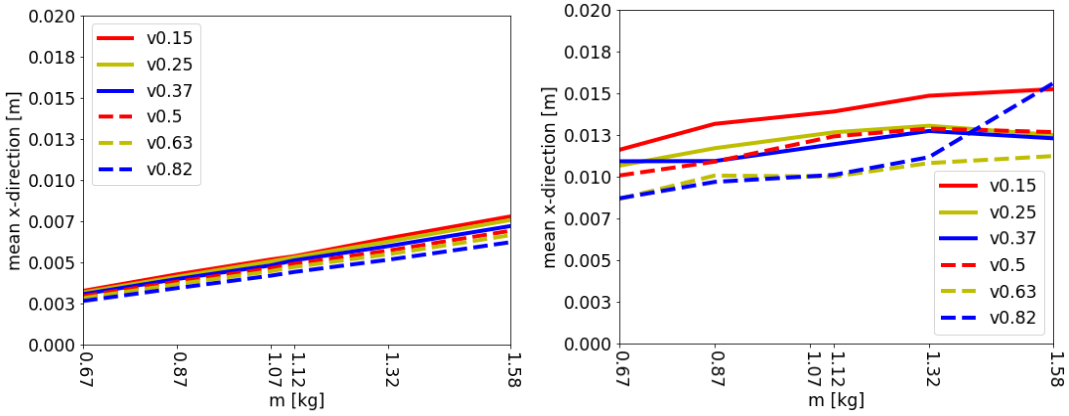

(a) 3DOF model x_{mean} displacements

(b) Nuus (2018) experimental data x_{mean} displacements

Figure 4.17: (a, b): Comparison between 3DOF model and experimental data from Nuus, with stiffness = 38.50 N/m. The label 'v0.15' corresponds to the dataset with 0.15 m/s slab velocity in x-direction, etc.

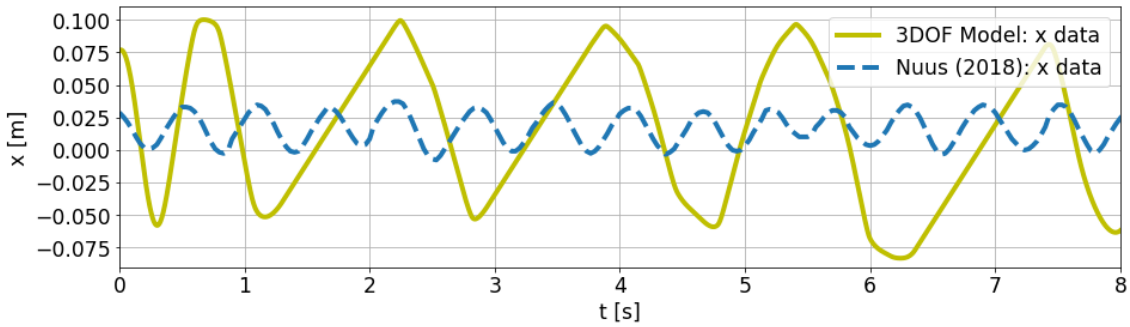

(a) x-displacements of 3DOF Model with friction coefficients as determined by Nuus (2018)

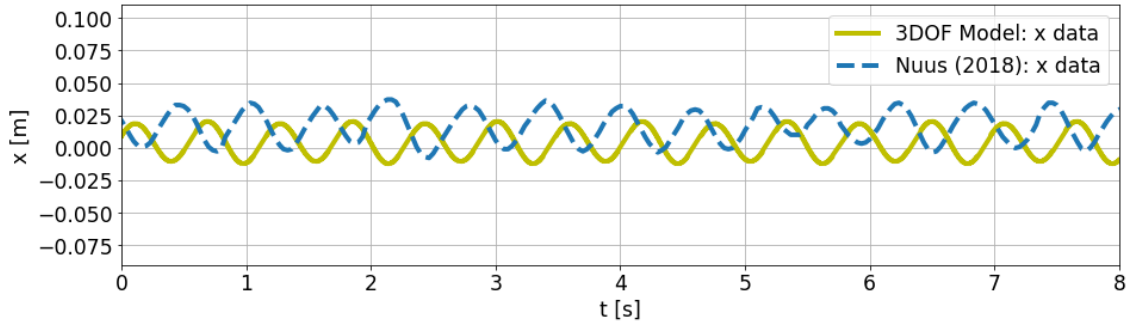

(b) x-displacements of 3DOF Model with newly determined friction coefficients. Friction coefficients are 25% of the friction coefficients as determined by Nuus (2018)

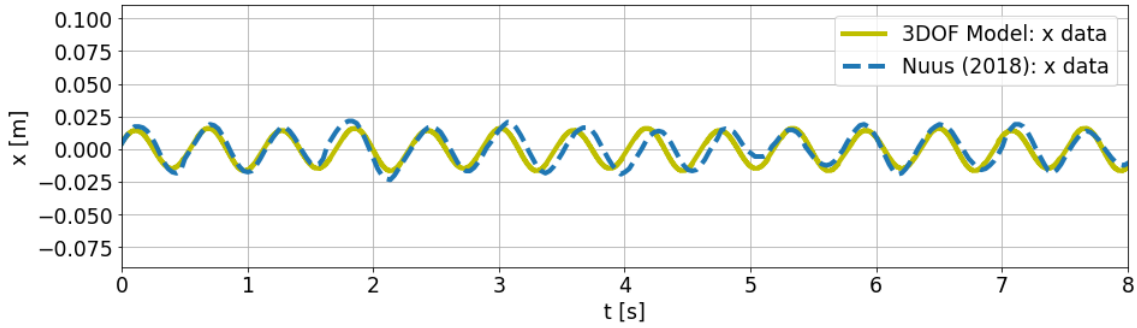

(c) x-displacements of 3DOF Model with newly determined friction coefficients. Experimental data is shifted in place (Δ_x = 0.02 m) and time (Δ_t = 0.33 s), and the numerical data is shifted in place (Δ_x = 0.004 m) to better compare the dynamics of the experimental data and numerical data.

Figure 4.18: (a, b,c): Comparison between the 3DOF model with friction coefficients as determined by Nuus (2018), and newly determined friction coefficients, with stiffness = 20.17 N/m, mass = 0.67 kg and slab velocity = 0.15 m/s. The axes of the three figures is kept the same intentionally. This is to better compare the three figures with one another.

To further clarify, the phase lag between the 3DOF model x data, and the x data from Nuus (2018) comes from the fact that both timeseries are in their steady-state regime. Therefore, it is allowed to shift the x data from Nuus (2018) in time to create a better comparison between the two sets of x data. The shifted timeseries is shown in Figure 4.18c.

From now on the results with the 3DOF model using the friction coefficients as determined by Nuus (2018) will be called dataset #1, and the results with the 3DOF model using the newly determined friction coefficients will be called dataset #2.

In Figures 4.19a & 4.19b the results of dataset #2 are presented for the displacements in both x- and y-direction. Again, the focus here lies on the dynamics of the sample, so on the amplitudes and the periods. The displacements shown are from the same run of the 3DOF model, so with the same set of parameters used. At first the 3DOF model shows no noticeable y-displacement. This is still the start-up phase. During that phase the periods of the occurring x-displacements are smaller than the experimental data, and the amplitude is smaller too. However, once the imbalance becomes more apparent, and the mass starts to move in y-direction as well, the displacements and periods in both x- and y-direction match with the experimental data. The imbalance in forces of the four springs occurs due to the independent displacements/rotations of the four springs. This causes the springs to be unaligned and results in an additional force in y-direction and an additional moment about the z-axis, which in turn causes y-displacements and rotations. That is how the imbalance leads to y-displacements and rotations on top of the already occurring x-displacements. The vertical bar indicates the transition from only 1D behaviour (with only displacements in x-direction) to 2D behaviour (with displacements in both x- and y-direction). It is that latter 2D behaviour that is exactly what this 3DOF model was created for. This validates the earlier statement that was made in Subsection 4.3.1 in Figure 4.6b where it was indicated that the model in which the αs were updated every iteration first initially behaves as a 1DOF model (where only x-displacements occur) and later on, when the imbalance is stronger, the 3DOF model shows 2D behaviour.

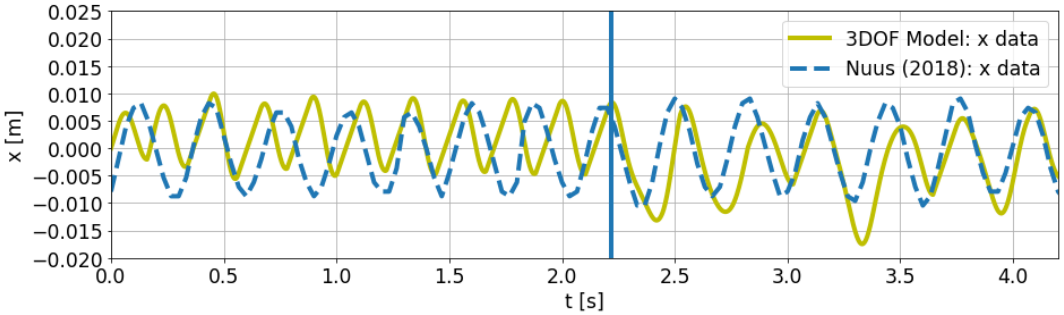

(a) Comparison between upgraded 3DOF model and experimental x data Nuus (2018). The start-up phase of dataset #2 is presented, but not the start-up phase of the experimental data to show the difference between start-up and steady-state of dataset #2

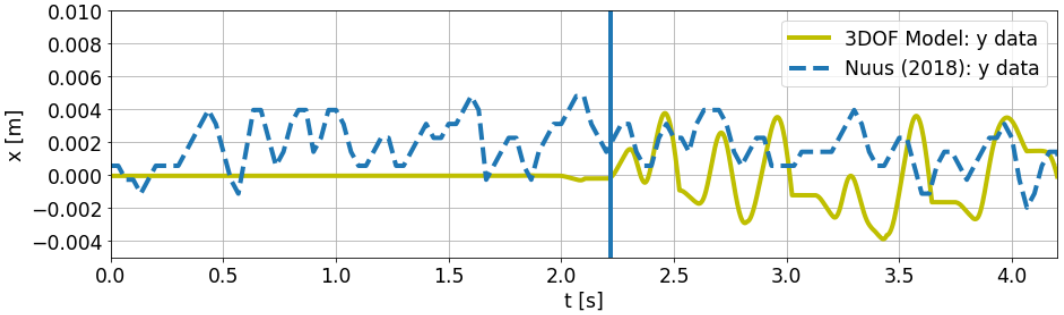

(b) Comparison between dataset #2 and experimental y data Nuus (2018). The start-up phase of dataset #2 is presented, but not the start-up phase of the experimental data to show the difference between start-up and steady-state of dataset #2

Figure 4.19: (a,b): displacements in x- and y-direction with k = 68.22 N/m, v = 0.15 m/s, m = 0.67 kg

To further clarify, as already said when the mass starts moving in y-direction and starts rotating the springs are no longer aligned and not completely horizontal. When this happens the springs are placed under an angle compared to their original position. Because the springs now exert a force under an angle the contribution of that spring force in x-direction is lower when compared to the case where the springs were in its original horizontal position. This means that total horizontal force that pushes the mass back towards it's equilibrium position is also lower. This lower horizontal force allows the mass to have a behaviour with larger amplitudes in x-direction and also longer periods. This is an explanation for the difference in the x-displacements that can be seen on the left and on the right of the vertical bar in Figure 4.19a.

4.6.4. Comparing Rotations

The data as provided by the research Nuus (2018) conducted only includes x- and y-coordinates of the moving ice sample. This means that only the location of the ice sample within a frame is obtained, but not the degree of rotation. Therefore, a validation of the 3DOF model cannot be carried out for the rotations. The only thing Nuus (2018) concluded was that on average, so throughout all the tests she carried out, a maximum rotation of 20°was observed. Nuus (2018) does not report findings of the rotational speed of her ice sample. The maximum rotation as found by Nuus (2018) is illustrated in Figure 4.20 on the right, where the circle represents the ice sample and the red box represents the tracker. With this tracker the x- and y-coordinates could be retrieved through analysis of the videos that she shot throughout the experiments.

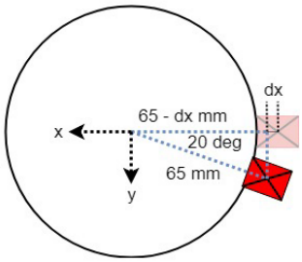

Figure 4.20: Average maximum rotation (Nuus, 2018)

In Figure 4.21a the rotations of a single run of dataset #1 is shown, and in Figure4.21b the rotations of dataset #2. It shows that in dataset #1 a maximum rotation of 150°anti-clockwise, and 120°clockwise occurs. This demonstrates that the rotations as found in the 3DOF model overshoot the actual occurring rotations that were observed during the experiment of Nuus (2018). In Figure 4.21b it can be seen that dataset #2 matches the maximum rotations as found by Nuus (2018). Again, the sliptimes in dataset #2 are longer compared to dataset #1, which matches with Nuus' (2018) findings.

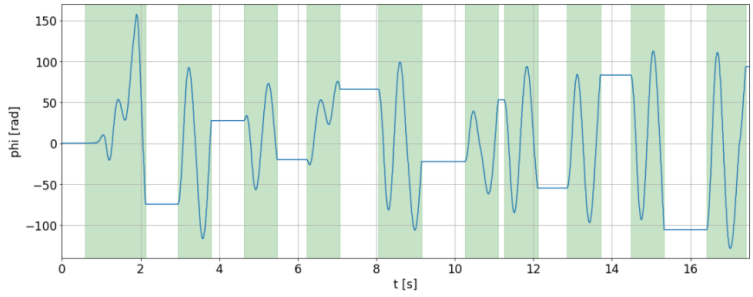

(a) dataset #1

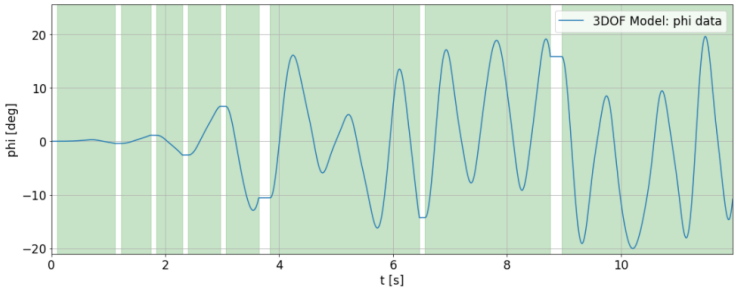

(b) dataset #2

Figure 4.21: (a, b): Comparison between dataset #1 and dataset #2, with stiffness = 20.17 N/m, mass = 0.67 kg and slab velocity = 0.15 m/s. The green background indicates slip mode

The maximum angular speed at which these rotations occur are calculated as follows:

$$\omega_{Initial} = \frac{|\phi_{T2} - \phi_{T1}|}{T_2 - T_1} = \frac{|150° - (-70°)|}{2.05s - 1.8s} = 880°/s \tag{4.26}$$

$$\omega_{Upgraded} = \frac{|\phi_{T2} - \phi_{T1}|}{T_2 - T_1} = \frac{|13° - (-15)°|}{6.1s - 5.6s} = 56°/s \tag{4.27}$$

Because Nuus (2018) does not report any findings on the angular speed no conclusions can be derived from this. However, this maximum angular speed as calculated in Equation 4.26 is assumed to be too high, though the maximum angular speed as calculated in Equation 4.27 seems more reasonable.

Based on the comparisons between dataset #2 and the experimental data provided by Nuus (2018) and the findings mentioned from literature the 3DOF model that resulted in dataset #2 is validated. This means that the friction coefficients as determined by Nuus (2018) are overestimated, and that friction coefficients of 75% less should be used to model the experiment Nuus (2018) conducted.

Chapter 5

Sensitivity Analysis of 3DOF Numerical Model

In this Chapter a sensitivity analysis is carried out to assess the sensitivity of the three degree of freedom (3DOF) numerical model on the used parameters. The set of parameters used are the same as the set of parameters that would have been used in the physical experiment as explained in Chapter 3.4. Also, this set of parameters corresponds to the set of parameters used by Nuus (2018) to be able to compare the results from the sensitivity analysis of the 3DOF numerical model with the findings presented by Nuus (2018). In Section 5.1 the 3DOF model is analysed based on the mean displacements in x-direction. In Section 5.2 the 3DOF model is analysed based on the slip times versus the slab velocity. An explanation of the slip times can be found in that Section. In Section 5.3 the kinetic friction coefficients found with the 3DOF model are analysed. During slip the dynamic behaviour of the mass in combination with the springs is seen in the output of the model. That is why the focus is put on the kinetic friction, rather than the static friction. The static friction is of less interest as the mass and rotating slab are in a static equilibrium, and the displacements of the mass coincide with the rotation of the slab.

As already established, and explained in Subsection 4.3.1, the created 3DOF numerical model starts with initial conditions all zero, apart from the velocity in x-direction (which is equal to the slab velocity). This leads to a start-up phase in which the imbalance in y-direction is not yet occurring. Only when this imbalance occurs the behaviour found in the 3DOF numerical model matches with the experimental data (Nuus, 2018). This phase is referred to as the steady-state. Findings presented in this Chapter often refer to the mean of displacements, rotations or forces. The reader should bare in mind that these values are derived from the steady-state phase of the 3DOF numerical model. Practically, this means that roughly the initial 10 cycles of the output is not considered, but only the 15 cycles of steady-state behaviour. Generally and if not explicitly stated otherwise, when in figures presented in this chapter the x-axis starts at t = 0 s, this is the start of the steady-state regime, and not the actual start of the 3DOF numerical model.

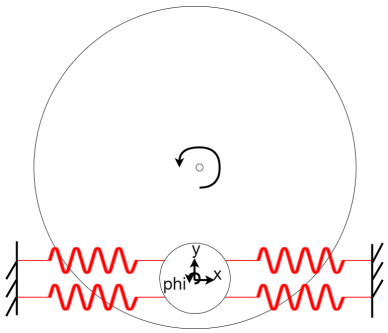

Figure 5.1: Top view of the ice sample on top of the rotating slab. Both figures show the model in *xy*-frame

Again, for the benefit of the reader the degrees of freedom as well as the orientation of the springs are illustrated in Figure 5.1.

5.1 Influence of Parameters On Displacements

In this Section the 3DOF numerical model is analysed based on the mean displacements in x-direction in the steady-state regime. The goal of the analysis in this Section is gain to insight into the effects of the involved parameters (mass, stiffness and slab velocity) on the mean displacements in x-direction. The results are presented below in Figures 5.2a-5.2d.

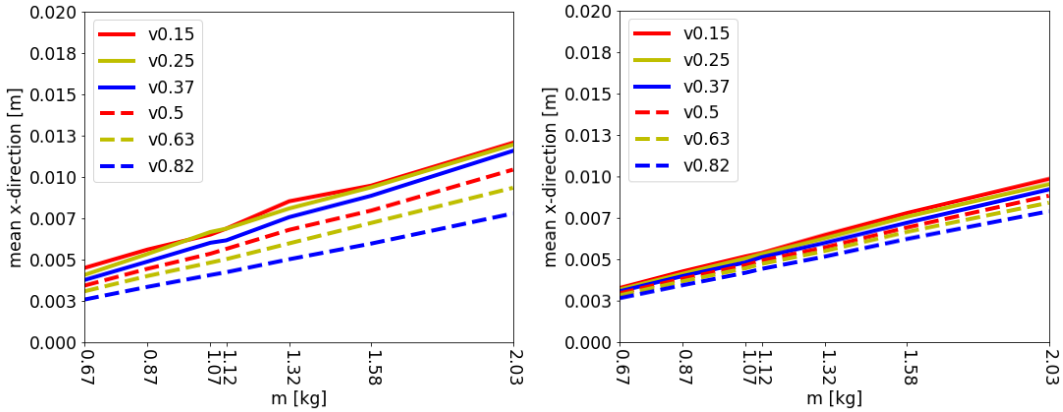

(a) x_{mean}, with stiffness = 20.17 N/m

(b) x_{mean}, with stiffness = 38.50 N/m

(c) x_{mean}, with stiffness = 49.83 N/m

(d) x_{mean}, with stiffness = 68.22 N/m

Figure 5.2: (a, b, c, d): mean displacements in x-direction for different stiffnesses the label 'v0.15' corresponds to the dataset with 0.15 m/s slab velocity in x-direction, etc. The range of the y-axes in all Figures are kept the same in order to easier compare the results per stiffness with each other. Hence, the graphs may look slim.

In all Figures 5.2a-5.2d the mean displacement in x-direction increases linearly with increasing mass. This can be attributed to the higher inertia of the mass. The higher the mass the higher the occurring friction forces and the higher the forces needs to be built up in the springs to overcome the inertia and reverse the motion of the mass. This linearity is based on seven datapoints per slab velocity. To show that this linearity does in fact occur, a further analysis has been performed to see if that really is the case. For the testing of this hypothesis the following set of parameters was used: stiffness = 38.50 N/m and slab velocity = 0.37 m/s and mass = [0.1 kg, 3.1 kg] with steps of 0.2 kg. The stiffness and slab velocity were chosen as such because they are roughly in the middle of the entire set of parameters used in this sensitivity analysis which ensures that for the highest or lowest parameters the outcome would not differ too much from this second analysis. The mass was increased with steps of 0.2 kg to get enough datapoints to be able to make a conclusion regarding the relation.

In Figure 5.3 the results are shown. It shows that the relationship is in fact linear, and the hypothesis is therefor true.

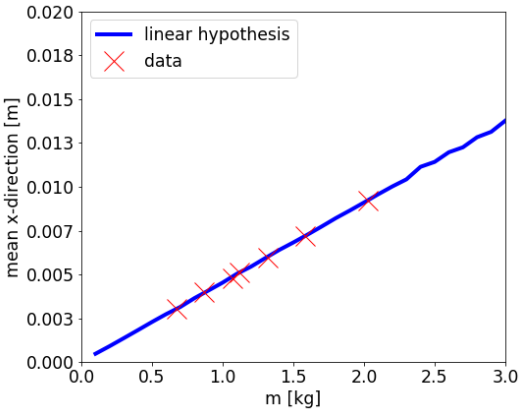

Figure 5.3: x_{mean}, with stiffness = 38.50 N/m and slab velocity = 0.37 m/s. The "Linear Hypothesis" shows the data from the hypothesis analysis, and the "data" shows the seven datapoints from the initial dataset.

In Figure 5.2a the undashed lines lie underneath the dashed lines. This indicates that the faster the concrete slab rotates the smaller the mean excitations in x-direction are. The same trend can be observed in other figures, but it is less obvious. When the velocity of the slab is higher the velocity of the mass during stick is also higher (since they are the same during slip, and the relative sliding velocity is zero). The higher the velocity the higher the indentation depth of the spring. This bigger indentation depth causes for higher spring forces, and hence, a faster push back towards the equilibrium position. This also leads to higher relative sliding velocity in absolute terms. The mass continues moving until the mass is at the spring on the other side (so at negative x position). Here, because of the higher relative sliding velocity the springs are again indented deeper, compared to the case where the slab velocity is lower. Hence, the path the mass has traveled is larger with higher slab velocity, see Figure 5.4 for an illustration of these paths. This means that the amplitude of the oscillatory movements increases with increasing slab velocity. Also, because of the deeper indentation of the springs on the negative x position this means that when deriving the mean displacement it is found that that mean displacement lies closer to the equilibrium position with increasing slab velocity.

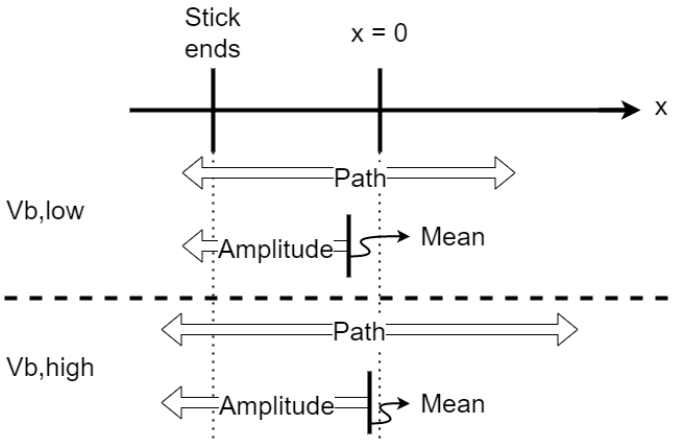

Figure 5.4: Comparison between the influence of low and high slab velocities on the means and amplitudes in x-direction.

In Figure 5.2d the mean x-displacements of the runs with the higher slab velocities deviate from the pattern found in the other three figures. In Figure 5.5 below a single run of one of these three is shown. It shows that after several cycles (in steady-state) an anomaly occurs. Apparently, at t ≈ 6.2 s the mass abruptly starts moving in the opposite direction, which is the same direction as the rotating slab. before this moment, the mass was in slip mode, but at t ≈ 6.2 s the model determined that the relative sliding velocity of the mass became zero. Therefor, the mass switched from slip to stick mode, which explains why the mass suddenly moves along with the rotating slab. It may very well be true that the relative sliding velocity reaches a value of 0 at this moment, though it is only found three times in the entire dataset, but the inertia of the mass should have made the behaviour more fluent if this really were to happen, and not so abruptly like in Figure 5.5. This anomaly is also found with the two other deviating runs (with slab velocities of 0.63 m/s and 0.82 m/s). Because of this anomalies the mean x-displacements for these three slab velocities with a stiffness of 68.22 N/m and a mass of 2.03 kg, are slightly over estimated, hence the deviation in the pattern in Figure 5.2d.

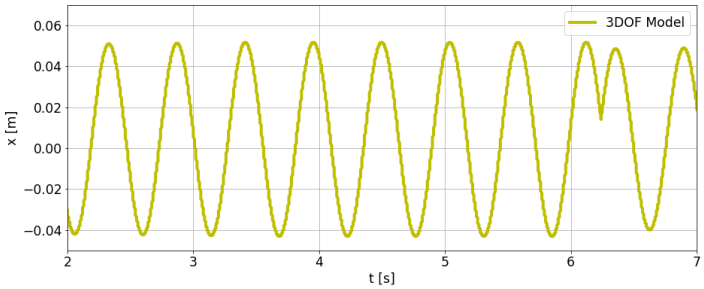

Figure 5.5: Single Run with stiffness = 68.22 N/m, mass = 2.03 kg and slab velocity = 0.50 m/s

When comparing the x-displacements versus the stiffness the following is found: in Figure 5.2a the stiffness is lowest and the mean x-displacements are highest, but in Figure 5.2d the stiffness is highest and the mean x-displacements are lowest. This means that the higher the stiffness, the less x-displacements occur. This is plausible as the higher stiffness causes the threshold of the static friction to lie closer to the equilibrium position:

$$x_{threshold} = \frac{F_{static}}{k} \tag{5.1}$$

So the higher the stiffness, the smaller $x_{threshold}$. Meaning that slip mode is initiated closer to the equilibrium position.

5.2 Influence of Slab Velocity on Slip Times

In this section the slip times versus the slab velocity are analysed. The slip time is the amount of time the mass is on average in slip mode. It is the mean of slip times of all occurring slip modes per run. For this analysis a mass of 0.67 kg and a stiffness of 20.17 N/m was selected. There is no reasoning behind this selection. The slab velocity was varied from 0.15 m/s to 0.82 m/s with a step of 0.1 m/s. The goal of the analysis in this Section is to gain insight into the effects of the slab velocity on the slip times of the mass. The results are shown in Figure 5.6.

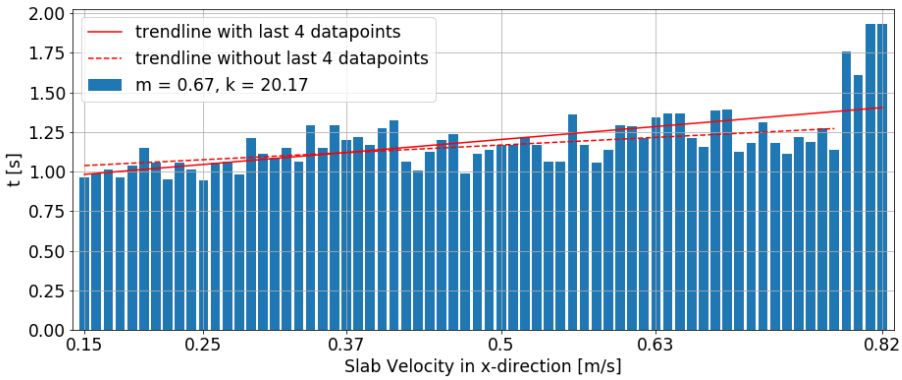

Figure 5.6: Slip Times versus Slab Velocity for range v = [0.01,0.5] m/s, mass = 0.67 kg and stiffness = 20.17 N/m

In Figure 5.6 the slip times increase for higher slab velocities. This can be attributed to the slab rotating faster, and hence building up more forces in the springs when compared to lower slab velocities. These higher forces push back the mass faster.

The high springs forces push the mass back faster in opposing x-direction, and the motion is reversed, and the relative sliding velocity is decreased. At all times during slip mode the relative sliding velocity is lower than the slab velocity. If the slab velocity is increased the gap between the relative sliding velocity and the slab velocity is larger compared to a lower slab velocity, see Figure 5.7. The larger the gap the longer it takes for the relative sliding velocity to decrease back to zero again, at which point stick mode is resumed.

Even when the 4 highest values for v = [0.79 m/s,0.82 m/s] are treated as outliers, and removed from the trend-line, the trend-line still shows an increasing slip time with increasing slab velocity.

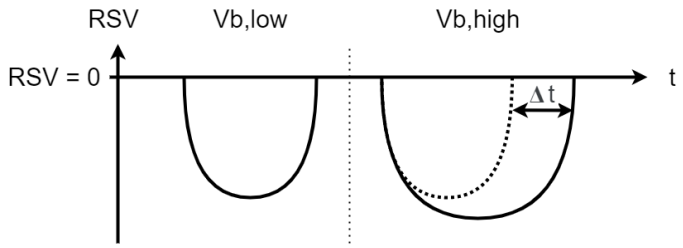

Figure 5.7: Comparison of the Relative Sliding Velocities (RSV) over time during one slip cycle for a low and high slab velocity (vb). The dashed line on the right illustrates the RSV cycle of the low slab velocity to show the difference between the RSV for a low and high slab velocity.

5.3 Influence of Parameters On Kinetic Friction Coefficient

In this Section the kinetic friction coefficients that results from the modelling is analysed. In Section 4.4 it was already explained how the friction force was modelled. The input for this modelling was the friction coefficients derived from experimental data (Nuus, 2018), and taking 25% from those values as during the validation it was found that the friction coefficients were overestimated by a factor of 4. The numerical model uses these coefficients as an initial guess to calculate the friction forces which are used as input in the equations of motions. Throughout the run the forces are updated, and so are the corresponding friction coefficients. This means that the input friction coefficients are not equal to the output friction coefficients. Again, the coefficients are determined as in Equation 5.2:

$$F_{friction} = m * g * \mu_{friction} \tag{5.2}$$

Ultimately, this leads to new friction coefficients in the steady-state regime. Those are presented in this Section. As the kinetic friction force was modelled with a dependency of the relative sliding velocity only the kinetic friction forces and corresponding coefficients are examined, not the static component. The goal of the analysis in this Section is to gain insight into the effects of the involved parameters (mass, stiffness and slab velocity) on the kinetic friction coefficient. The results of the kinetic friction coefficients are presented in Figures 5.8a-5.8d.

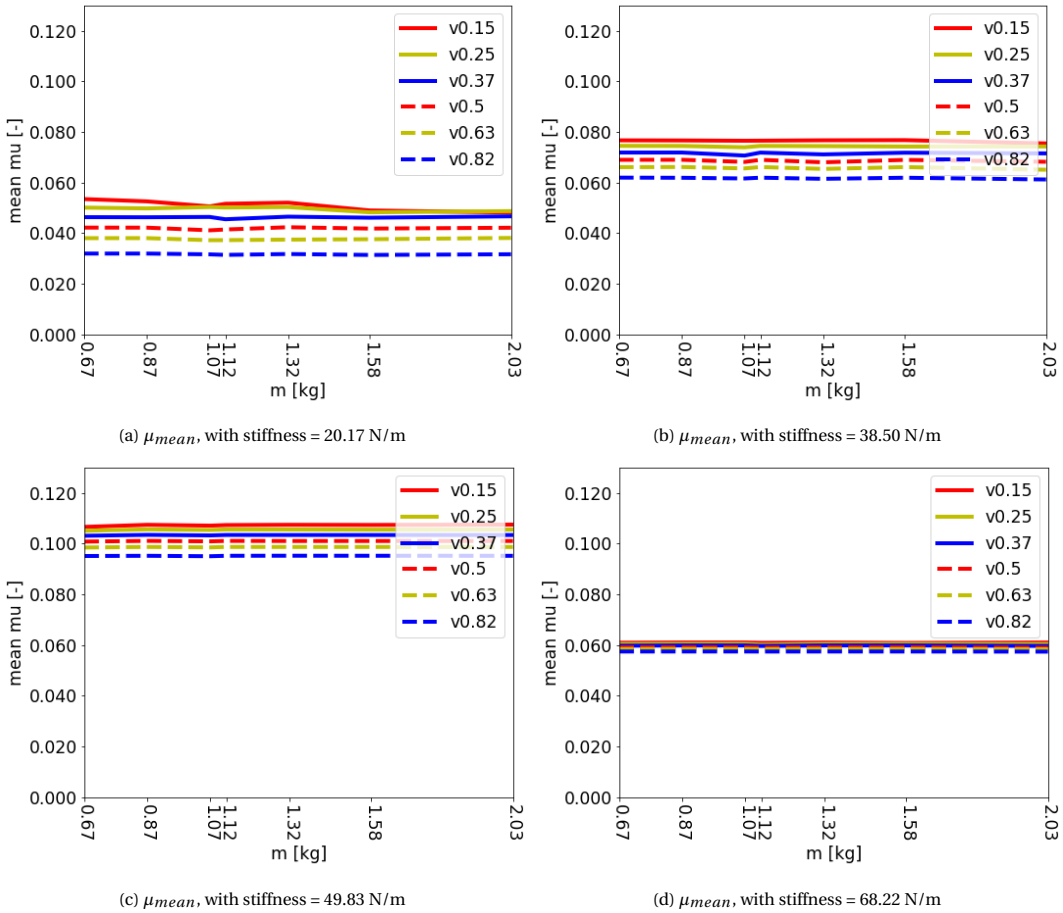

(a) μ_{mean}, with stiffness = 20.17 N/m

(b) μ_{mean}, with stiffness = 38.50 N/m

(c) μ_{mean}, with stiffness = 49.83 N/m

(d) μ_{mean}, with stiffness = 68.22 N/m

Figure 5.8: (a, b, c, d): mean kinetic friction coefficients for different stiffnesses. the label 'v0.15' corresponds to the dataset with 0.15 m/s slab velocity in x-direction, etc. The range of the y-axes in all Figures are kept the same in order to easier compare the results per stiffness with each other. Hence, the graphs may look slim.

The horizontal lines in Figures 5.8a- 5.8d show that a similar kinetic friction coefficient is found per mass. The horizontal lines also indicate that Coulomb's Law of Friction is a good approximation for determining the kinetic friction forces.

In Figure 5.8a it becomes apparent that the kinetic friction coefficient decreases with increasing slab velocity. This is plausible as it was earlier assumed, based on experimental data and findings by Nuus (2018), that there exists an inverse linear relationship between the slab velocity and the kinetic friction coefficient. Figure 5.9 shows this relationship, and was already explained in Subsection 4.4.2.

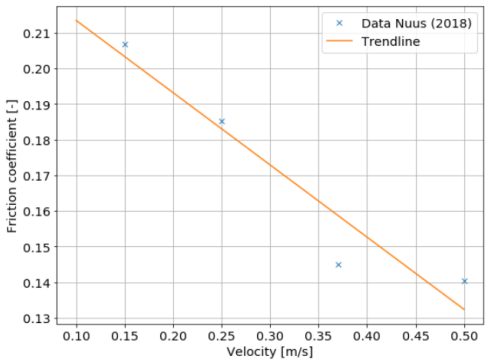

Figure 5.9: Inverse linear relation between the slab velocity and the kinetic friction coefficient. Data from Nuus (2018)

However, with increasing stiffness the variation of kinetic friction coefficients per different slab velocity decreases. This can be observed when comparing the Figures 5.8a-5.8d. Which means that kinetic friction coefficients converges to a single value the stiffer the spring are. This leads to the hypothesis that if the stiffness would be large enough, a single kinetic friction coefficient could be found regardless of slab velocity.

This is tested doubling the highest stiffness of the current set of parameters. The model is then run again for all slab velocities and mass, and the results are shown in 5.10b. To enable easier comparison, the results with stiffness 68.22 N/m are also shown, in Figure 5.10a.

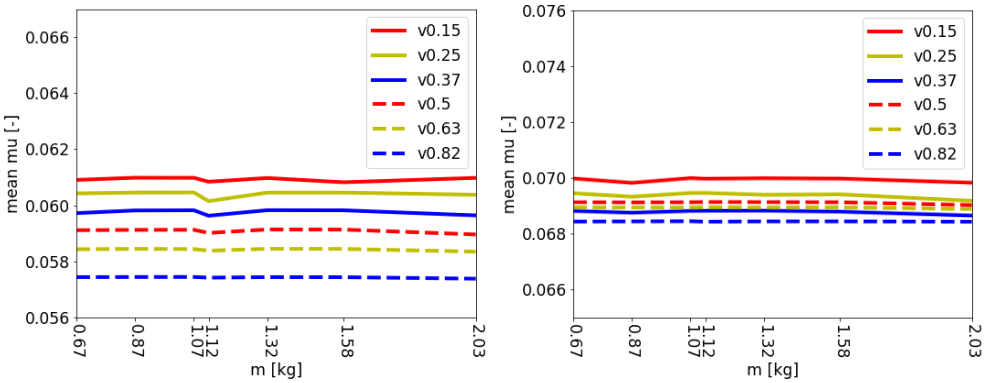

(a) μ_{mean}, with stiffness = 68.22 N/m

(b) μ_{mean}, with stiffness = 136.44 N/m

Figure 5.10: (a, b): The Δ_y of the y-axes in both Figures are kept the same in order to easier compare the results per stiffness with each other. Hence, the graphs may look slim.

Doubling the stiffness to 136.44 N/m leads to more harmonisation of the kinetic friction coefficient. So, the slab velocity has less and less influence on the friction coefficient the stiffer the system becomes. Ultimately, if the stiffness would be high enough it is believed that a single kinetic friction coefficient is reached. With the given results this hypothesis cannot be verified 100%. Nevertheless, the decrease in variation of the coefficients with slab velocities can be explained. If the stiffness is high enough the mass would switch to slip mode almost immediately after leaving it's equilibrium position, and because of the high stiffness the mass would be kept firmly in place. This will lead to the case where the mass is in constant slip mode around it's equilibrium position. The slab velocities considered in this thesis, in the range between 0.15 m/s and 0.82 m/s, have no influence on this. Hence, the independence of the slab velocities is logical.

Comparing all five systems with different stiffnesses it shows that although the influence of the slab velocity decreases with increasing stiffness, this does not lead to an asymptote for the friction coefficient. So, there exists no clear relation between the stiffness and the kinetic friction coefficient.

5.4 Influence of ratio kinetic to static friction on displacements/forces

In this Section an analysis is carried out in which the ratio of kinetic friction coefficient to static friction coefficient is varied. This ratio is shown in Equation 5.3:

$$Ratio = \frac{\mu_{kinetic}}{\mu_{static}} \tag{5.3}$$

Initially, and as outcome of the validation, this ratio was 0.77. In this analysis that ratio serves as the initial case with which the results of the analysis is compared. In this analysis the ratio of kinetic to static friction coefficient is first set at 0.5, so a lower kinetic friction compared to the initial case. Secondly, this ratio is set at 1.0, so a higher kinetic friction compared to the initial case. The upper case ratio is intentionally set at 1.0 as the kinetic friction will not be higher compared to the static friction. The ratios of 0.5 and 1.0 could also have been achieved by either decreasing or increasing the static friction instead of the kinetic friction coefficient. It proved to be more convenient to change the kinetic friction coefficient without changing the model too much. That is why the kinetic friction coefficient was changed to achieve the desired ratios, and not the static friction coefficient. The goal of this analysis is to gain insight into how this ratio affects the behaviour of the mass with respect to experimental data, but also with respect to the initial case with a ratio of 0.77. For this analysis only the steady-state regime is examined, and the set of parameters used are a mass of 0.67 kg, a stiffness of 20.17 N/m and a slab velocity of 0.15 m/s. In Figures 5.11a-5.11c the x-displacements of the analysis are shown. In contrast to previous analyses, this analysis focuses on the behaviour of a single run of the model compared to the experimental data (Nuus, 2018). When focusing on single runs the differences as a consequence to different kinetic to static friction ratios are easier observed compared to focusing on mean x-displacements or mean friction forces.

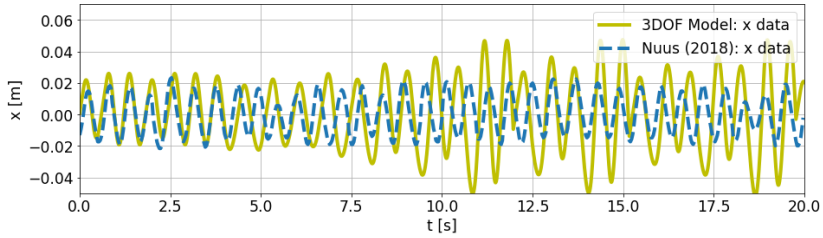

(a) $\frac{\mu_{kinetic}}{\mu_{static}} = 0.5$, counting 30 oscillations

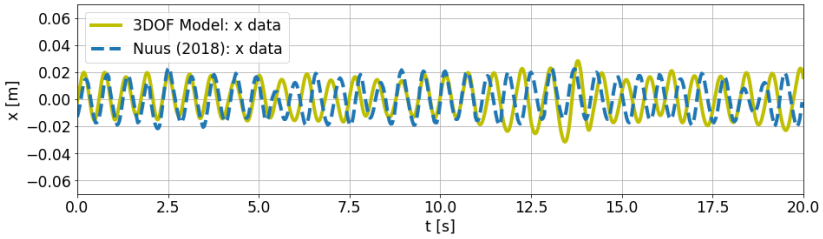

(b) $\frac{\mu_{kinetic}}{\mu_{static}} = 0.77$, initial case, counting 31 oscillations

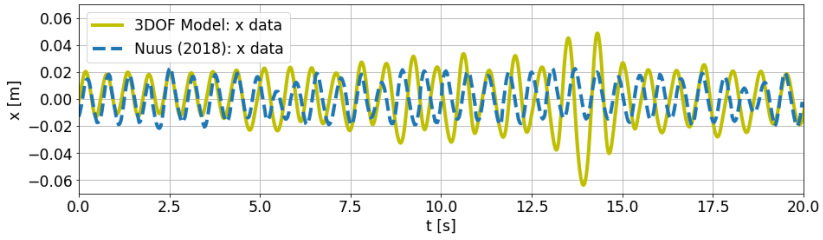

(c) $\frac{\mu_{kinetic}}{\mu_{static}} = 1.0$, counting 29 oscillations

Figure 5.11: (a,b,c): Comparing the x-displacements of both the 3DOF model and the experimental data with different kinetic to static friction coefficient ratios. Experimental data counts 34 oscillations

During the validation of the model, the start of the steady-state regime was set to start after 10 cycles of

stick and slip phases. In the results presented in this Section this means that the start of the steady-state regimes is around t = 0 s. When comparing the results shown in Figures 5.11a-5.11c it can be concluded that in the beginning, first 5 seconds, all three cases show similar behaviour in terms of amplitude and period, and they all match with the experimental data. After that the cases with deviating ratios 0.5 and 1.0 start to show larger amplitudes and longer periods compared to the initial case and the experimental data. This suggests that the two deviating cases are not yet in steady-state regime. The behaviour of the case with a ratio of 0.5 starts the steady-state regime at 7.5 s as the x-displacements do show a repetition, whereas for the case with a ratio of 1.0 it is unclear when the steady-state regime starts. Both deviating cases count one or two oscillations less compared to the case with the initial ratio of 0.77. This shows that the deviating cases have longer periods. The large amplitudes in the case with a ratio of 0.5 can be explained by the lower kinetic friction coefficient. During slip The lower kinetic friction causes less resistance. This means that the spring forces are relatively higher compared to the kinetic friction force. This difference in forces causes the mass to be pushed away from the springs faster compared to the initial with a ratio of 0.77 (Figure 5.11b). The higher relative sliding velocity causes larger amplitudes in x-direction, and it compensates the slower movement caused by the lower kinetic friction. That is why the lower kinetic friction does not result in slower slip behaviour, and almost no change in the period of the oscillation. There was no explanation found for the deviating amplitudes and periods in Figure 5.11c with ratio 1.0. Therefor, the high amplitudes around t = 13 s are attributed to the randomness in modelling the friction forces.

In Figures 5.12a-5.12c the friction forces of the analysis are shown. As Nuus (2018) does not provide data that shows the friction force of a single run, the comparison with the experimental is not carried out for the friction forces. Instead, the focus is put on comparing the three different kinetic to static friction coefficient ratios.

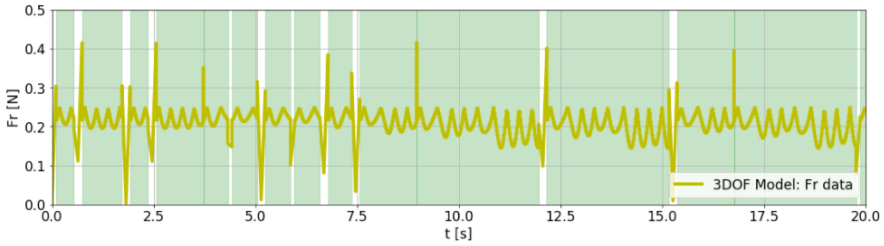

(a) $\frac{\mu_{kinetic}}{\mu_{static}} = 0.5$

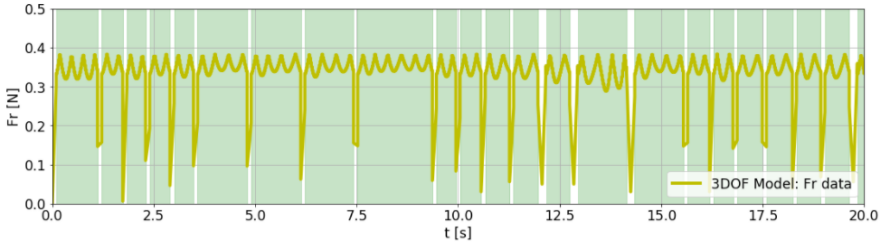

(b) $\frac{\mu_{kinetic}}{\mu_{static}} = 0.77$, initial case

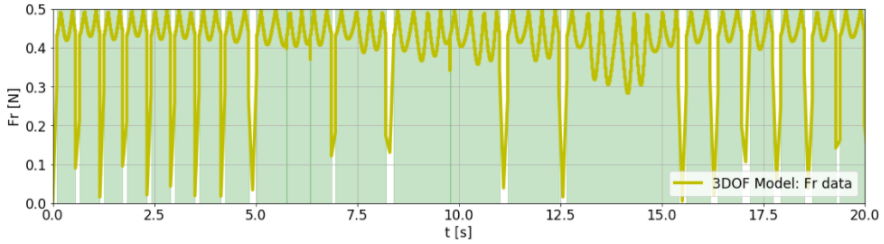

(c) $\frac{\mu_{kinetic}}{\mu_{static}} = 1.0$

Figure 5.12: (a,b,c): Analysing the friction forces of the 3DOF model with different kinetic to static friction coefficients ratios. The green background shows when the mass is in slip mode

From Figures 5.12a-5.12c it is observed that the kinetic friction forces increase with increasing ratio, which is exactly what should happen when the ratio of kinetic to static friction is increased. During slip mode the kinetic friction force makes a half oscillatory movement. The difference between the maximum and minimum kinetic friction force per such a half oscillatory movement also increases with increasing friction ratio. This is attributed to the relative sliding velocity, as the kinetic friction force is modelled with a dependency on the relative sliding velocity. Apparently, with higher kinetic friction, the effect of the relative sliding velocity is magnified.

With a kinetic to static friction coefficient ratio of 0.5 there is less kinetic friction occurring comapred to the initial case. The lower kinetic friction prolongs the slip times, and decreases the amount of stick periods within the same time period (less white bars in Figure 5.12a). The longer the slip time the more time the effects of the imbalance in y-direction are felt by the mass, and the heavier the oscillations in x-direction compared to the case with a ratio of 0.77. Also, with a ratio 0f 0.5 the difference between the static and kinetic friction is largest. This can be seen by the peaks in the white bars in Figure 5.12a, here the friction force shows jumps when the mass switches from stick (white background) to slip (green background). Another consequence of the prolonged slip times is that the model with a ratio of 0.5 behaves slower compared to the model with a ratio of 0.77. The peaks observed in Figure 5.12a during stick should also be visible in Figure 5.12b as the static friction is higher compared to the kinetic friction too. This is however, not visible, and the reason for this lies in the numerical modelling of this system. The higher static friction force is in fact there, but not visible because of the scale of the x-axis. The same can be said about the unsmooth transition

from stick mode to slip mode in Figure 5.12c where the static friction coefficient is equal to the kinetic friction coefficient. This leads to no jump in the friction force when switching from stick to slip, although Figure 5.12c shows minor jumps.

Chapter 6

Discussion

In this Chapter the best test set-up from Chapter 3 and the three degree of freedom (3DOF) numerical model from Chapter 4 are being discussed. Section 6.1 discussed the test set-up and Section 6.2 discusses the 3DOF numerical Model. As the main focus of this thesis shifted towards the modelling of the ice-structure interaction the research conducted into this area is more thorough compared to the research into the test set-ups. That is also the reason why the discussion about these two topics are not equally thorough. The discussion of the 3DOF numerical model is more in depths compared to the discussion of the test set-up.

6.1 Discussion Regarding Best Test Set-up

In this Section the test set-up is being discussed. The test set-up that was deemed best for the experiment is again illustrated below in Figures 6.1a & 6.1b.

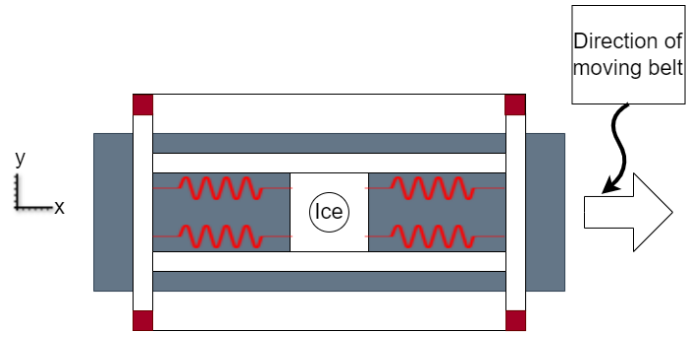

(a) Construction layout top view in *xy*-frame

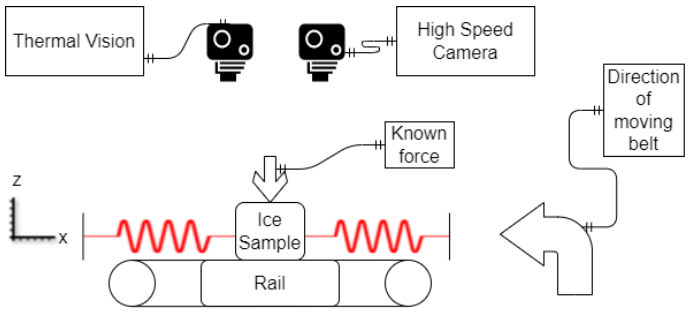

(b) Construction layout side view in *xz*-frame

Figure 6.1: (a,b): Illustrations of the test set-up as already presented in Section 3.3

The proposed set-up does not use real construction materials such as concrete or steel. The use of such materials would not enable the test set-up to exert 1D forcing on the ice sample. Meaning, that with the use of construction materials the experiment will always be a 2D experiment, and thus 2D behaviour of the ice will

always be found. It is noteworthy to say that when looking for experimental test set-ups in literature, no test set-ups were found that combined construction materials and 1D ice-structure interaction. There was always an element of 2D behaviour found. That is why the possible test set-ups with 1D behaviour were always ideas developed by the author.

The use of equipment at a temperature below zero causes uncertainty as to whether or not the equipment will function properly. During the search for proper equipment it was never explicitly stated, apart from the thermal imaging camera, that the equipment could be used at temperatures below zero. Manufacturers could never say if the equipment could withstand temperatures below 0°C, as it was not made to function under such circumstances. The thermal imaging camera that was mentioned in Subsection 3.3.3 was purchased and tested, and it was found that the bolometer matrix of 320 x 240 pixels and the thermal sensitivity of 70 mK was not adequate enough. The camera could measure 1°C difference, but not 0.01°C difference, which was the resolution that was wanted for.

6.2 Discussion Regarding 3DOF Numerical Model

In this Section the 3DOF numerical model is being discussed. As explained in Chapter 4, and again in Chapter 5, the 3DOF numerical model was set up with equations of motion that were derived from physical experiment conducted by Nuus (2018), of which the illustrations are given in Figures 6.2a & 6.2b. These illustrations are shown again for the readability of this thesis.

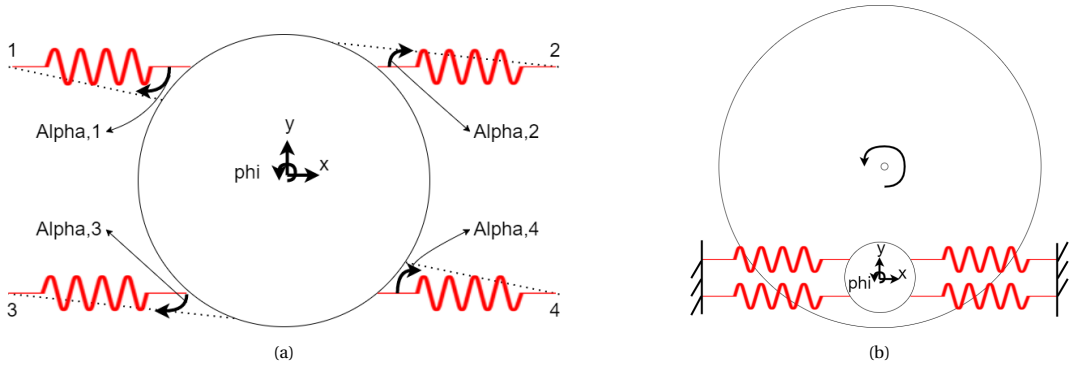

Figure 6.2: (a): Orientation of Axes and degrees of freedom of the ice sample. Full stripes indicate the springs in original position, and the dashed lines indicate the springs after rotation of the ice mass, (b): Top view of the ice sample (smaller circle) on top of the rotating slab (larger circle)

When modelling the friction force it was assumed that the friction force could be modelled using Coulomb's Law of Friction. This is also known as dry friction. It is known that during the conducted experiment by Nuus (2018) the system has a start-up period during which the rotating concrete slab is speeded up until it has the desired rotating velocity. After one rotation the sliding interface is reused again, meaning that the ice sample is slid over the same surface each rotation. This causes the interface to be wet, and this has been confirmed by Nuus (2018). This is on top of the lubricating layer that already exists at the surrounding temperature (Kietzig et al., 2010). Both effects are sufficient to say that the assumption of Coulomb Friction is not completely valid, and the circumstances point towards a combination of dry and marginal hydrodynamic friction. These hydrodynamic effects were not modelled. Nevertheless, the data from the 3DOF numerical model show that although these effects were not modelled, the current friction modelling is good enough to describe the 2D behaviour found in the experimental data. That is also why the friction can be approximated by using Coulomb's Law of Friction.

In general, springs are never linear over the entire length. Only in the first couple of centimeters a spring is linear, but beyond that range the spring will exert more force on the mass as a consequence of the nonlinearity in the spring. This can cause the modelled forces exerted by the springs on the mass in ranges beyond roughly a couple of centimeters to be underestimated, which can lead to larger excitations on occasion. During some model runs, on occasions, the excitations of the model exceeded the maximum occurring excitation of the experimental data (Nuus, 2018). An example of this is found in Figure 6.3. In this Figure around t = 13.5 s the excitation exceeds the maximum occurring amplitude of the experimental data.

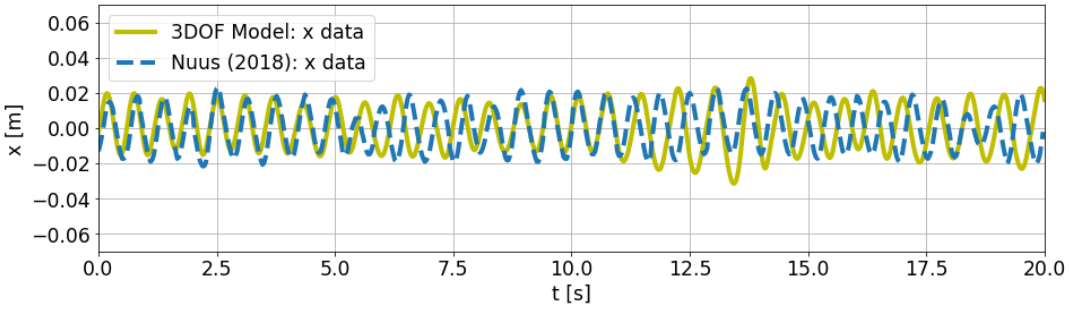

Figure 6.3: Comparison between output 3DOF numerical model and experimental data (Nuus, 2018). Parameters used: mass = 0.67 kg, stiffness = 20.17 N/m, slab velocity = 0.15 m/s

Furthermore, the length of springs was not provided by Nuus (2018), and was derived based on pictures provided by Nuus (2018), and assumed to be 20 cm. Also the angles β_i were assumed based on these pictures at ± 20°from the horizontal line. So β_1 = 160°, β_2 = 20°, β_3 = 200°, and β_4 = 340°. Both of these estimations cause uncertainty in the 3DOF numerical model. If the assumption of the lengths and angles are a little bit off, they are deemed to be of not enough influence to have a significant effect on the data of the 3DOF numerical model. If they were, the 3DOF numerical model would not have matched well with the experimental data. That, or the estimation of the angles and spring lengths was accurate.

As a consequence of the translations and rotation of the mass the position where the spring is attached to the mass moves along with this motion. This puts the spring under an angle with respect to it's original position. When incorporating this angle in defining the contribution of the springs to the equations of motions this leads to a nonlinearity. To be able to linearise this a Taylor polynomial was used. This was done using the Taylor polynomial expansion as described in Equation 6.1:

$$\epsilon_i = \sqrt{\Delta x_i|\Delta x_i| + \Delta y_i|\Delta y_i|} = \sqrt{1 + \frac{\Delta y_i|\Delta y_i|}{\Delta x_i|\Delta x_i|}} = 1 + \frac{1}{2}\frac{\Delta y_i|\Delta y_i|}{\Delta x_i|\Delta x_i|} + O(2) \tag{6.1}$$

Where the subscript i stands for the spring and it's corresponding position on the circumference of the mass. The positions are labelled 1-4, and can be seen in Figure 6.2a.

In determining the friction force exerted by the rotating slab on the mass the relative sliding velocity was taken into account. However, this was only done in x-direction. This means that only a friction force in x-direction was modelled, but not in y-direction. It was stated in Section 4.4 that the friction force in y-direction was of insignificant value compared to the friction force in x-direction. However, The mean displacements in y-direction found in this thesis remain close to the equilibrium position and is almost zero (see Figure 6.4a), whereas the experimental data show a mean excitation of around 0.01 m (see Figure 6.4b). This mean excitation is not found in the model. A reason for this could be that the y-component of the friction force was not modelled in the 3DOF numerical model. That y-component is present in the experiment as the rotation of the concrete slab creates a loading in both radial (y-) and transverse (x-) direction.

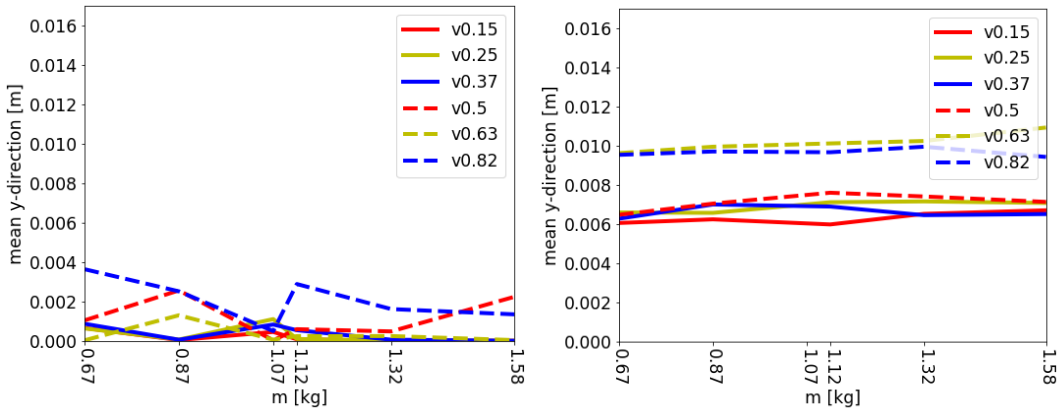

(a) 3DOF model data: y_{mean} with stiffness = 38.50 N/m

(b) Experimental data Nuus (2018): y_{mean} with stiffness = 38.50 N/m

Figure 6.4: (a,b):

A second assumption regarding the relative sliding velocity in x-direction was made. The model switches from stick to slip and back to slip again. To switch from slip mode to stick mode the relative sliding velocity needs to be zero, because that would mean that the mass would have the same velocity as the belt. For this threshold only the relative sliding velocity in x-direction was used, but not the relative sliding velocity in y-direction or the angular relative sliding velocity. It was believed during the modelling that using only the relative sliding velocity in x-direction was good enough to create a model that matches well with the experimental data, and it does. It would be an improvement if also the relative sliding velocity in y-direction and the angular relative sliding velocity were taken into account.

Chapter 7

Conclusion & Recommendations

In this Chapter the conclusions of this thesis are presented in Section 7.1 and recommendations are presented in 7.1b. At first the thesis focused on realising a test set-up and conducting experiments, called Track #1. Halfway through the focus shifted towards modelling a stick-slip model of ice-structure interaction based on data from an experiment that had already been carried out, called Track #2. More comments about the comparison between the two tracks can be found later on in this Chapter. Because with Track #2 the focus shifted towards modelling the majority of the conclusions and recommendations are focused on the outcomes of the modelling track of this thesis. Only briefly attention paid is to Track #1 the test set-up analysis from Chapter 3. The parameters involved in this thesis that is focused on are: the mass of the ice sample, the velocity of the material over which the ice is slid, and the stiffness of the springs that are used to keep the ice sample in place while still allowing translation and rotation of the ice sample. The use of springs and the movements of the ice enable the determination of the friction forces.

7.1 Conclusions

The best test set-up that came out of the analysis in Chapter 3 is a test set-up that uses a conveyor belt of sandpaper. On this conveyor belt an ice sample is placed, and four springs are attached to the back and front of the sample to ensure that the sample can move, but stays relatively in the same position. An illustration of the full test set-up and a picture of the proposed conveyor belt system are shown in Figures 7.1a & 7.1b. The full test set-up as shown in Figure 7.1a is deemed best for the experiments. All possible test set-up were evaluated based on the following four criteria: whether or not concrete or steel can be used as sliding interface during experiments, whether or not testing materials can be changed easily to alter parameters involved in the friction process. The machine shown in Figure 7.1b is to be used in the test set-up. The sandpaper conveyor belt is the brown element that can be seen in the top of the figure, the motor of the conveyor belt consists of the black objects on the left, and the grey surrounding table can be used to place equipment on.

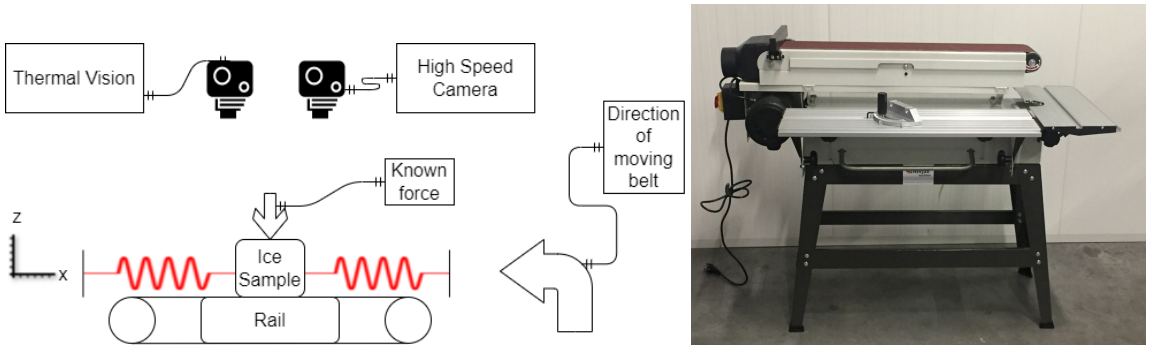

(a) Illustration of the final test set-up

(b) Actual Belt Sanding Machine (Heejan, 2021)

Figure 7.1: (a,b): Layout of the final test set-up

As explained in Section 3.5 the realisation was farmed out to an outside construction company, and the

realisation on their part took too long. Initially, the aim was to carry out 1D experiments with this set-up varying the parameters as explained in Chapter 3.4. This would have given an overview of how different parameters influence the ice-structure friction process. The same parameters were chosen as previous research that had used a 2D experiment set-up (Nuus, 2018). If the realisation of the 1D test set-up as shown in Figures 7.1a & 7.1b would have been successful and 1D experiments would have been carried out, it would have been possible to compare the output of the 1D experiment with the previous research of a 2D experiment. It is unclear to what extent this comparison would have been possible because the 1D experiment proposed in this thesis would have used sandpaper as a substitute for the concrete or steel, where the 2D experiment conducted by Nuus (2018). Nuus (2018) set-up a one degree of freedom (1DOF) model to try and describe the 2D behaviour found in her experiment. One of her recommendations was to set up a three degree of freedom (3DOF) model to describe the behaviour found in her experimental data. Because the realisation of the proposed 1D test set-up in this thesis took too long, it was decided to follow up on that recommendation, and a 3DOF model was created.

This 3DOF numerical model was set up in Chapter 4. A schematic overview from which the 3DOF numerical model is derived, is shown in Figures 7.2a & 7.2b. Four different approaches were used to determine the contribution of the springs to the Equations of Motions. It was found that the best way to do this was to update the position of the spring with respect to it's original position every timestep during modelling. Secondly, two different approaches were used to determine the friction forces acting on the ice-structure interface. Both approaches used the kinetic and static friction coefficients determined by Nuus (2018) as a starting point to determine the friction forces. It was found that the friction force was best modelled when determining the friction force with a dependency on both the mass of the ice sample, and the sliding velocity of the mass with respect to the sliding surface. The main conclusions of Track #2 are that the created 3DOF numerical model works, that it is verified, validated, and that it matches with the experimental data of Nuus (2018). From the validation of the 3DOF numerical model it was concluded that the initial friction coefficients determined by Nuus (2018) overestimated the friction coefficients by a factor of 4. Meaning, that when the created 3DOF model uses friction coefficients that are 25% of the determined friction coefficients of Nuus (2018), the output of the 3DOF model matches with the experimental data of Nuus (2018). For example: Nuus (2018) found μ_{static} = 0.28 whereas this thesis finds μ_{static} = 0.065, for a the same set of parameters. Again, all the parameters used in this thesis are the same as used by Nuus (2018). It is therefor also concluded that a 1DOF model is not able to accurately describe the 2D behaviour found in the experimental data.

The sensitivity analysis carried out in Chapter 5 shows a linear relationship between increasing friction and increasing mass, which is in accordance with Coulomb´s Law of Friction, and that this linear relationship becomes less steep with increasing spring stiffness. Furthermore, when the spring stiffness is relatively low the slab velocity has considerably impact on the mean x-displacement. The cause of this has been explained in 5.1, 5.2 and 5.3.

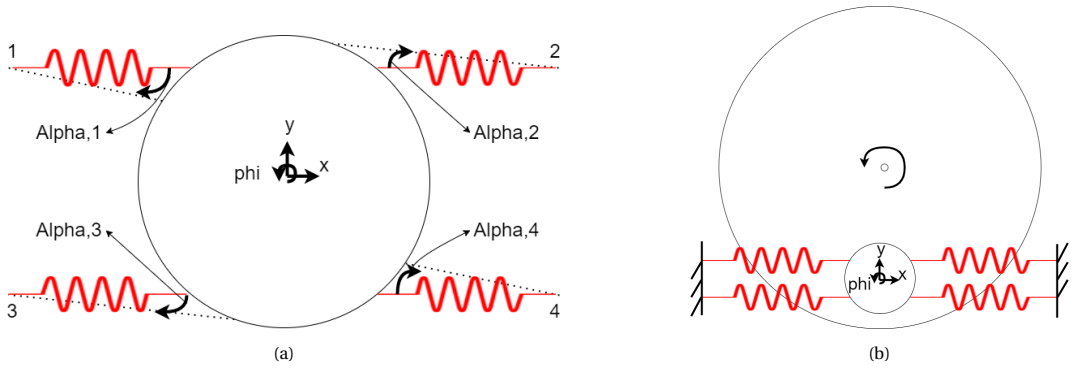

Figure 7.2: (a): Orientation of Axes and degrees of freedom of the ice sample. Full stripes indicate the springs in original position, and the dashed lines indicate the springs after rotation of the ice mass, (b): Top view of the ice sample (smaller circle) on top of the rotating slab (larger circle)

Regarding the 1D test set-up, the 3DOF numerical model shows that such a model is capable of describing the 2D behaviour that can be found when exerting 2D loading on an ice sample. This puts the earlier discussion of the 1D test set-up in a new perspective, because although a 1D test set-up would be beneficial for getting better insight into the ice-structure friction process regarding 1D loading, it is now concluded that a 1D test set-up is not necessary to conduct the research.

7.2 Recommendations

The following list lists the recommendations of this thesis:

- With the benefit of hindsight it is recommended to focus on carrying out 2D experiments, rather than to focus on 1D experiments. 2D experiments allow the use of concrete and steel, and this research showed that a numerical model is capable of describing the 2D behaviour found in that experiment. In this research a main parameter of influence was left out: the temperature. It is recommended to focus on extending this research by using the same set of parameters in this thesis, but varying the temperature. When doing this it may be interesting to try and vary both the surrounding temperature and the ice sample temperature as these are linked, but they are not necessarily the same. For this research it is recommended to use an apparatus such as the one used by Nuus (2018), but with a smaller radius of the rotating concrete slab. As the 2D effect can now be modelled it does not matter anymore to what extent this 2D effect is present in the behaviour of the ice sample. Therefor the test set-up does not have to be as large as the test set-up Nuus (2018) used. This would allow the test to be carried out in the relatively small cold room at TU Delft's faculty of Civil Engineering and Geosciences.

- In the numerical 3DOF model created in this thesis the stick and slip mode have been modelled linearly, but independent from one another. This means that the 3DOF model in itself is not linear, but that the two modes are linear and the model switches between the two modes. In the slip mode the forces exerted on the mass are linearised, which enabled the use of linear modelling techniques in Python. It would be an improvement if the forces can be modelled nonlinear, and therefor the slip mode can be modelled nonlinear. As discussed in Section 6.2 a truncation error of the second order was made. If modelled nonlinear, this truncation error would be taken out of the equation.

- In the numerical 3DOF model the 2D component of the friction force was not taken into account when modelling the slip behaviour of the mass. This 2D component is the force in y-direction. It would be an improvement if this 2D force component was modelled as well. Perhaps this force could lead to the mean offset in y-direction that was found in the experimental data provided by Nuus (2018), see Figure 7.3. Also the relative sliding velocity in y-direction and the angular relative sliding velocity can be taken into account to improve the 3DOF numerical model.

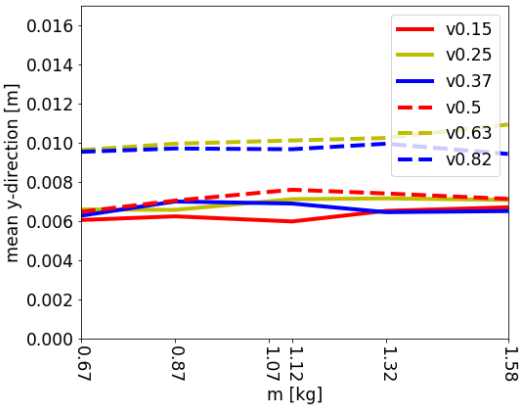

Figure 7.3: Experimental data Nuus (2018): y_{mean} with stiffness = 38.50 N/m

- During the process of realising a test set-up it was found that the construction process is time-consuming. It is therefor advised to think carefully before contracting a party (either TU Delft' DEMO[1] or outside construction company) to deliver the test set-up. It could be wise to built an initial set-up by oneself, which may be of lesser quality, but still provide meaningful insight into the process of 1D ice-structure friction.

[1] Dienst Elektronische & Mechanische Ondersteuning: TU Delft's factory where all experimental test set-ups are being built

References

Akkok, M., Ettles, C. M. M., & Calabrese, S. J. (1987, 07). Parameters Affecting the Kinetic Friction of Ice. *Journal of Tribology*, *109*(3), 560-560. Retrieved from https://doi.org/10.1115/1.3261504 doi: 10.1115/1.3261504

Albracht, F., Reichel, S., Wlnkler, V., & Kern, H. (2004). Untersuchung von Einflussfaktoren auf das tribologische Verhalten von Werkstoffen gegen Eis. *Materialwissenschaft und Werkstofftechnik*, *35*(10-11), 620–625. doi: 10.1002/mawe.200400822

Bäurle, L., Szabó, D., Fauve, M., Rhyner, H., & Spencer, N. D. (2006). Sliding friction of polyethylene on ice: Tribometer measurements. *Tribology Letters*, *24*(1), 77-84. doi: 10.1007/s11249-006-9147-z

Bowden, F., & Hughes, T. (1939). The mechanism of sliding on ice and snow. *Proceedings of the Royal Society of London. Series A. Mathematical and Physical Sciences*, *172*(949), 280–298. doi: 10.1098/rspa.1939.0104

Calabrese, S., Buxtion, R., & Marsh, G. (1980). Frictional characteristics of materials sliding against ice. *American Society of Lubricating Engineers*, *36*(5), 283–289.

De Koning, J. J., Houdijk, H., De Groot, G., & Bobbert, M. F. (2000). From biomechanical theory to application in top sports: The Klapskate story. *Journal of Biomechanics*, *33*(10), 1225–1229. doi: 10.1016/S0021-9290(00)00063-4

Dekking, K. C. L. H. P. M. L. E., F. M. M. (2005). *A modern introduction to probability and statistics: Understanding why and how*. Springer.

Dowson, D. (1998). *History of tribology*. Professional engineering Publishing for the institution of mechanical engineers.

Ducret, S., Zahouani, H., Midol, A., Lanteri, P., & Mathia, T. (2005). Friction and abrasive wear of uhwmpe sliding on ice. , *258*, 26–31.

Dynamics and control. (n.d.). Retrieved from https://apmonitor.com/pdc/index.php/Main/StateSpaceModel

Electronic, C. (2021). *Seek Thermal ShotPRO Warmtebeeldcamera -40 tot +330 Â°C 320 x 240 Pixel 9 Hz WiFi | Conrad.nl*. Retrieved from https://www.conrad.nl/p/seek-thermal-shotpro-warmtebeeldcamera-40-tot-330-c-320-x-240-pixel-9-hz-wifi-1761227

Evans, D. C. B., Nye, J. F., & Cheeseman, K. J. (1976). The Kinetic Friction of Ice. *Proceedings of the Royal Society of London. Series A, Mathematical and Physical Sciences ,*, *324*(1651), 493–512.

Feng, D., xue Shen, M., dong Peng, X., & kai Meng, X. (2017, jan). Surface Roughness Effect on the Friction and Wear Behaviour of Acrylonitrile–Butadiene Rubber (NBR) Under Oil Lubrication. *Tribology Letters*, *65*(1), 1–14. Retrieved from https://link-springer-com.tudelft.idm.oclc.org/article/10.1007/s11249-016-0793-5 doi: 10.1007/s11249-016-0793-5

Fiorio, B., Meyssonnier, J., & Boulon, M. (1997). Experimental study of the friction of ice over concrete at the centimetre scale. *Proceedings of the International Offshore and Polar Engineering Conference*, *2*, 466–472.

Gamma NL. (2021). *GAMMA | Piranha schuurband K60 533x75 mm 3 stuks X33186 kopen? | schuurpapier*. Retrieved from https://www.gamma.nl/assortiment/piranha-schuurband-k60-533x75-mm-3-stuks-x33186/p/B197859

Hayes, W. (2017). *Crc handbook of chemistry and physics: a ready-reference book of chemical and physical data.* (97th ed.). CRC Press.

Heejan. (2021, 05). *Bandschuurmachine 2010 x 152 mm.* Retrieved from https://www.heejan.nl/machines/bandschuurmachine/

Itoh, Y., Yoshida, A., Tsuchiya, M., Katoh, K., Sasaki, K., & Saeki, H. (1988). An experimental study on abrasion of concrete due to sea ice. In *Proceedings of the annual offshore technology conference* (Vol. 1988-May, pp. 61–68).

Jones, S. J., Kitagawa, H., Izumiyama, K., & Shimoda, H. (1994). Friction of melting ice. *Annals of Glaciology*, *19*, 7–12. doi: 10.3189/1994AoG19-1-7-12

Kietzig, A. M., Hatzikiriakos, S. G., & Englezos, P. (2010). Physics of ice friction. *Journal of Applied Physics*, *107*(8). doi: 10.1063/1.3340792

Leine, R., Van Campen, D., De Kraker, A., & Van Den Steen, L. (1998). Stick-slip vibrations induced by alternate friction models.

Lishman, B., Sammonds, P., & Feltham, D. (2011). A rate and state friction law for saline ice. *Journal of Geophysical Research: Oceans*, *116*(C5). Retrieved from https://agupubs.onlinelibrary.wiley.com/doi/abs/10.1029/2010JC006334 doi: https://doi.org/10.1029/2010JC006334

Marghitu, D. B. (2001). *6. theory of vibration.* Elsevier. Retrieved from https://app.knovel.com/hotlink/khtml/id:kt00C5H7P3/mechanical-engineers/theory-of-vibration

Marmo, B. A., Blackford, J. R., & Jeffree, C. E. (2005). Ice friction, wear features and their dependence on sliding velocity and temperature. *Journal of Glaciology*, *51*(174), 391–398. doi: 10.3189/172756505781829304

Møen, E., Høiseth, K. V., Leira, B., & Høyland, K. V. (2015, feb). Experimental study of concrete abrasion due to ice friction - Part I: Set-up, ice abrasion vs. material properties and exposure conditions. *Cold Regions Science and Technology*, *110*, 183–201. doi: 10.1016/j.coldregions.2014.09.008

Morin, D. (2007). The Lagrangian Method.

Nakazawa, N. (1986). The Coefficient of Friction Between Sea Ice and Various Materials Used in Offshore Structures. *Journal of Energy Resources Technology*. Retrieved from https://www.researchgate.net/publication/236399832 doi: 10.4043/4689-MS

Nuus, N. (2018). Stick-slip behavior of ice interacting with concrete surfaces.

Oksanen, P., & Keinonen, J. (1982). The mechanism of friction of ice. *Wear*, *78*(3), 315-324. Retrieved from https://www.sciencedirect.com/science/article/pii/0043164882902423 doi: https://doi.org/10.1016/0043-1648(82)90242-3

Persson, B. N. (2015). Ice friction: Role of non-uniform frictional heating and ice premelting. *Journal of Chemical Physics*, *143*(22). Retrieved from http://dx.doi.org/10.1063/1.4936299 doi: 10.1063/1.4936299

Reynolds, O. (1901). Papers on mechanical and physical subjects.

Schulson, E. M., & Fortt, A. L. (2013, mar). Static strengthening of frictional surfaces of ice. *Acta Materialia*, *61*(5), 1616–1623. doi: 10.1016/J.ACTAMAT.2012.11.038

Thermal Conductivity - selected Materials and Gases. (2003). Retrieved from https://www.engineeringtoolbox.com/thermal-conductivity-d_429.html

World of Physics. (2000, 10). Retrieved from http://www.hk-phy.org/contextual/heat/tep/temch02_e.html

Appendices

Appendix A

Numerical Derivation

A.1 Derivation of Kinetic Energy

$$L = \frac{1}{2}(m\dot{x}^2 + m\dot{y}^2 + J\dot{\phi}^2) - \frac{1}{2}k_i e_i^2 \qquad , \qquad i = 1,2,3,4$$

$$\frac{d}{dt}\left(\frac{\delta L}{\delta \dot{q}_i}\right) = \frac{d}{dt}\left(\frac{\delta K}{\delta \dot{q}_i}\right) \qquad , \qquad \dot{q}_i = \dot{x}, \dot{y}, \dot{\phi}$$

$$\frac{d}{dt}\left(\frac{\delta K}{\delta \dot{x}}\right) = m\ddot{x}$$

$$\frac{d}{dt}\left(\frac{\delta K}{\delta \dot{y}}\right) = m\ddot{y}$$

$$\frac{d}{dt}\left(\frac{\delta K}{\delta \dot{\phi}}\right) = J\ddot{\phi}$$

A.2 Elongation of a single spring

$$e_i = l(t) - l_{original} = \sqrt{(l_{x_i,original} + \Delta x_i)^2 + (l_{y_i,original} + \Delta y_i)^2} - l_{original}$$

$$= \sqrt{(l_{x_i,original}^2 + 2l_{x_i,original}\Delta x_i + \Delta x_i^2) + (l_{y_i,original}^2 + 2l_{y_i,original}\Delta x_i + \Delta y_i^2)} - l_{original}$$

$$= \sqrt{(l_{x_i,original}^2 + l_{y_i,original}^2) * (1 + \frac{2l_{x_i,original}\Delta x_i + 2l_{y_i,original}\Delta y_i}{l_{x_i,original}^2 + l_{y_i,original}^2} + \frac{\Delta x_i^2 + \Delta y_i^2}{l_{x_i,original}^2 + l_{y_i,original}^2})} - l_{original}$$

$$= \sqrt{l_{origianl}^2 * (1 + \frac{2l_{x_i,original}\Delta x_i + 2l_{y_i,original}\Delta y_i}{l_{x_i,original}^2 + l_{y_i,original}^2} + \frac{\Delta x_i^2 + \Delta y_i^2}{l_{x_i,original}^2 + l_{y_i,original}^2})} - l_{original}$$

$$= l_{original}\sqrt{1 + \frac{2l_{x_i,original}\Delta x_i + 2l_{y_i,original}\Delta y_i}{l_{x_i,original}^2 + l_{y_i,original}^2} + \frac{\Delta x_i^2 + \Delta y_i^2}{l_{x_i,original}^2 + l_{y_i,original}^2}} - l_{original}$$

$$\text{Taylor series}\sqrt{1 + x_i} = 1 + \frac{x_i}{2} + O(2)$$

$$e_i = l_{original}\left(1 + \frac{l_{x_i,original}\Delta x_i + l_{y_i,original}\Delta y_i}{l_{x_i,original}^2 + l_{y_i,original}^2} + \frac{1}{2}\frac{\Delta x_i^2 + \Delta y_i^2}{l_{x_i,original}^2 + l_{y_i,original}^2}\right) - l_{original}$$

$$= l_{original}\left(1 + \frac{l_{x_i,original}\Delta x_i + l_{y_i,original}\Delta y_i}{l_{original}} + \frac{1}{2}\frac{\Delta x_i^2 + \Delta y_i^2}{l_{original}}\right) - l_{original}$$

In this thesis the order of derivation is restricted to two for the purpose of execution.

$$e_i = l_{original}\left(1 + \frac{l_{x_i,original}\Delta x_i + l_{y_i,original}\Delta y_i}{l_{original}}\right) - l_{original}$$

$$= \frac{l_{x_i,original}\Delta x_i + l_{y_i,original}\Delta y_i}{l_{original}}$$

$$= \frac{l_{x_i,original}}{l_{original}}\Delta x_i + \frac{l_{y_i,original}}{l_{original}}\Delta y_i$$

$$= cos(\alpha_i)\Delta x_i + sin(\alpha_i)\Delta y_i$$

$$\Delta x_i = x + rcos(\beta_i + \phi) - rcos(\beta_i)$$

$$= x + r(cos(\beta_i)cos(\phi) - sin(\beta_i)sin(\phi)) - rcos(\beta_i)$$

$$\Delta y_i = y + rsin(\beta_i + \phi) - rsin(\beta_i)$$

$$= y + r(sin(\beta_i)cos(\phi) + cos(\beta_i)sin(\phi)) - rsin(\beta_i)$$

Where x, y and ϕ are the respective degrees of freedom as described in Figure A.1. Each spring is attached at a different point on the circumference of the ice sample. α_1 and β_1 refers to point 1, etc. See Figure A.2 for an illustration.

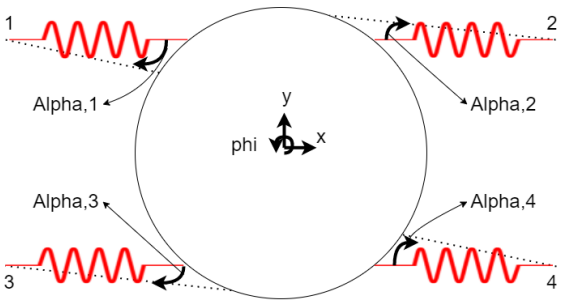

Figure A.1: Orientation of Axes and degrees of freedom

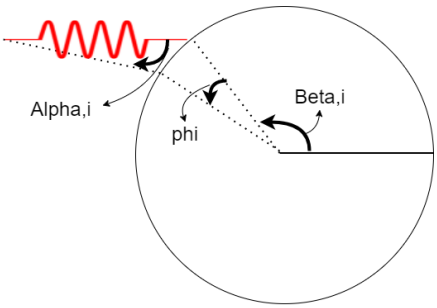

Figure A.2: Orientation of α, β and ϕ

A.3 Derivation of Potential Energy

A.3.1. General Derivation

```
> restart; #THIS IS ALL FOR ONE SPRING
  interface(displayprecision = 2) :
```

```
> e_1 := Δ_x1·cos(α_1) + Δ_y1·sin(α_1);
```

$$e_1 := \Delta_{x1}\cos(\alpha_1) + \Delta_{y1}\sin(\alpha_1) \tag{1}$$

```
> Δ_x1 := x + r·(cos(β_1)·cos(phi) − sin(β_1)·sin(phi) − cos(β_1));
```

$$\Delta_{x1} := x + r\left(\cos(\beta_1)\cos(\phi) - \sin(\beta_1)\sin(\phi) - \cos(\beta_1)\right) \tag{2}$$

```
> Δ_y1 := y + r·(sin(β_1)·cos(phi) + cos(β_1)·sin(phi) − sin(β_1));
```

$$\Delta_{y1} := y + r\left(\sin(\beta_1)\cos(\phi) + \cos(\beta_1)\sin(\phi) - \sin(\beta_1)\right) \tag{3}$$

```
> e_1 := Δ_x1·cos(α_1) + Δ_y1·sin(α_1);
```

$$e_1 := \left(x + r\left(\cos(\beta_1)\cos(\phi) - \sin(\beta_1)\sin(\phi) - \cos(\beta_1)\right)\right)\cos(\alpha_1) + \left(y + r\left(\sin(\beta_1)\cos(\phi) + \cos(\beta_1)\sin(\phi) - \sin(\beta_1)\right)\right)\sin(\alpha_1) \tag{4}$$

```
> E_pot,1 := 1/2·k_1·e_1^2;
```

$$E_{pot,1} := \frac{1}{2}\left(k_1\left(\left(x + r\left(\cos(\beta_1)\cos(\phi) - \sin(\beta_1)\sin(\phi) - \cos(\beta_1)\right)\right)\cos(\alpha_1) + \left(y + r\left(\sin(\beta_1)\cos(\phi) + \cos(\beta_1)\sin(\phi) - \sin(\beta_1)\right)\right)\sin(\alpha_1)\right)^2\right) \tag{5}$$

```
> #A:=r·cos(β_1);
  #B:=r·sin(β_1);
  Δ_x1 := x + A·cos(phi) − B·sin(phi) − A;
  Δ_y1 := y + B·cos(phi) + A·sin(phi) − B;
```

$$\Delta_{x1} := x + A\cos(\phi) - B\sin(\phi) - A$$

$$\Delta_{y1} := y + B\cos(\phi) + A\sin(\phi) - B \tag{6}$$

```
> e_1 := Δ_x1·cos(α_1) + Δ_y1·sin(α_1);
  #C:=cos(α_1);
  #D:=sin(α_1);
  e_1 := Δ_x1·C + Δ_y1·D;
  e_1 := C·x + C·A·cos(ϕ) − C·B·sin(ϕ) − C·A + D·y + D·B·cos(ϕ) + D·A·sin(ϕ) − D·B;
```

$$e_1 := \left(x + A\cos(\phi) - B\sin(\phi) - A\right)\cos(\alpha_1) + \left(y + B\cos(\phi) + A\sin(\phi) - B\right)\sin(\alpha_1)$$

$$e_1 := C\left(x + A\cos(\phi) - B\sin(\phi) - A\right) + D\left(y + B\cos(\phi) + A\sin(\phi) - B\right)$$

$$e_1 := C\,x + C\,A\cos(\phi) - C\,B\sin(\phi) - C\,A + D\,y + D\,B\cos(\phi) + D\,A\sin(\phi) - D\,B \tag{7}$$

```
> #1/2·k_1·e_1^2 := 1/2·k_1·[C^2·x^2 + C·x·C·A·cos(ϕ) − C·x·C·B·sin(ϕ) − C·x·C·A + C·x·D·y + C·x
```

$$\cdot \mathrm{D}\cdot B\cdot\cos(\phi) + C\cdot x\cdot \mathrm{D}\cdot A\cdot\sin(\phi) - C\cdot x\cdot \mathrm{D}\cdot B +$$

$$\#\ C\cdot A\cdot cos(\phi)\cdot C\cdot x + C^2\cdot A^2\cdot\cos(\phi)^2 - C\cdot A\cdot\cos(\phi)\cdot C\cdot B\cdot\sin(\phi) - C\cdot A\cdot\cos(\phi)\cdot C\cdot A + C\cdot A \cdot\cos(\phi)\cdot \mathrm{D}\cdot y + C\cdot A\cdot\cos(\phi)\cdot \mathrm{D}\cdot B\cdot\cos(\phi) + C\cdot A\cdot\cos(\phi)\cdot \mathrm{D}\cdot A\cdot\sin(\phi) - C\cdot A\cdot\cos(\phi)\cdot \mathrm{D}\cdot B -$$

$$\#\ C\cdot B\cdot sin(\phi)\cdot C\cdot x - C\cdot B\cdot\sin(\phi)\cdot C\cdot A\cdot\cos(\phi) + C^2\cdot B^2\cdot\sin(\phi)^2 + C\cdot B\cdot\sin(\phi)\cdot C\cdot A - C\cdot B \cdot\sin(\phi)\cdot \mathrm{D}\cdot y - C\cdot B\cdot\sin(\phi)\cdot \mathrm{D}\cdot B\cdot\cos(\phi) - C\cdot B\cdot\sin(\phi)\cdot \mathrm{D}\cdot A\cdot\sin(\phi) + C\cdot B\cdot\sin(\phi)\cdot \mathrm{D}\cdot B -$$

$$\#\ C\cdot A\cdot C\cdot x + C\cdot A\cdot C\cdot A\cdot cos(\phi) + C\cdot A\cdot C\cdot B\cdot\sin(\phi) + C^2\cdot A^2 - C\cdot A\cdot \mathrm{D}\cdot y - C\cdot A\cdot \mathrm{D}\cdot B\cdot\cos(\phi) - C\cdot A\cdot \mathrm{D}\cdot A\cdot\sin(\phi) - C\cdot A\cdot \mathrm{D}\cdot B +$$

$$\#\ D\cdot y\cdot C\cdot x + D\cdot y\cdot C\cdot A\cdot cos(\phi) - \mathrm{D}\cdot y\cdot C\cdot B\cdot\sin(\phi) - \mathrm{D}\cdot y\cdot C\cdot A + \mathrm{D}^2\cdot y^2 + \mathrm{D}\cdot y\cdot \mathrm{D}\cdot B\cdot\cos(\phi) + \mathrm{D} \cdot y\cdot \mathrm{D}\cdot A\cdot\sin(\phi) - \mathrm{D}\cdot y\cdot \mathrm{D}\cdot B +$$

$$\#\ D\cdot B\cdot cos(\phi)\cdot C\cdot x + D\cdot B\cdot cos(\phi)\cdot C\cdot A\cdot\cos(\phi) - D\cdot B\cdot cos(\phi)\cdot C\cdot B\cdot\sin(\phi) - D\cdot B\cdot cos(\phi)\cdot C \cdot A + D\cdot B\cdot cos(\phi)\cdot \mathrm{D}\cdot y + \mathrm{D}^2\cdot B^2\cdot\cos(\phi)^2 + D\cdot B\cdot cos(\phi)\cdot \mathrm{D}\cdot A\cdot\sin(\phi) - D\cdot B\cdot cos(\phi)\cdot \mathrm{D}\cdot B +$$

$$\#`\ \mathrm{D}\cdot A\cdot\sin(\phi)\cdot C\cdot x + \mathrm{D}\cdot A\cdot\sin(\phi)\cdot C\cdot A\cdot\cos(\phi) - \mathrm{D}\cdot A\cdot\sin(\phi)\cdot C\cdot B\cdot\sin(\phi) - \mathrm{D}\cdot A\cdot\sin(\phi)\cdot C \cdot A + \mathrm{D}\cdot A\cdot\sin(\phi)\cdot \mathrm{D}\cdot y + \mathrm{D}\cdot A\cdot\sin(\phi)\cdot \mathrm{D}\cdot B\cdot\cos(\phi) + \mathrm{D}^2\cdot A^2\cdot\sin(\phi)^2 - \mathrm{D}\cdot A\cdot\sin(\phi)\cdot \mathrm{D}\cdot B -$$

$$\#\ D\cdot B\cdot C\cdot x - D\cdot B\cdot C\cdot A\cdot cos(\phi) + \mathrm{D}\cdot B\cdot C\cdot B\cdot\sin(\phi) + \mathrm{D}\cdot B\cdot C\cdot A - \mathrm{D}\cdot B\cdot \mathrm{D}\cdot y - \mathrm{D}\cdot B\cdot \mathrm{D}\cdot B\cdot\cos(\phi) - \mathrm{D}\cdot B\cdot \mathrm{D}\cdot A\cdot\sin(\phi) + \mathrm{D}^2\cdot B^2\Big];$$

```
>
>
```

> #LINEARISE BEFORE DIFFERENTIATING:

$$\#\ sin(\phi) := \phi;$$

$$\#\ cos(\phi) := 1;$$

$$\#\ sin(\varphi)^2 := \phi^2;$$

$$\#\ cos(\varphi)^2 := 1;$$

$$\#\frac{1}{2}k_1{e_1}^2 := \frac{1}{2}k_1\Big[C^2\cdot x^2 + C\cdot x\cdot C\cdot A - C\cdot x\cdot C\cdot B\cdot\phi - C\cdot x\cdot C\cdot A + C\cdot x\cdot \mathrm{D}\cdot y + C\cdot x\cdot \mathrm{D}\cdot B + C\cdot x \cdot \mathrm{D}\cdot A\cdot\phi - C\cdot x\cdot \mathrm{D}\cdot B +$$

$$\#\ C\cdot A\cdot C\cdot x + C^2\cdot A^2 - C\cdot A\cdot C\cdot B\cdot\phi - C\cdot A\cdot C\cdot A + C\cdot A\cdot \mathrm{D}\cdot y + C\cdot A\cdot \mathrm{D}\cdot B + C\cdot A\cdot \mathrm{D}\cdot A\cdot\phi - C\cdot A\cdot \mathrm{D} \cdot B -$$

$$\#\ C\cdot B\cdot\phi\cdot C\cdot x - C\cdot B\cdot\phi\cdot C\cdot A + C^2\cdot B^2\cdot\phi^2 + C\cdot B\cdot\phi\cdot C\cdot A - C\cdot B\cdot\phi\cdot \mathrm{D}\cdot y - C\cdot B\cdot\phi\cdot \mathrm{D}\cdot B - C\cdot B\cdot\phi^2\cdot \mathrm{D} \cdot A + C\cdot B\cdot\phi\cdot \mathrm{D}\cdot B -$$

$$\#\ C\cdot A\cdot C\cdot x + C\cdot A\cdot C\cdot A + C\cdot A\cdot C\cdot B\cdot\phi + C^2\cdot A^2 - C\cdot A\cdot \mathrm{D}\cdot y - C\cdot A\cdot \mathrm{D}\cdot B - C\cdot A\cdot \mathrm{D}\cdot A\cdot\phi - C\cdot A\cdot \mathrm{D}\cdot B +$$

$$\#\ D\cdot y\cdot C\cdot x + D\cdot y\cdot C\cdot A - D\cdot y\cdot C\cdot B\cdot\phi - D\cdot y\cdot C\cdot A + D^2\cdot y^2 + \mathrm{D}\cdot y\cdot \mathrm{D}\cdot B + \mathrm{D}\cdot y\cdot \mathrm{D}\cdot A\cdot\phi - \mathrm{D}\cdot y\cdot \mathrm{D}\cdot B +$$

$$\#\ D\cdot B\cdot C\cdot x + D\cdot B\cdot C\cdot A - D\cdot B\cdot C\cdot B\cdot\phi - D\cdot B\cdot C\cdot A + D\cdot B\cdot D\cdot y + D^2\cdot B^2 + \mathrm{D}\cdot B\cdot \mathrm{D}\cdot A\cdot\phi - \mathrm{D}\cdot B\cdot \mathrm{D}\cdot B$$

Figure A.3

$$+$$
$$\#\ D\cdot A\cdot\phi\cdot C\cdot x+D\cdot A\cdot\phi\cdot C\cdot A-D\cdot A\cdot\phi^2\cdot C\cdot B-\mathrm{D}\cdot A\cdot\phi\cdot C\cdot A+\mathrm{D}\cdot A\cdot\phi\cdot\mathrm{D}\cdot y+\mathrm{D}\cdot A\cdot\phi\cdot\mathrm{D}\cdot B+\mathrm{D}^2\cdot A^2$$
$$\cdot\phi^2-\mathrm{D}\cdot A\cdot\phi\cdot\mathrm{D}\cdot B-$$
$$\#\ D\cdot B\cdot C\cdot x-D\cdot B\cdot C\cdot A+D\cdot B\cdot C\cdot B\cdot\phi+D\cdot B\cdot C\cdot A-D\cdot B\cdot D\cdot y-D\cdot B\cdot D\cdot B-D\cdot B\cdot D\cdot A\cdot\phi+D^2\cdot B^2\Big];$$

> $\#\frac{1}{2}k_1e_1^{\,2}$ *partial derivation with respect* **to** x

$$\#dPdx:=\frac{1}{2}k_1\Big[2\cdot C^2\cdot x+C\cdot C\cdot A-C\cdot C\cdot B\cdot\phi-C\cdot C\cdot A+C\cdot\mathrm{D}\cdot y+C\cdot\mathrm{D}\cdot B+C\cdot\mathrm{D}\cdot A\cdot\phi-C\cdot\mathrm{D}\cdot B$$
$$+$$
$$\#\ C\cdot A\cdot C-$$
$$\#\ C\cdot B\cdot\phi\cdot C-$$
$$\#\ C\cdot A\cdot C+$$
$$\#\ D\cdot y\cdot C+$$
$$\#\ D\cdot B\cdot C+$$
$$\#\ D\cdot A\cdot\phi\cdot C-$$
$$\#\ D\cdot B\cdot C\Big];$$

> *# x :*
> *# Grouping terms:*

$$\#dPdx:=\frac{1}{2}\cdot k_1\cdot\Big[\left(2\cdot C^2\right)\cdot x+\left(2\cdot C\cdot\mathrm{D}\right)\cdot y+\left(-2\cdot B\cdot C^2+2\cdot A\cdot C\cdot\mathrm{D}\right)\cdot\phi\Big]$$

> $\#\frac{1}{2}k_1e_1^{\,2}$ *partial derivation with respect* **to** y

$$\#dPdy:=\frac{1}{2}k_1\Big[C\cdot x\cdot\mathrm{D}+$$
$$\#+C\cdot A\cdot D$$
$$\#-C\cdot B\cdot\phi\cdot D$$
$$\#-C\cdot A\cdot D$$
$$\#+D\cdot C\cdot x+D\cdot C\cdot A-D\cdot C\cdot B\cdot\phi-D\cdot C\cdot A+2\cdot D^2\cdot y+\mathrm{D}\cdot\mathrm{D}\cdot B+\mathrm{D}\cdot\mathrm{D}\cdot A\cdot\phi-\mathrm{D}\cdot\mathrm{D}\cdot B+$$
$$\#\ +D\cdot B\cdot D$$
$$\#+D\cdot A\cdot\phi\cdot D$$
$$\#\ -D\cdot B\cdot D\Big];$$

> *# y :*
> *# Grouping terms:*

$$\#dPdy := \frac{1}{2}\cdot k_1 \cdot \left[(2\cdot C\cdot \mathrm{D})\cdot x + \left(2\cdot \mathrm{D}^2\right)\cdot y + \left(-2\cdot B\cdot C\cdot \mathrm{D} + 2\cdot A\cdot \mathrm{D}^2\right)\cdot \phi \right]$$

>

> # $\frac{1}{2} k_1 e_1{}^2$ *partial derivation with respect* **to** ϕ

$$\#\frac{1}{2} k_1 e_1{}^2 := \frac{1}{2} k_1 \left[C^2\cdot x^2 + C\cdot x\cdot C\cdot A - C\cdot x\cdot C\cdot B\cdot \phi - C\cdot x\cdot C\cdot A + C\cdot x\cdot \mathrm{D}\cdot y + C\cdot x\cdot \mathrm{D}\cdot B + C\cdot x \right.$$
$$\cdot \mathrm{D}\cdot A\cdot \phi - C\cdot x\cdot \mathrm{D}\cdot B +$$
$$\# C\cdot A\cdot C\cdot x + C^2\cdot A^2 - C\cdot A\cdot C\cdot B\cdot \phi - C\cdot A\cdot C\cdot A + C\cdot A\cdot \mathrm{D}\cdot y + C\cdot A\cdot \mathrm{D}\cdot B + C\cdot A\cdot \mathrm{D}\cdot A\cdot \phi - C\cdot A\cdot \mathrm{D}$$
$$\cdot B -$$
$$\# C\cdot B\cdot \phi\cdot C\cdot x - C\cdot B\cdot \phi\cdot C\cdot A + C^2\cdot B^2\cdot \phi^2 + C\cdot B\cdot \phi\cdot C\cdot A - C\cdot B\cdot \phi\cdot \mathrm{D}\cdot y - C\cdot B\cdot \phi\cdot \mathrm{D}\cdot B - C\cdot B\cdot \phi^2\cdot \mathrm{D}$$
$$\cdot A + C\cdot B\cdot \phi\cdot \mathrm{D}\cdot B -$$
$$\# C\cdot A\cdot C\cdot x + C\cdot A\cdot C\cdot A + C\cdot A\cdot C\cdot B\cdot \phi + C^2\cdot A^2 - C\cdot A\cdot \mathrm{D}\cdot y - C\cdot A\cdot \mathrm{D}\cdot B - C\cdot A\cdot \mathrm{D}\cdot A\cdot \phi - C\cdot A\cdot \mathrm{D}\cdot B$$
$$+$$
$$\# D\cdot y\cdot C\cdot x + D\cdot y\cdot C\cdot A - D\cdot y\cdot C\cdot B\cdot \phi - D\cdot y\cdot C\cdot A + D^2\cdot y^2 + \mathrm{D}\cdot y\cdot \mathrm{D}\cdot B + \mathrm{D}\cdot y\cdot \mathrm{D}\cdot A\cdot \phi - \mathrm{D}\cdot y\cdot \mathrm{D}\cdot B +$$
$$\# D\cdot B\cdot C\cdot x + D\cdot B\cdot C\cdot A - D\cdot B\cdot C\cdot B\cdot \phi - D\cdot B\cdot C\cdot A + D\cdot B\cdot D\cdot y + D^2\cdot B^2 + \mathrm{D}\cdot B\cdot \mathrm{D}\cdot A\cdot \phi - \mathrm{D}\cdot B\cdot \mathrm{D}\cdot B$$
$$+$$
$$\# D\cdot A\cdot \phi\cdot C\cdot x + D\cdot A\cdot \phi\cdot C\cdot A - D\cdot A\cdot \phi^2\cdot C\cdot B - \mathrm{D}\cdot A\cdot \phi\cdot C\cdot A + \mathrm{D}\cdot A\cdot \phi\cdot \mathrm{D}\cdot y + \mathrm{D}\cdot A\cdot \phi\cdot \mathrm{D}\cdot B + \mathrm{D}^2\cdot A^2$$
$$\cdot \phi^2 - \mathrm{D}\cdot A\cdot \phi\cdot \mathrm{D}\cdot B -$$
$$\left.\# D\cdot B\cdot C\cdot x - D\cdot B\cdot C\cdot A + D\cdot B\cdot C\cdot B\cdot \phi + D\cdot B\cdot C\cdot A - D\cdot B\cdot D\cdot y - D\cdot B\cdot D\cdot B - D\cdot B\cdot D\cdot A\cdot \phi + D^2\cdot B^2 \right];$$

$$\#dPd\varphi := \frac{1}{2} k_1 \left[-C\cdot x\cdot C\cdot B + C\cdot x\cdot \mathrm{D}\cdot A + \right.$$
$$\#`-`C\cdot A\cdot C\cdot B + C\cdot A\cdot D\cdot A -$$
$$\# C\cdot B\cdot C\cdot x - C\cdot B\cdot C\cdot A + 2\cdot C^2\cdot B^2\cdot \phi + C\cdot B\cdot C\cdot A - C\cdot B\cdot \mathrm{D}\cdot y - C\cdot B\cdot \mathrm{D}\cdot B - 2\cdot C\cdot B\cdot \phi\cdot \mathrm{D}\cdot A + C$$
$$\cdot B\cdot \mathrm{D}\cdot B$$
$$\# + C\cdot A\cdot C\cdot B - C\cdot A\cdot D\cdot A$$
$$\#` `- D\cdot y\cdot C\cdot B + D\cdot y\cdot D\cdot A$$
$$\# - D\cdot B\cdot C\cdot B + D\cdot B\cdot D\cdot A +$$
$$\# D\cdot A\cdot C\cdot x + D\cdot A\cdot C\cdot A - 2\cdot D\cdot A\cdot \phi\cdot C\cdot B - D\cdot A\cdot C\cdot A + D\cdot A\cdot D\cdot y + D\cdot A\cdot D\cdot B + 2\cdot D^2\cdot A^2\cdot \phi - \mathrm{D}\cdot A\cdot \mathrm{D}$$
$$\cdot B$$
$$\left.\# + D\cdot B\cdot C\cdot B - D\cdot B\cdot D\cdot A \right];$$

>

> # ϕ :
> # *Grouping terms:*

$$\#dPd\varphi := \frac{1}{2}\cdot k_1\cdot\left[\left(-2\cdot B\cdot C^2+2\cdot A\cdot C\cdot D\right)\cdot x+\left(-2\cdot B\cdot C\cdot D+2\cdot A\cdot D^2\right)\cdot y+\left(2\cdot B^2\cdot C^2-4\cdot A\cdot B\cdot C\cdot D+2\cdot A^2\cdot D^2\right)\cdot\phi\right]$$

$$\#dP1dx := \frac{1}{2}\cdot k_1\cdot\left[\left(2\cdot C^2\right)\cdot x+\left(2\cdot C\cdot d\right)\cdot y+\left(-2\cdot B\cdot C^2+2\cdot A\cdot C\cdot d\right)\cdot\phi\right];$$

$$\#dP1dy := \frac{1}{2}\cdot k_1\cdot\left[\left(2\cdot C\cdot d\right)\cdot x+\left(2\cdot d^2\right)\cdot y+\left(-2\cdot B\cdot C\cdot d+2\cdot A\cdot d^2\right)\cdot\phi\right];$$

$$\#dP1d\varphi := \frac{1}{2}\cdot k_1\cdot\left[\left(-2\cdot B\cdot C^2+2\cdot A\cdot C\cdot d\right)\cdot x+\left(-2\cdot B\cdot C\cdot d+2\cdot A\cdot d^2\right)\cdot y+\left(2\cdot B^2\cdot C^2-4\cdot A\cdot B\cdot C\cdot d+2\cdot A^2\cdot d^2\right)\cdot\phi\right];$$

```
restart;
interface(displayprecision = 5) :
```

$$e_1 := \Delta_{x1}\cdot\cos\left(\alpha_1\right)+\Delta_{y1}\cdot\sin\left(\alpha_1\right);$$

$$\#C := cos\left(\alpha_1\right);$$

$$\#d := sin\left(\alpha_1\right);$$

$$e_1 := \Delta_{x1}\cdot C+\Delta_{y1}\cdot d;$$

$$e_1 := \Delta_{x1}\cos\left(\alpha_1\right)+\Delta_{y1}\sin\left(\alpha_1\right)$$

$$e_1 := \Delta_{x1}\,C+\Delta_{y1}\,d \tag{8}$$

$$dP1dx := \frac{1}{2}\cdot k_1\cdot\left[\left(2\cdot C^2\right)\cdot x+\left(2\cdot C\cdot d\right)\cdot y+\left(-2\cdot B\cdot C^2+2\cdot A\cdot C\cdot d\right)\cdot\phi\right];$$

$$dP1dy := \frac{1}{2}\cdot k_1\cdot\left[\left(2\cdot C\cdot d\right)\cdot x+\left(2\cdot d^2\right)\cdot y+\left(-2\cdot B\cdot C\cdot d+2\cdot A\cdot d^2\right)\cdot\phi\right];$$

$$dP1d\varphi := \frac{1}{2}\cdot k_1\cdot\left[\left(-2\cdot B\cdot C^2+2\cdot A\cdot C\cdot d\right)\cdot x+\left(-2\cdot B\cdot C\cdot d+2\cdot A\cdot d^2\right)\cdot y+\left(2\cdot B^2\cdot C^2-4\cdot A\cdot B\cdot C\cdot d+2\cdot A^2\cdot d^2\right)\cdot\phi\right];$$

$$dP1dx := \frac{k_1\left[2\,C^2\,x+2\,C\,d\,y+\left(2\,A\,C\,d-2\,B\,C^2\right)\phi\right]}{2}$$

$$dP1dy := \frac{k_1\left[2\,C\,d\,x+2\,d^2\,y+\left(2\,A\,d^2-2\,B\,C\,d\right)\phi\right]}{2}$$

$$dP1d\varphi := \frac{k_1\left[\left(2\,A\,C\,d-2\,B\,C^2\right)x+\left(2\,A\,d^2-2\,B\,C\,d\right)y+\left(2\,A^2\,d^2-4\,A\,B\,C\,d+2\,B^2\,C^2\right)\phi\right]}{2} \tag{9}$$

```
> #NOW FOR ALL SPRING
  restart;
  interface(displayprecision = 5) :
```

```
> e_1 := Δ_x1·C + Δ_y1·d;
  e_2 := Δ_x2·C + Δ_y2·d;
  e_3 := Δ_x3·C + Δ_y3·d;
  e_4 := Δ_x4·C + Δ_y4·d;
```

$$e_1 := \Delta_{x1}\,C + \Delta_{y1}\,d$$
$$e_2 := \Delta_{x2}\,C + \Delta_{y2}\,d$$
$$e_3 := \Delta_{x3}\,C + \Delta_{y3}\,d$$
$$e_4 := \Delta_{x4}\,C + \Delta_{y4}\,d \qquad \textbf{(10)}$$

```
> r := 0.05 :
  β_1 := 160/180·Pi :
  β_2 := 20/180·Pi :
  β_3 := 200/180·Pi :
  β_4 := 340/180·Pi :
```

```
> A := r·cos(β_1) :
  B := r·sin(β_1) :
  C := cos(α_1) :
  d := sin(α_1) :
  dP1dx := 1/2·k_1·((2·C^2)·x + (2·C·d)·y + (-2·B·C^2 + 2·A·C·d)·ϕ) :
  simplify(dP1dx);
  dP1dy := 1/2·k_1·((2·C·d)·x + (2·d^2)·y + (-2·B·C·d + 2·A·d^2)·ϕ) :
  simplify(dP1dy);
  dP1dφ := 1/2·k_1·((-2·B·C^2 + 2·A·C·d)·x + (-2·B·C·d + 2·A·d^2)·y + (2·B^2·C^2 - 4·A
      ·B·C·d + 2·A^2·d^2)·ϕ) :
  simplify(dP1dφ);
```

$$k_1\left((x - 0.01710\,\phi)\cos(\alpha_1) + (y - 0.04698\,\phi)\sin(\alpha_1)\right)\cos(\alpha_1)$$
$$k_1\left((x - 0.01710\,\phi)\cos(\alpha_1) + (y - 0.04698\,\phi)\sin(\alpha_1)\right)\sin(\alpha_1)$$
$$-0.01710\,k_1\left(\left(-2.74748\,y + 0.11199\,\phi + 1.00000\,x\right)\cos(\alpha_1)\right)^2 + \left(2.74748\,x + 1.00000\,y \right. \qquad \textbf{(11)}$$

$$-0.09397\,\phi)\,\sin(\alpha_1)\,\cos(\alpha_1)+2.74748\,y-0.12909\,\phi)$$

```
> A := r·cos(β2) :
  B := r·sin(β2) :
  C := cos(α2) :
  d := sin(α2) :
  dP2dx := 1/2·k1·((2·C^2)·x + (2·C·d)·y + (-2·B·C^2 + 2·A·C·d)·ϕ) :
  simplify(dP2dx);
  dP2dy := 1/2·k1·((2·C·d)·x + (2·d^2)·y + (-2·B·C·d + 2·A·d^2)·ϕ) :
  simplify(dP2dy);
  dP2dφ := 1/2·k1·((-2·B·C^2 + 2·A·C·d)·x + (-2·B·C·d + 2·A·d^2)·y + (2·B^2·C^2 − 4·A
      ·B·C·d + 2·A^2·d^2)·ϕ) :
  simplify(dP2dφ);
```

$$\left((x-0.01710\,\phi)\,\cos(\alpha_2)+(y+0.04698\,\phi)\,\sin(\alpha_2)\right)k_1\cos(\alpha_2)$$

$$\left((x-0.01710\,\phi)\,\cos(\alpha_2)+(y+0.04698\,\phi)\,\sin(\alpha_2)\right)k_1\sin(\alpha_2)$$

$$-0.01710\,k_1\left((2.74748\,y+0.11199\,\phi+1.00000\,x)\,\cos(\alpha_2)^2+(-2.74748\,x+1.00000\,y+0.09397\,\phi)\,\sin(\alpha_2)\,\cos(\alpha_2)-2.74748\,y-0.12909\,\phi\right) \quad \textbf{(12)}$$

```
> A := r·cos(β3) :
  B := r·sin(β3) :
  C := cos(α3) :
  d := sin(α3) :
  dP3dx := 1/2·k1·((2·C^2)·x + (2·C·d)·y + (-2·B·C^2 + 2·A·C·d)·ϕ) :
  simplify(dP3dx);
  dP3dy := 1/2·k1·((2·C·d)·x + (2·d^2)·y + (-2·B·C·d + 2·A·d^2)·ϕ) :
  simplify(dP3dy);
  dP3dφ := 1/2·k1·((-2·B·C^2 + 2·A·C·d)·x + (-2·B·C·d + 2·A·d^2)·y + (2·B^2·C^2 − 4·A
      ·B·C·d + 2·A^2·d^2)·ϕ) :
  simplify(dP3dφ);
```

$$k_1\cos(\alpha_3)\left((x+0.01710\,\phi)\,\cos(\alpha_3)+(y-0.04698\,\phi)\,\sin(\alpha_3)\right)$$

$$k_1\left((x+0.01710\,\phi)\,\cos(\alpha_3)+(y-0.04698\,\phi)\,\sin(\alpha_3)\right)\sin(\alpha_3)$$

$$0.01710\left((2.74748\,y-0.11199\,\phi+1.00000\,x)\,\cos(\alpha_3)^2+(-2.74748\,x+1.00000\,y \quad \textbf{(13)}$$

$$-0.09397\,\phi)\,\sin(\alpha_3)\,\cos(\alpha_3) - 2.74748\,y + 0.12909\,\phi\Big)\,k_1$$

```
> A := r·cos(β4) :
  B := r·sin(β4) :
  C := cos(α4) :
  d := sin(α4) :
  dP4dx := 1/2·k1·((2·C^2)·x + (2·C·d)·y + (-2·B·C^2 + 2·A·C·d)·φ) :
   simplify(dP4dx);
  dP4dy := 1/2·k1·((2·C·d)·x + (2·d^2)·y + (-2·B·C·d + 2·A·d^2)·φ) :
   simplify(dP4dy);
  dP4dφ := 1/2·k1·((-2·B·C^2 + 2·A·C·d)·x + (-2·B·C·d + 2·A·d^2)·y + (2·B^2·C^2 − 4·A
      ·B·C·d + 2·A^2·d^2)·φ) :
   simplify(dP4dφ);
```

$$\big((x + 0.01710\,\phi)\,\cos(\alpha_4) + (y + 0.04698\,\phi)\,\sin(\alpha_4)\big)\,k_1\cos(\alpha_4)$$

$$\big((x + 0.01710\,\phi)\,\cos(\alpha_4) + (y + 0.04698\,\phi)\,\sin(\alpha_4)\big)\,k_1\sin(\alpha_4)$$

$$0.01710\,\Big((-2.74748\,y - 0.11199\,\phi + 1.00000\,x)\,\cos(\alpha_4)^2 + (2.74748\,x + 1.00000\,y + 0.09397\,\phi)\,\sin(\alpha_4)\,\cos(\alpha_4) + 2.74748\,y + 0.12909\,\phi\Big)\,k_1 \qquad \textbf{(14)}$$

```
> dPdx := dP1dx + dP2dx + dP3dx + dP4dx :
  dPdx := evalf(dPdx) :
  simplify(dPdx);
  dPdy := dP1dy + dP2dy + dP3dy + dP4dy :
  dPdy := evalf(dPdy) :
  simplify(dPdy);
  dPdφ := dP1dφ + dP2dφ + dP3dφ + dP4dφ :
  dPdφ := evalf(dPdφ) :
  simplify(dPdφ);
```

$$\Big((x - 0.01710\,\phi)\,\cos(\alpha_1)^2 + (y - 0.04698\,\phi)\,\sin(\alpha_1)\,\cos(\alpha_1) + (x - 0.01710\,\phi)\,\cos(\alpha_2)^2 + (y + 0.04698\,\phi)\,\sin(\alpha_2)\,\cos(\alpha_2) + (x + 0.01710\,\phi)\,\cos(\alpha_3)^2 + (y - 0.04698\,\phi)\,\sin(\alpha_3)\,\cos(\alpha_3) + (x + 0.01710\,\phi)\,\cos(\alpha_4)^2 + (y + 0.04698\,\phi)\,\cos(\alpha_4)\,\sin(\alpha_4)\Big)\,k_1$$

$$k_1\,\Big((-1.00000\,y + 0.04698\,\phi)\,\cos(\alpha_1)^2 + (x - 0.01710\,\phi)\,\sin(\alpha_1)\,\cos(\alpha_1) + (-1.00000\,y - 0.04698\,\phi)\,\cos(\alpha_2)^2 + (x - 0.01710\,\phi)\,\sin(\alpha_2)\,\cos(\alpha_2) + (-1.00000\,y$$

$$
\begin{aligned}
&+0.04698\,\phi)\cos(\alpha_3)^2+(x+0.01710\,\phi)\sin(\alpha_3)\cos(\alpha_3)+(-1.00000\,y\\
&-0.04698\,\phi)\cos(\alpha_4)^2+(x+0.01710\,\phi)\cos(\alpha_4)\sin(\alpha_4)+4.00000\,y\Big)\\
-0.01710\,&\Big((-2.74748\,y+1.00000\,x+0.11199\,\phi)\cos(\alpha_1)^2+(1.00000\,y-0.09397\,\phi \qquad \textbf{(15)}\\
&+2.74748\,x)\sin(\alpha_1)\cos(\alpha_1)+(2.74748\,y+1.00000\,x+0.11199\,\phi)\cos(\alpha_2)^2\\
&+(1.00000\,y+0.09397\,\phi-2.74748\,x)\sin(\alpha_2)\cos(\alpha_2)+(-2.74748\,y-1.00000\,x\\
&+0.11199\,\phi)\cos(\alpha_3)^2+(-1.00000\,y+0.09397\,\phi+2.74748\,x)\sin(\alpha_3)\cos(\alpha_3)\\
&+(2.74748\,y-1.00000\,x+0.11199\,\phi)\cos(\alpha_4)^2+(-1.00000\,y-0.09397\,\phi\\
&-2.74748\,x)\sin(\alpha_4)\cos(\alpha_4)-0.51636\,\phi\Big)\,k_1
\end{aligned}
$$

>

>

A.3.2. α equals 0

```
> #NU VOOR ALLE VEREN:
  restart;
  interface(displayprecision = 5) :
> e1 := Δx1·C + Δy1·d;
  e2 := Δx2·C + Δy2·d;
  e3 := Δx3·C + Δy3·d;
  e4 := Δx4·C + Δy4·d;
```

$$e_1 := \Delta_{x1} C + \Delta_{y1} d$$
$$e_2 := \Delta_{x2} C + \Delta_{y2} d$$
$$e_3 := \Delta_{x3} C + \Delta_{y3} d$$
$$e_4 := \Delta_{x4} C + \Delta_{y4} d \quad \textbf{(1)}$$

```
> r := 0.05 :
  α4 := alpha :
  α3 := alpha :
  α2 := alpha :
  α1 := alpha :
  alpha := 0 :
  β1 := 160/180 ·Pi :
  β2 := 20/180 ·Pi :
  β3 := 200/180 ·Pi :
  β4 := 340/180 ·Pi :
> A := r·cos(β1) :
  B := r·sin(β1) :
  C := cos(α1) :
  d := sin(α1) :
  dP1dx := 1/2 ·k1·((2· C^2)·x + (2· C·d)·y + (-2· B·C^2 + 2· A·C·d)·ϕ) :
  simplify(dP1dx);
  dP1dy := 1/2 ·k1·((2· C·d)·x + (2·d^2)·y + (-2· B·C·d + 2· A·d^2)·ϕ) :
  simplify(dP1dy);
  dP1dφ := 1/2 ·k1·((-2· B·C^2 + 2· A·C·d)·x + (-2· B·C·d + 2· A·d^2)·y + (2·B^2·C^2 - 4·A
      ·B·C·d + 2·A^2·d^2)·ϕ) :
```

```
simplify(dP1dφ);
```

$$(x - 0.01710\,\phi)\,k_1$$
$$0$$
$$(-0.01710\,x + 0.00029\,\phi)\,k_1 \qquad (2)$$

```
> A := r·cos(β2) :
  B := r·sin(β2) :
  C := cos(α2) :
  d := sin(α2) :
  dP2dx := 1/2·k1·((2·C^2)·x + (2·C·d)·y + (-2·B·C^2 + 2·A·C·d)·φ) :
  simplify(dP2dx);
  dP2dy := 1/2·k1·((2·C·d)·x + (2·d^2)·y + (-2·B·C·d + 2·A·d^2)·φ) :
  simplify(dP2dy);
  dP2dφ := 1/2·k1·((-2·B·C^2 + 2·A·C·d)·x + (-2·B·C·d + 2·A·d^2)·y + (2·B^2·C^2 - 4·A
      ·B·C·d + 2·A^2·d^2)·φ) :
  simplify(dP2dφ);
```

$$(x - 0.01710\,\phi)\,k_1$$
$$0$$
$$(-0.01710\,x + 0.00029\,\phi)\,k_1 \qquad (3)$$

```
> A := r·cos(β3) :
  B := r·sin(β3) :
  C := cos(α3) :
  d := sin(α3) :
  dP3dx := 1/2·k1·((2·C^2)·x + (2·C·d)·y + (-2·B·C^2 + 2·A·C·d)·φ) :
  simplify(dP3dx);
  dP3dy := 1/2·k1·((2·C·d)·x + (2·d^2)·y + (-2·B·C·d + 2·A·d^2)·φ) :
  simplify(dP3dy);
  dP3dφ := 1/2·k1·((-2·B·C^2 + 2·A·C·d)·x + (-2·B·C·d + 2·A·d^2)·y + (2·B^2·C^2 - 4·A
      ·B·C·d + 2·A^2·d^2)·φ) :
  simplify(dP3dφ);
```

$$(x + 0.01710\,\phi)\,k_1$$
$$0$$
$$(0.01710\,x + 0.00029\,\phi)\,k_1 \qquad (4)$$

```
> A := r·cos(β4) :
```

$$B := r\cdot\sin(\beta_4):$$
$$C := \cos(\alpha_4):$$
$$d := \sin(\alpha_4):$$
$$dP4dx := \frac{1}{2}\cdot k_1\cdot\left(\left(2\cdot C^2\right)\cdot x + (2\cdot C\cdot d)\cdot y + \left(-2\cdot B\cdot C^2 + 2\cdot A\cdot C\cdot d\right)\cdot\phi\right):$$
$$simplify(dP4dx);$$
$$dP4dy := \frac{1}{2}\cdot k_1\cdot\left((2\cdot C\cdot d)\cdot x + \left(2\cdot d^2\right)\cdot y + \left(-2\cdot B\cdot C\cdot d + 2\cdot A\cdot d^2\right)\cdot\phi\right):$$
$$simplify(dP4dy);$$
$$dP4d\varphi := \frac{1}{2}\cdot k_1\cdot\left(\left(-2\cdot B\cdot C^2 + 2\cdot A\cdot C\cdot d\right)\cdot x + \left(-2\cdot B\cdot C\cdot d + 2\cdot A\cdot d^2\right)\cdot y + \left(2\cdot B^2\cdot C^2 - 4\cdot A\cdot B\cdot C\cdot d + 2\cdot A^2\cdot d^2\right)\cdot\phi\right):$$
$$simplify(dP4d\varphi);$$

$$\begin{bmatrix}(x + 0.01710\,\phi)\,k_1\\ 0\\ (0.01710\,x + 0.00029\,\phi)\,k_1\end{bmatrix} \quad (5)$$

```
> dPdx := dP1dx + dP2dx + dP3dx + dP4dx:
  dPdx := evalf(dPdx):
  simplify(dPdx);
  dPdy := dP1dy + dP2dy + dP3dy + dP4dy:
  dPdy := evalf(dPdy):
  simplify(dPdy);
  dPdφ := dP1dφ + dP2dφ + dP3dφ + dP4dφ:
  dPdφ := evalf(dPdφ):
  simplify(dPdφ);
```

$$\begin{bmatrix}4.00000\,k_1\,x\\ 0.\\ 0.00117\,k_1\,\phi\end{bmatrix} \quad (6)$$

The resulting equations of motion can be found below:

$$\begin{bmatrix} m & 0 & 0\\ 0 & m & 0\\ 0 & 0 & J\end{bmatrix}\begin{bmatrix}\ddot{x}\\ \ddot{y}\\ \ddot{\phi}\end{bmatrix} + k * \begin{bmatrix} 4 & 0 & 0\\ 0 & 0 & 0\\ 0 & 0 & 0.00117\end{bmatrix}\begin{bmatrix} x\\ y\\ \phi\end{bmatrix} = \begin{bmatrix}\sum F_r\\ 0\\ \sum M_r\end{bmatrix}$$

A.3.3. $\alpha_1 = \alpha_2 = \alpha_3 = \alpha_4 =$ not 0

```
#NU VOOR ALLE VEREN:
restart;
interface(displayprecision = 5) :
```

```
e_1 := Δ_x1·C + Δ_y1·d;
e_2 := Δ_x2·C + Δ_y2·d;
e_3 := Δ_x3·C + Δ_y3·d;
e_4 := Δ_x4·C + Δ_y4·d;
```

$$e_1 := \Delta_{x1} C + \Delta_{y1} d$$
$$e_2 := \Delta_{x2} C + \Delta_{y2} d$$
$$e_3 := \Delta_{x3} C + \Delta_{y3} d$$
$$e_4 := \Delta_{x4} C + \Delta_{y4} d \quad \textbf{(1)}$$

```
r := 0.05 :
α_4 := 1/180 ·Pi :
α_3 := 1/180 ·Pi :
α_2 := 1/180 ·Pi :
α_1 := 1/180 ·Pi :
β_1 := 160/180 ·Pi :
β_2 := 20/180 ·Pi :
β_3 := 200/180 ·Pi :
β_4 := 340/180 ·Pi :
```

```
A := r·cos(β_1) :
B := r·sin(β_1) :
C := cos(α_1) :
d := sin(α_1) :
dP1dx := 1/2 ·k_1·((2·C^2)·x + (2·C·d)·y + (-2·B·C^2 + 2·A·C·d)·ϕ) :
simplify(dP1dx);
dP1dy := 1/2 ·k_1·((2·C·d)·x + (2·d^2)·y + (-2·B·C·d + 2·A·d^2)·ϕ) :
simplify(dP1dy);
dP1dφ := 1/2 ·k_1·((-2·B·C^2 + 2·A·C·d)·x + (-2·B·C·d + 2·A·d^2)·y + (2·B^2·C^2 − 4·A
```

$$\cdot B\cdot C\cdot d + 2\cdot A^2\cdot d^2\big)\cdot\phi\big):$$

simplify(*dP1dφ*);

$$\left(-0.01791\,\phi + 0.01745\,y + 0.99970\,x\right) k_1$$

$$\left(-0.00036\,\phi + 0.00030\,y + 0.01745\,x\right) k_1$$

$$\left(-0.01792\,x - 0.00031\,y + 0.00032\,\phi\right) k_1 \qquad \textbf{(2)}$$

> $A := r\cdot\cos\left(\beta_2\right):$

$B := r\cdot\sin\left(\beta_2\right):$

$C := \cos\left(\alpha_2\right):$

$d := \sin\left(\alpha_2\right):$

$dP2dx := \frac{1}{2}\cdot k_1\cdot\left(\left(2\cdot C^2\right)\cdot x + (2\cdot C\cdot d)\cdot y + \left(-2\cdot B\cdot C^2 + 2\cdot A\cdot C\cdot d\right)\cdot\phi\right):$

simplify(*dP2dx*);

$dP2dy := \frac{1}{2}\cdot k_1\cdot\left((2\cdot C\cdot d)\cdot x + \left(2\cdot d^2\right)\cdot y + \left(-2\cdot B\cdot C\cdot d + 2\cdot A\cdot d^2\right)\cdot\phi\right):$

simplify(*dP2dy*);

$dP2d\varphi := \frac{1}{2}\cdot k_1\cdot\left(\left(-2\cdot B\cdot C^2 + 2\cdot A\cdot C\cdot d\right)\cdot x + \left(-2\cdot B\cdot C\cdot d + 2\cdot A\cdot d^2\right)\cdot y + \left(2\cdot B^2\cdot C^2 - 4\cdot A\right.$

$\left.\cdot B\cdot C\cdot d + 2\cdot A^2\cdot d^2\right)\cdot\phi\big):$

simplify(*dP2dφ*);

$$\left(-0.01628\,\phi + 0.01745\,y + 0.99970\,x\right) k_1$$

$$\left(-0.00028\,\phi + 0.00030\,y + 0.01745\,x\right) k_1$$

$$\left(-0.01628\,x - 0.00028\,y + 0.00026\,\phi\right) k_1 \qquad \textbf{(3)}$$

> $A := r\cdot\cos\left(\beta_3\right):$

$B := r\cdot\sin\left(\beta_3\right):$

$C := \cos\left(\alpha_3\right):$

$d := \sin\left(\alpha_3\right):$

$dP3dx := \frac{1}{2}\cdot k_1\cdot\left(\left(2\cdot C^2\right)\cdot x + (2\cdot C\cdot d)\cdot y + \left(-2\cdot B\cdot C^2 + 2\cdot A\cdot C\cdot d\right)\cdot\phi\right):$

simplify(*dP3dx*);

$dP3dy := \frac{1}{2}\cdot k_1\cdot\left((2\cdot C\cdot d)\cdot x + \left(2\cdot d^2\right)\cdot y + \left(-2\cdot B\cdot C\cdot d + 2\cdot A\cdot d^2\right)\cdot\phi\right):$

simplify(*dP3dy*);

$dP3d\varphi := \frac{1}{2}\cdot k_1\cdot\left(\left(-2\cdot B\cdot C^2 + 2\cdot A\cdot C\cdot d\right)\cdot x + \left(-2\cdot B\cdot C\cdot d + 2\cdot A\cdot d^2\right)\cdot y + \left(2\cdot B^2\cdot C^2 - 4\cdot A\right.$

$\left.\cdot B\cdot C\cdot d + 2\cdot A^2\cdot d^2\right)\cdot\phi\big):$

simplify(*dP3dφ*);

$$\left(0.01628\,\phi + 0.01745\,y + 0.99970\,x\right) k_1$$

$$\left(0.00028\,\phi + 0.00030\,y + 0.01745\,x\right) k_1$$

(4)

$$(0.01628\,x + 0.00028\,y + 0.00026\,\phi)\,k_1 \tag{4}$$

```
> A := r·cos(β4) :
  B := r·sin(β4) :
  C := cos(α4) :
  d := sin(α4) :
  dP4dx := 1/2·k1·((2·C^2)·x + (2·C·d)·y + (-2·B·C^2 + 2·A·C·d)·ϕ) :
  simplify(dP4dx);
  dP4dy := 1/2·k1·((2·C·d)·x + (2·d^2)·y + (-2·B·C·d + 2·A·d^2)·ϕ) :
  simplify(dP4dy);
  dP4dφ := 1/2·k1·((-2·B·C^2 + 2·A·C·d)·x + (-2·B·C·d + 2·A·d^2)·y + (2·B^2·C^2 - 4·A
      ·B·C·d + 2·A^2·d^2)·ϕ) :
  simplify(dP4dφ);
```

$$(0.01791\,\phi + 0.01745\,y + 0.99970\,x)\,k_1$$

$$(0.00036\,\phi + 0.00030\,y + 0.01745\,x)\,k_1$$

$$(0.01792\,x + 0.00031\,y + 0.00032\,\phi)\,k_1 \tag{5}$$

```
> dPdx := dP1dx + dP2dx + dP3dx + dP4dx :
  dPdx := evalf(dPdx) :
  simplify(dPdx);
  dPdy := dP1dy + dP2dy + dP3dy + dP4dy :
  dPdy := evalf(dPdy) :
  simplify(dPdy);
  dPdφ := dP1dφ + dP2dφ + dP3dφ + dP4dφ :
  dPdφ := evalf(dPdφ) :
  simplify(dPdφ);
```

$$k_1\,(3.99878\,x + 0.06980\,y)$$

$$k_1\,(0.06980\,x + 0.00122\,y)$$

$$0.00117\,k_1\,\phi \tag{6}$$

```
>
>
```

The resulting equations of motion can be found below:

$$\begin{bmatrix} m & 0 & 0 \\ 0 & m & 0 \\ 0 & 0 & J \end{bmatrix} \begin{bmatrix} \ddot{x} \\ \ddot{y} \\ \ddot{\phi} \end{bmatrix} + k * \begin{bmatrix} 3.99878 & 0.06980 & 0 \\ 0.06980 & 0.00122 & 0 \\ 0 & 0 & 0.00117 \end{bmatrix} \begin{bmatrix} x \\ y \\ \phi \end{bmatrix} = \begin{bmatrix} \sum F_r \\ 0 \\ \sum M_r \end{bmatrix}$$

A.3.4. $\alpha_1 = \alpha_2 = -\alpha_3 = -\alpha_4$ = not 0

```
> #NU VOOR ALLE VEREN:
  restart;
  interface(displayprecision = 5) :
> e_1 := Δ_x1·C + Δ_y1·d;
  e_2 := Δ_x2·C + Δ_y2·d;
  e_3 := Δ_x3·C + Δ_y3·d;
  e_4 := Δ_x4·C + Δ_y4·d;
```

$$e_1 := \Delta_{x1} C + \Delta_{y1} d$$
$$e_2 := \Delta_{x2} C + \Delta_{y2} d$$
$$e_3 := \Delta_{x3} C + \Delta_{y3} d$$
$$e_4 := \Delta_{x4} C + \Delta_{y4} d \quad \textbf{(1)}$$

```
> r := 0.05 :
  α_4 := -1/180·Pi :
  α_3 := -1/180·Pi :
  α_2 := 1/180·Pi :
  α_1 := 1/180·Pi :
  β_1 := 160/180·Pi :
  β_2 := 20/180·Pi :
  β_3 := 200/180·Pi :
  β_4 := 340/180·Pi :
> A := r·cos(β_1) :
  B := r·sin(β_1) :
  C := cos(α_1) :
  d := sin(α_1) :
  dP1dx := 1/2·k_1·((2·C^2)·x + (2·C·d)·y + (-2·B·C^2 + 2·A·C·d)·ϕ) :
  simplify(dP1dx);
  dP1dy := 1/2·k_1·((2·C·d)·x + (2·d^2)·y + (-2·B·C·d + 2·A·d^2)·ϕ) :
  simplify(dP1dy);
  dP1dφ := 1/2·k_1·((-2·B·C^2 + 2·A·C·d)·x + (-2·B·C·d + 2·A·d^2)·y + (2·B^2·C^2 − 4·A
```

$$\cdot B\cdot C\cdot d + 2\cdot A^2\cdot d^2\big)\cdot\phi\big):$$

$$simplify(dP1d\varphi);$$

$$\big(-0.01791\,\phi + 0.01745\,y + 0.99970\,x\big)\,k_1$$

$$\big(-0.00036\,\phi + 0.00030\,y + 0.01745\,x\big)\,k_1$$

$$\big(-0.01792\,x - 0.00031\,y + 0.00032\,\phi\big)\,k_1 \qquad \textbf{(2)}$$

> $A := r\cdot\cos\big(\beta_2\big):$

$B := r\cdot\sin\big(\beta_2\big):$

$C := \cos\big(\alpha_2\big):$

$d := \sin\big(\alpha_2\big):$

$$dP2dx := \frac{1}{2}\cdot k_1\cdot\big(\big(2\cdot C^2\big)\cdot x + (2\cdot C\cdot d)\cdot y + \big(-2\cdot B\cdot C^2 + 2\cdot A\cdot C\cdot d\big)\cdot\phi\big):$$

$$simplify(dP2dx);$$

$$dP2dy := \frac{1}{2}\cdot k_1\cdot\big((2\cdot C\cdot d)\cdot x + \big(2\cdot d^2\big)\cdot y + \big(-2\cdot B\cdot C\cdot d + 2\cdot A\cdot d^2\big)\cdot\phi\big):$$

$$simplify(dP2dy);$$

$$dP2d\varphi := \frac{1}{2}\cdot k_1\cdot\big(\big(-2\cdot B\cdot C^2 + 2\cdot A\cdot C\cdot d\big)\cdot x + \big(-2\cdot B\cdot C\cdot d + 2\cdot A\cdot d^2\big)\cdot y + \big(2\cdot B^2\cdot C^2 - 4\cdot A$$

$$\cdot B\cdot C\cdot d + 2\cdot A^2\cdot d^2\big)\cdot\phi\big):$$

$$simplify(dP2d\varphi);$$

$$\big(-0.01628\,\phi + 0.01745\,y + 0.99970\,x\big)\,k_1$$

$$\big(-0.00028\,\phi + 0.00030\,y + 0.01745\,x\big)\,k_1$$

$$\big(-0.01628\,x - 0.00028\,y + 0.00026\,\phi\big)\,k_1 \qquad \textbf{(3)}$$

> $A := r\cdot\cos\big(\beta_3\big):$

$B := r\cdot\sin\big(\beta_3\big):$

$C := \cos\big(\alpha_3\big):$

$d := \sin\big(\alpha_3\big):$

$$dP3dx := \frac{1}{2}\cdot k_1\cdot\big(\big(2\cdot C^2\big)\cdot x + (2\cdot C\cdot d)\cdot y + \big(-2\cdot B\cdot C^2 + 2\cdot A\cdot C\cdot d\big)\cdot\phi\big):$$

$$simplify(dP3dx);$$

$$dP3dy := \frac{1}{2}\cdot k_1\cdot\big((2\cdot C\cdot d)\cdot x + \big(2\cdot d^2\big)\cdot y + \big(-2\cdot B\cdot C\cdot d + 2\cdot A\cdot d^2\big)\cdot\phi\big):$$

$$simplify(dP3dy);$$

$$dP3d\varphi := \frac{1}{2}\cdot k_1\cdot\big(\big(-2\cdot B\cdot C^2 + 2\cdot A\cdot C\cdot d\big)\cdot x + \big(-2\cdot B\cdot C\cdot d + 2\cdot A\cdot d^2\big)\cdot y + \big(2\cdot B^2\cdot C^2 - 4\cdot A$$

$$\cdot B\cdot C\cdot d + 2\cdot A^2\cdot d^2\big)\cdot\phi\big):$$

$$simplify(dP3d\varphi);$$

$$\big(0.01791\,\phi - 0.01745\,y + 0.99970\,x\big)\,k_1$$

$$\big(-0.00036\,\phi + 0.00030\,y - 0.01745\,x\big)\,k_1$$

(4)

$$(0.01792\,x - 0.00031\,y + 0.00032\,\phi)\,k_1 \tag{4}$$

```
> A := r·cos(β4) :
  B := r·sin(β4) :
  C := cos(α4) :
  d := sin(α4) :
  dP4dx := 1/2·k1·((2·C^2)·x + (2·C·d)·y + (-2·B·C^2 + 2·A·C·d)·φ) :
  simplify(dP4dx);
  dP4dy := 1/2·k1·((2·C·d)·x + (2·d^2)·y + (-2·B·C·d + 2·A·d^2)·φ) :
  simplify(dP4dy);
  dP4dφ := 1/2·k1·((-2·B·C^2 + 2·A·C·d)·x + (-2·B·C·d + 2·A·d^2)·y + (2·B^2·C^2 - 4·A
      ·B·C·d + 2·A^2·d^2)·φ) :
  simplify(dP4dφ);
```

$$(0.01628\,\phi - 0.01745\,y + 0.99970\,x)\,k_1$$

$$(-0.00028\,\phi + 0.00030\,y - 0.01745\,x)\,k_1$$

$$(0.01628\,x - 0.00028\,y + 0.00026\,\phi)\,k_1 \tag{5}$$

```
> dPdx := dP1dx + dP2dx + dP3dx + dP4dx :
  dPdx := evalf(dPdx) :
  simplify(dPdx);
  dPdy := dP1dy + dP2dy + dP3dy + dP4dy :
  dPdy := evalf(dPdy) :
  simplify(dPdy);
  dPdφ := dP1dφ + dP2dφ + dP3dφ + dP4dφ :
  dPdφ := evalf(dPdφ) :
  simplify(dPdφ);
```

$$3.99878\,k_1\,x$$

$$k_1\,(0.00122\,y - 0.00119\,\phi)$$

$$k_1\,(-0.00119\,y + 0.00117\,\phi) \tag{6}$$

```
>
>
```

The resulting equations of motion can be found below:

$$\begin{bmatrix} m & 0 & 0 \\ 0 & m & 0 \\ 0 & 0 & J \end{bmatrix} \begin{bmatrix} \ddot{x} \\ \ddot{y} \\ \ddot{\phi} \end{bmatrix} + k * \begin{bmatrix} 3.99878 & 0 & 0 \\ 0 & 0.00122 & -0.00119 \\ 0 & -0.00119 & 0.00117 \end{bmatrix} \begin{bmatrix} x \\ y \\ \phi \end{bmatrix} = \begin{bmatrix} \sum F_r \\ 0 \\ \sum M_r \end{bmatrix}$$

A.3.5. Update alphas

The derivation resulting in the coefficients that will be updated each iteration can be found below. They are an immediate result from the derivation presented in Subsection A.3.1.

$$\#\ Cxx := k_1 \cdot \left(\cos(\alpha_1)^2 + \cos(\alpha_2)^2 + \cos(\alpha_3)^2 + \cos(\alpha_4)^2\right);$$

$$\#\ Cxy := k_1 \cdot \left(\sin(\alpha_1)\cos(\alpha_1) + \sin(\alpha_2)\cos(\alpha_2) + \sin(\alpha_3)\cos(\alpha_3) + \cos(\alpha_4)\sin(\alpha_4)\right);$$

$$\#\ Cxphi := k_1 \cdot \left(-0.01710 \cdot \cos(\alpha_1)^2 - 0.04698 \cdot \sin(\alpha_1)\cos(\alpha_1) - 0.01710 \cdot \cos(\alpha_2)^2 + 0.04698 \cdot \sin(\alpha_2)\cos(\alpha_2) + 0.01710 \cdot \cos(\alpha_3)^2 - 0.04698 \cdot \sin(\alpha_3)\cos(\alpha_3) + 0.01710 \cdot \cos(\alpha_4)^2 + 0.04698 \cdot \cos(\alpha_4)\sin(\alpha_4)\right);$$

$$\#Cyx := k_1 \cdot \left(\sin(\alpha_1)\cos(\alpha_1) + \sin(\alpha_2)\cos(\alpha_2) + \sin(\alpha_3)\cos(\alpha_3) + \cos(\alpha_4)\sin(\alpha_4)\right);$$

$$\#\ Cyy := k_1 \cdot \left(-\cos(\alpha_1)^2 - \cos(\alpha_2)^2 - \cos(\alpha_3)^2 - \cos(\alpha_4)^2 + 4\right);$$

$$\#\ Cyphi := k_1 \cdot \left(0.04698 \cdot \cos(\alpha_1)^2 - 0.01710 \cdot \sin(\alpha_1)\cos(\alpha_1) - 0.04698 \cdot \cos(\alpha_2)^2 - 0.01710 \cdot \sin(\alpha_2)\cos(\alpha_2) + 0.04698 \cdot \cos(\alpha_3)^2 + 0.01710 \cdot \sin(\alpha_3)\cos(\alpha_3) - 0.04698 \cdot \cos(\alpha_4)^2 + 0.01710 \cdot \cos(\alpha_4)\sin(\alpha_4)\right);$$

$$\#\ Cphix := k_1 \cdot \left(-0.01710 \cdot \cos(\alpha_1)^2 - 0.04698 \cdot \sin(\alpha_1)\cos(\alpha_1) - 0.01710 \cdot \cos(\alpha_2)^2 + 0.04698 \cdot \sin(\alpha_2)\cos(\alpha_2) + 0.01710 \cdot \cos(\alpha_3)^2 - 0.04698 \cdot \sin(\alpha_3)\cos(\alpha_3) + 0.01710 \cdot \cos(\alpha_4)^2 + 0.04698 \cdot \cos(\alpha_4)\sin(\alpha_4)\right);$$

$$\#\ Cphiy := k_1 \cdot \left(0.04698 \cdot \cos(\alpha_1)^2 - 0.01710 \cdot \sin(\alpha_1)\cos(\alpha_1) - 0.04698 \cdot \cos(\alpha_2)^2 - 0.01710 \cdot \sin(\alpha_2)\cos(\alpha_2) + 0.04698 \cdot \cos(\alpha_3)^2 + 0.01710 \cdot \sin(\alpha_3)\cos(\alpha_3) - 0.04698 \cdot \cos(\alpha_4)^2 + 0.01710 \cdot \cos(\alpha_4)\sin(\alpha_4)\right);$$

$$\#\ Cphiphi := k_1 \cdot -0.01710 \cdot \left(0.11199 \cdot \cos(\alpha_1)^2 - 0.09397 \cdot \sin(\alpha_1)\cos(\alpha_1) + 0.11199 \cdot \cos(\alpha_2)^2 + 0.09397 \cdot \sin(\alpha_2)\cos(\alpha_2) + 0.11199 \cdot \cos(\alpha_3)^2 + 0.09397 \cdot \sin(\alpha_3)\cos(\alpha_3) + 0.11199 \cdot \cos(\alpha_4)^2 - 0.09397 \cdot \sin(\alpha_4)\cos(\alpha_4) - 0.51636\right);$$

The resulting equations of motion can be found below:

$$\begin{bmatrix} m & 0 & 0 \\ 0 & m & 0 \\ 0 & 0 & J \end{bmatrix} \begin{bmatrix} \ddot{x} \\ \ddot{y} \\ \ddot{\phi} \end{bmatrix} + k * \begin{bmatrix} C_{xx} & C_{xy} & C_{x\phi} \\ C_{yx} & C_{yy} & C_{y\phi} \\ C_{\phi x} & C_{\phi y} & C_{\phi\phi} \end{bmatrix} \begin{bmatrix} x \\ y \\ \phi \end{bmatrix} = \begin{bmatrix} \sum F_r \\ 0 \\ \sum M_r \end{bmatrix}$$

Appendix B

Numerical Model Code

```
In [1]: from scipy import signal
        import numpy as np
        import numpy.random as rnd
        import pandas as pd
        import matplotlib.pyplot as plt
        import matplotlib.animation as animation
        from matplotlib.patches import Circle
        from matplotlib.patches import Rectangle
        from matplotlib.patches import Arrow
        from IPython.display import display
        from datetime import date
        import random
        %matplotlib notebook
```

```
In [1]: #Input Parameters
        DeltaTimeSlip = 100                 #[Hz]
        DeltaTimeStick = 100                #[Hz]
        TimeExperiment = 10                 #[s]
        TimeExperimentSlip = 2              #[s]
        TimeExperimentStick = 20            #[s]
        Nwidth = 1                          #[-], width divided in Nwidth bits
        m  = 0.67                           #[kg] m1 in Nuus(2018)
        k  = 20.17                          #[N/m] k1 in Nuus (2018)
        r  = 0.05                           #[m]
        J  = m*r**2                         #[kg*m^2]
        g  = 9.81                           #[kg*m/s^2]
        mukin = 0.2086
        mustatic = 0.2815
        Fcrdyn = m*g*mukin                  #[N]
        Fcrstat = m*g*mustatic              #[N]
        vb = 0.05                           #[m/s]
```

```
In [4]: def Slip(Sys,Fcrdyn,xdot0,k,x0,t0,sigma,y0,phi0,ydot0,phidot0):

            IC = [x0,xdot0,y0,ydot0,phi0,phidot0]
            t = np.linspace(0,0.01,DeltaTimeSlip)
            u = np.zeros((len(t),2))
            AantalStukjes = 50
            Deltay = r/AantalStukjes

            for time in range(len(u[:,0])):
                krachtje = np.zeros(2*AantalStukjes)
                for j in range(AantalStukjes):
                    Drukje = sigma * rnd.standard_normal(1) + Fcrdyn/(np.pi*r**2)
                    Deltax = (2 * np.sqrt(r**2 - (Deltay*(j+1))**2)
                              + (np.sqrt(r**2 - (Deltay*(j))**2)
                                 - np.sqrt(r**2 - (Deltay*(j+1))**2)))
                    Oppervlakje = Deltay * Deltax
                    krachtje[j] = Drukje * Oppervlakje
                    arm = j*Deltay + 0.5*Deltay
                    u[time,1] += krachtje[j] * arm
                for j in range(AantalStukjes):
                    Drukje = sigma * rnd.standard_normal(1) + Fcrdyn/(np.pi*r**2)
                    Deltax = (2 * np.sqrt(r**2 - (Deltay*(j+1))**2)
                              + (np.sqrt(r**2 - (Deltay*(j))**2)
                                 - np.sqrt(r**2 - (Deltay*(j+1))**2)))
                    Oppervlakje = Deltay * Deltax
                    krachtje[j+AantalStukjes] = Drukje * Oppervlakje
                    arm = j*Deltay + 0.5*Deltay
                    u[time,1] -= krachtje[j+AantalStukjes] * arm
                u[time,0] = np.sum(krachtje)

            t1,x,StateVector1 = signal.lsim(Sys,u,t,IC)

            t1 = t1+t0
            x = np.zeros(len(t))
            xdot = np.zeros(len(t))
            y = np.zeros(len(t))
            ydot = np.zeros(len(t))
            phi = np.zeros(len(t))
            phidot = np.zeros(len(t))
            Indicator = np.zeros(len(t))

            for i in range(len(t)):
                x[i] = StateVector1[i,0]
                xdot[i] = StateVector1[i,1]
                y[i] = StateVector1[i,2]
                ydot[i] = StateVector1[i,3]
                phi[i] = StateVector1[i,4]
                phidot[i] = StateVector1[i,5]
```

```
            Indicator[i] = False
        demper = False
        return x, xdot, y, ydot, phi, phidot, u[:,0], u[:,1], t1, Indicator, demper
```

In [5]:
```
def Stick(vb,k,x0,t0,Fcrstat,y0,phi0):
    t = np.linspace(t0,t0+TimeExperimentStick,TimeExperimentStick*DeltaTimeStick)
    x = np.zeros(len(t))
    xdot = np.zeros(len(t))
    y = np.ones(len(t))*y0
    ydot = np.zeros(len(t))
    phi = np.ones(len(t))*phi0
    phidot = np.zeros(len(t))
    Fw = np.zeros(len(t))
    Indicator = np.zeros(len(t))
    for i in range(len(t)):
        x[i] = vb*(t[i]-t0) + x0
        xdot[i] = vb
        Fw[i] = k*x[i]
        Indicator[i] = True
        if Fw[i] >= Fcrstat:
            return (x[0:i], xdot[0:i], y[0:i], ydot[0:i], phi[0:i],
                    phidot[0:i], Fw[0:i], t[0:i], Indicator[0:i])
```

In [9]:
```
def Experiment(m,vb,k,cycli,mustatic,mukinetic,sigma):
    J = m * r * r
    Fcrstat = m * 9.81 * mustatic
    Fcrdyn = m * 9.81 * mukinetic
    sigma = sigma * (m*g/(np.pi*r**2))
    xlist = []
    x0list = []
    xdotlist = []
    ylist = []
    y0list = []
    ydotlist = []
    philist = []
    phi0list = []
    phidotlist = []
    tlist = []
    t0list = []
    Fwlist = []
    Indicatorlist = []
    xticks = []
    xSliplabels = []

    x,xdot,y,ydot,phi,phidot,Fw,t,Indicator = Stick(vb,k,0.0,0.0,
                                                    Fcrstat=Fcrstat, y0=0.0,
                                                    phi0=0.0)
    xlist.extend(x)
```

```
xdotlist.extend(xdot)
ylist.extend(y)
ydotlist.extend(ydot)
philist.extend(phi)
phidotlist.extend(phidot)
Fwlist.extend(Fw)
tlist.extend(t)
Indicatorlist.extend(Indicator)
t0 = tlist[-1]
t0list.extend([t0])
x0 = xlist[-1]
x0list.extend([x0])
xdot0 = xdotlist[-1]
y0 = ylist[-1]
y0list.extend([y0])
ydot0 = ydotlist[-1]
phi0 = philist[-1]
phi0list.extend([phi0])
phidot0 = phidotlist[-1]

y__1 = 0.0
y__2 = 0.0
y__3 = 0.0
y__4 = 0.0
lveer = 0.2 #[m] Length of the spring
N = 100

for i in range(cycli):
    for j in range(N):
        alpha__1 = np.arctan2(y__1,lveer)
        alpha__2 = np.arctan2(y__2,lveer)
        alpha__3 = np.arctan2(y__3,lveer)
        alpha__4 = np.arctan2(y__4,lveer)

        Cxx   = (np.cos(alpha__1)**2
                 + np.cos(alpha__2)**2
                 + np.cos(alpha__3)**2
                 + np.cos(alpha__4)**2)
        Cxy   = (np.cos(alpha__1)*np.sin(alpha__1)
                 + np.cos(alpha__2)*np.sin(alpha__2)
                 + np.cos(alpha__3)*np.sin(alpha__3)
                 + np.cos(alpha__4)*np.sin(alpha__4))
        Cxphi = (-0.01710*np.cos(alpha__1)**2
                 - 0.04698*np.cos(alpha__1)*np.sin(alpha__1)
                 - 0.01710*np.cos(alpha__2)**2
                 + 0.04698*np.cos(alpha__2)*np.sin(alpha__2)
                 + 0.01710*np.cos(alpha__3)**2
                 - 0.04698*np.cos(alpha__3)*np.sin(alpha__3)
```

```
          + 0.01710*np.cos(alpha__4)**2
          + 0.04698*np.cos(alpha__4)*np.sin(alpha__4))
Cyx    = (np.cos(alpha__1)*np.sin(alpha__1)
          + np.cos(alpha__2)*np.sin(alpha__2)
          + np.cos(alpha__3)*np.sin(alpha__3)
          + np.cos(alpha__4)*np.sin(alpha__4))
Cyy    = (-np.cos(alpha__1)**2-np.cos(alpha__2)**2
          -np.cos(alpha__3)**2-np.cos(alpha__4)**2+4)
Cyphi  = ( 0.04698*np.cos(alpha__1)**2 -
          0.01710*np.cos(alpha__1)*np.sin(alpha__1)
          - 0.04698*np.cos(alpha__2)**2
          - 0.01710*np.cos(alpha__2)*np.sin(alpha__2)
          + 0.04698*np.cos(alpha__3)**2
          + 0.01710*np.cos(alpha__3)*np.sin(alpha__3)
          - 0.04698*np.cos(alpha__4)**2
          + 0.01710*np.cos(alpha__4)*np.sin(alpha__4))
Cphix  = (-0.01710*np.cos(alpha__1)**2
          - 0.04698*np.cos(alpha__1)*np.sin(alpha__1)
          - 0.01710*np.cos(alpha__2)**2
          + 0.04698*np.cos(alpha__2)*np.sin(alpha__2)
          + 0.01710*np.cos(alpha__3)**2
          - 0.04698*np.cos(alpha__3)*np.sin(alpha__3)
          + 0.01710*np.cos(alpha__4)**2
          + 0.04698*np.cos(alpha__4)*np.sin(alpha__4))
Cphiy  = ( 0.04698*np.cos(alpha__1)**2
          - 0.01710*np.cos(alpha__1)*np.sin(alpha__1)
          - 0.04698*np.cos(alpha__2)**2
          - 0.01710*np.cos(alpha__2)*np.sin(alpha__2)
          + 0.04698*np.cos(alpha__3)**2
          + 0.01710*np.cos(alpha__3)*np.sin(alpha__3)
          - 0.04698*np.cos(alpha__4)**2
          + 0.01710*np.cos(alpha__4)*np.sin(alpha__4))
Cphiphi = (-0.01710*(0.11199*np.cos(alpha__1)**2
                     - 0.09397*np.cos(alpha__1)*np.sin(alpha__1)
                     + 0.11199*np.cos(alpha__2)**2
                     + 0.09397*np.cos(alpha__2)*np.sin(alpha__2)
                     + 0.11199*np.cos(alpha__3)**2
                     + 0.09397*np.cos(alpha__3)*np.sin(alpha__3)
                     + 0.11199*np.cos(alpha__4)**2
                     - 0.09397*np.cos(alpha__4)*np.sin(alpha__4)
                     - 0.51636))
A = [[      0.0, 1.0,       0.0, 0.0,         0.0, 0.0] ,
     [ -Cxx*k/m, 0.0,  -Cxy*k/m, 0.0,  -Cxphi*k/m, 0.0] ,
     [      0.0, 0.0,       0.0, 1.0,         0.0, 0.0] ,
     [ -Cyx*k/m, 0.0,  -Cyy*k/m, 0.0,  -Cyphi*k/m, 0.0] ,
     [      0.0, 0.0,       0.0, 0.0,         0.0, 1.0] ,
     [-Cphix*k/J, 0.0,-Cphiy*k/J, 0.0,-Cphiphi*k/J, 0.0]]
B = [[  0.0,   0.0] ,
```

```
      [1.0/m, 0.0/m] ,
      [  0.0,   0.0] ,
      [0.0/m, 0.0/m] ,
      [  0.0,   0.0] ,
      [0.0/J, 1.0/J]]
C = [[1.0,0.0,0.0,0.0,0.0,0.0],
      [0.0,0.0,1.0,0.0,0.0,0.0],
      [0.0,0.0,0.0,0.0,1.0,0.0]]
D = [[0.0,0.0],
      [0.0,0.0],
      [0.0,0.0]]
Sys = signal.StateSpace(A,B,C,D)

x, xdot, y, ydot, phi, phidot, Fw, M, t, Indicator, demper = Slip(Sys,
                                                                  Fcrdyn,
                                                                  xdot0,
                                                                  k,x0,t0,
                                                                  sigma,y0,
                                                                  phi0,
                                                                  ydot0,
                                                                  phidot0)

if xdot[-1] >= vb and N > 1:
    xlist.extend(x)
    xdotlist.extend(xdot)
    ylist.extend(y)
    ydotlist.extend(ydot)
    philist.extend(phi)
    phidotlist.extend(phidot)
    Fwlist.extend(Fw)
    tlist.extend(t)
    Indicatorlist.extend(Indicator)
    break
else:
    y__1 = np.sin(160/180*np.pi+phi[-1]) - np.sin(160/180*np.pi)
    y__2 = np.sin( 20/180*np.pi+phi[-1]) - np.sin( 20/180*np.pi)
    y__3 = np.sin(200/180*np.pi+phi[-1]) - np.sin(200/180*np.pi)
    y__4 = np.sin(340/180*np.pi+phi[-1]) - np.sin(340/180*np.pi)

    xlist.extend(x)
    xdotlist.extend(xdot)
    ylist.extend(y)
    ydotlist.extend(ydot)
    philist.extend(phi)
    phidotlist.extend(phidot)
    Fwlist.extend(Fw)
    tlist.extend(t)
    Indicatorlist.extend(Indicator)
```

```
                t0 = tlist[-1]
                x0 = xlist[-1]
                xdot0 = xdotlist[-1]
                y0 = ylist[-1]
                ydot0 = ydotlist[-1]
                phi0 = philist[-1]
                phidot0 = phidotlist[-1]

            if demper == True:
                return
            t0 = tlist[-1]
            t0list.extend([t0])
            x0 = xlist[-1]
            x0list.extend([x0])
            y0 = ylist[-1]
            y0list.extend([y0])
            phi0 = philist[-1]
            phi0list.extend([phi0])

            x,xdot,y,ydot,phi,phidot,Fw,t,Indicator = Stick(vb,k,x0,t0,Fcrstat,y0,phi0)

            xlist.extend(x)
            xdotlist.extend(xdot)
            ylist.extend(y)
            ydotlist.extend(ydot)
            philist.extend(phi)
            phidotlist.extend(phidot)
            Fwlist.extend(Fw)
            tlist.extend(t)
            Indicatorlist.extend(Indicator)

            t0 = tlist[-1]
            t0list.extend([t0])
            x0 = xlist[-1]
            x0list.extend([x0])
            y0 = ylist[-1]
            y0list.extend([y0])
            phi0 = philist[-1]
            phi0list.extend([phi0])

        xlist = np.array(xlist)
        tlist = np.array(tlist)
        xdotlist = np.array(xdotlist)
        ylist = np.array(ylist)
        ydotlist = np.array(ydotlist)
        philist = np.array(philist)
        phidotlist = np.array(phidotlist)


        Fwlist = np.array(Fwlist)
        Indicatorlist = np.array(Indicatorlist)


    return (xlist,xdotlist,ylist,ydotlist,philist,phidotlist,Fwlist,tlist,
            Indicatorlist,x0list,t0list)
```

Appendix C

Set-up Drawings

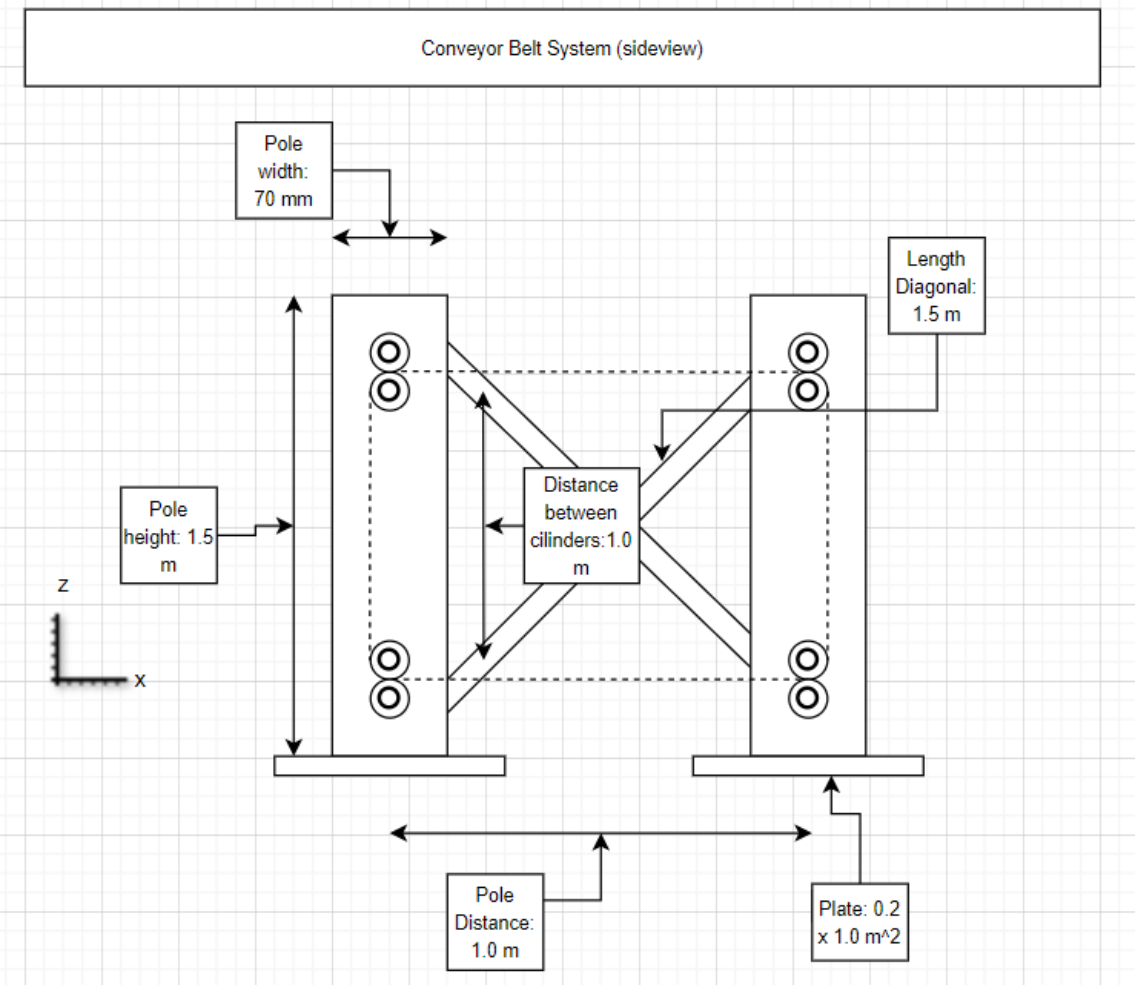

Figure C.1: Full dimensions of Conveyor Belt System

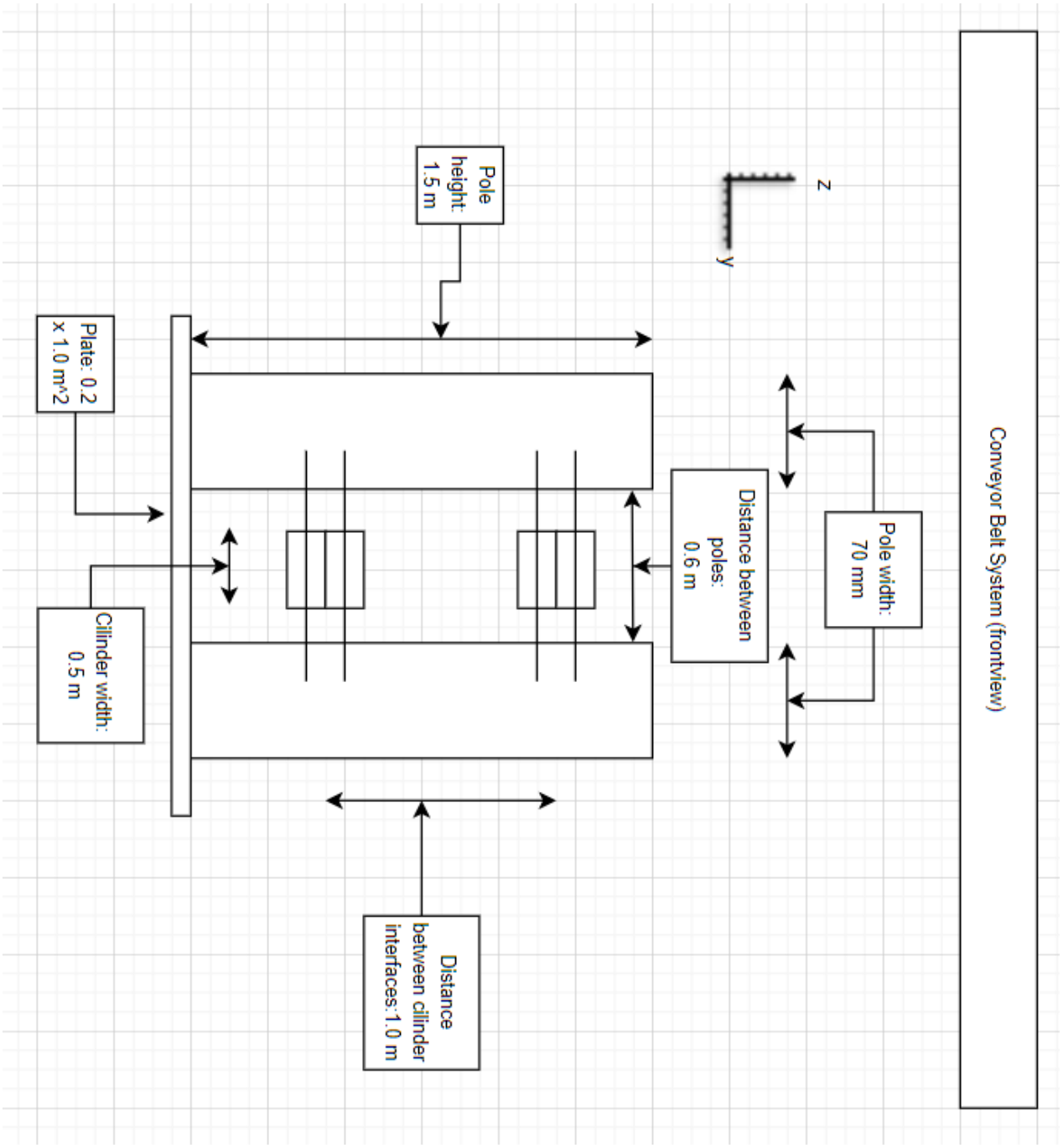

Figure C.2: Full dimensions of Poles holding the cylinders

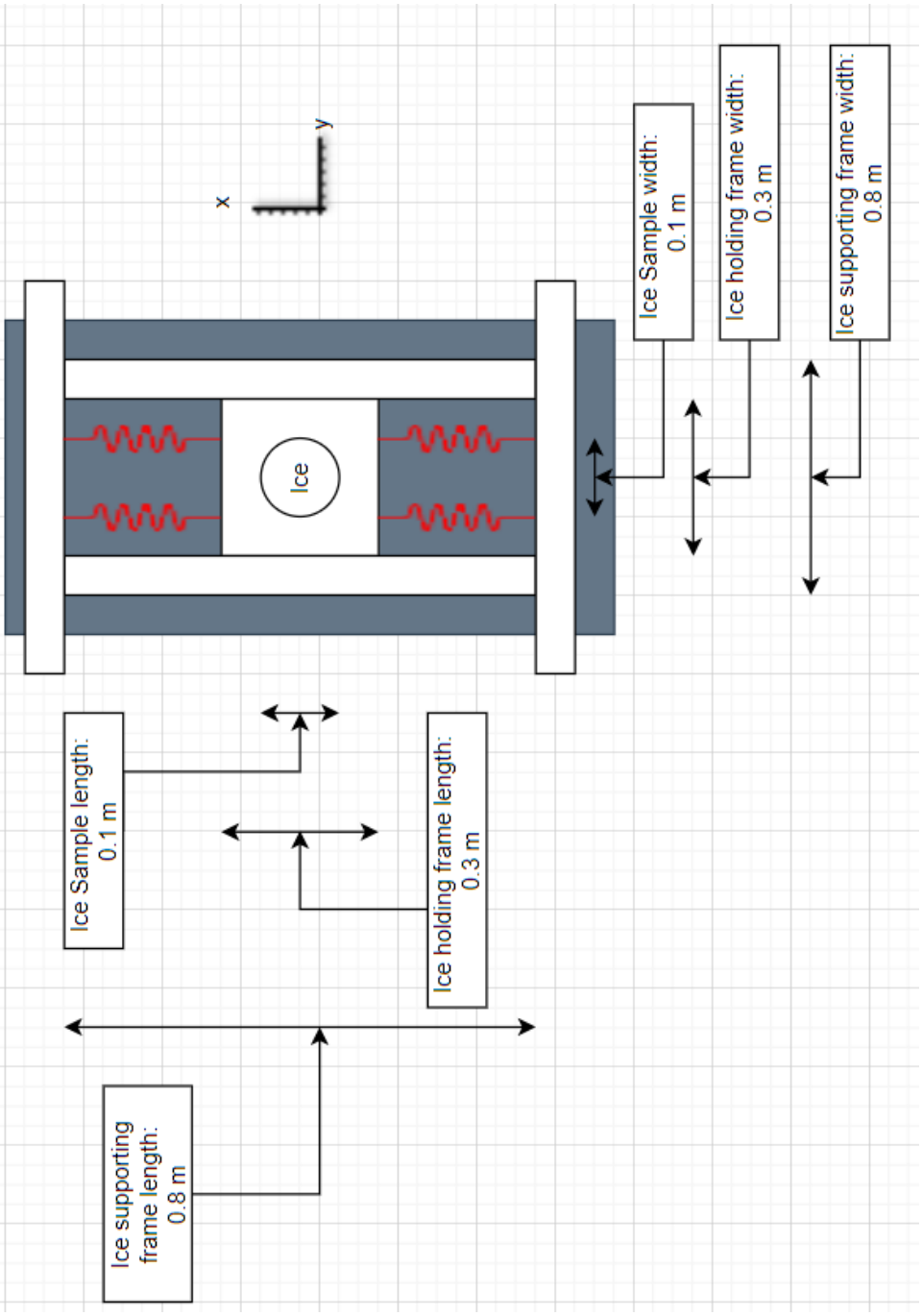

Figure C.3: Full dimensions of 1D Ice Holding Structure

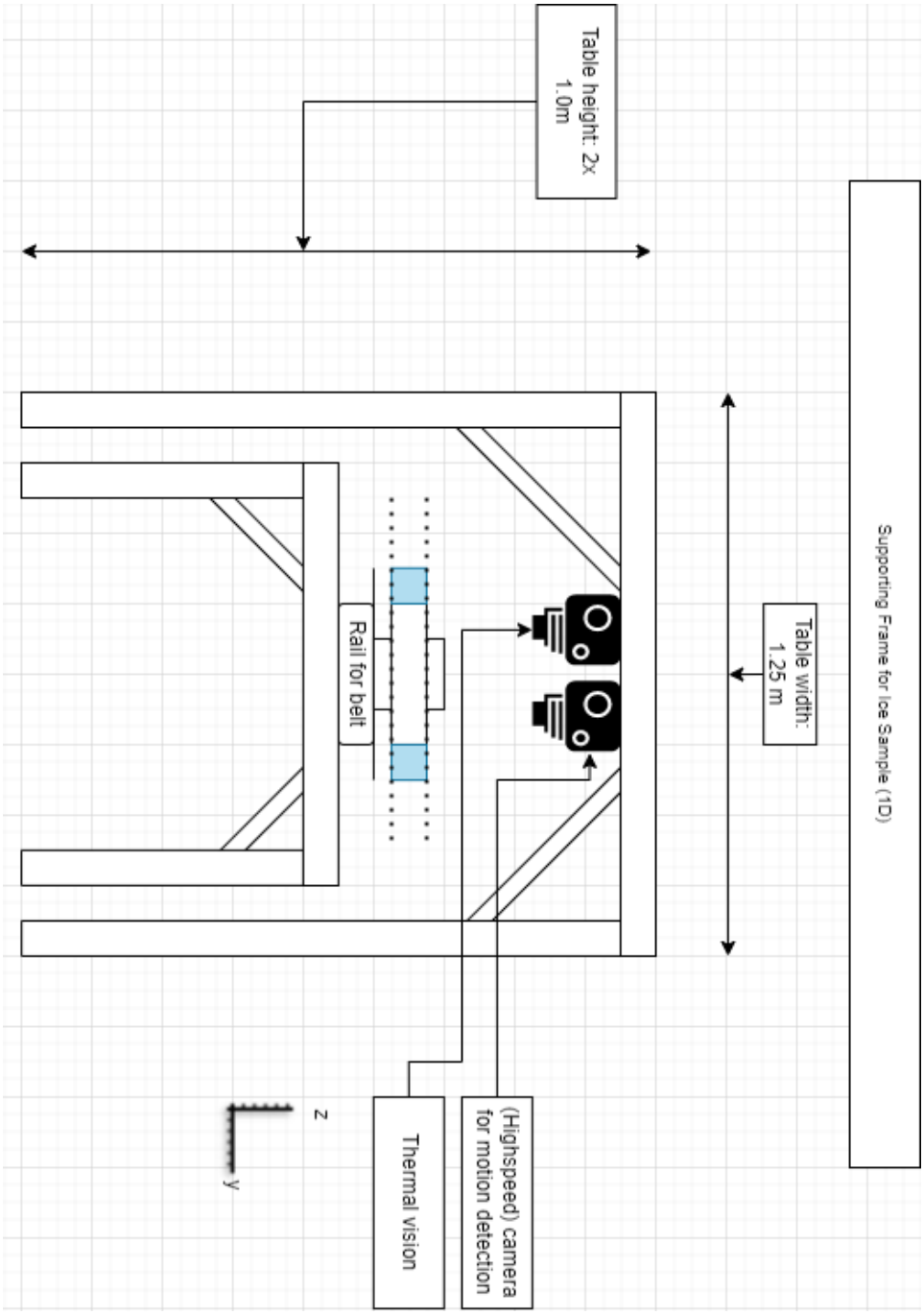

Figure C.4: Full dimensions of 1D and 2D Supporting Frame

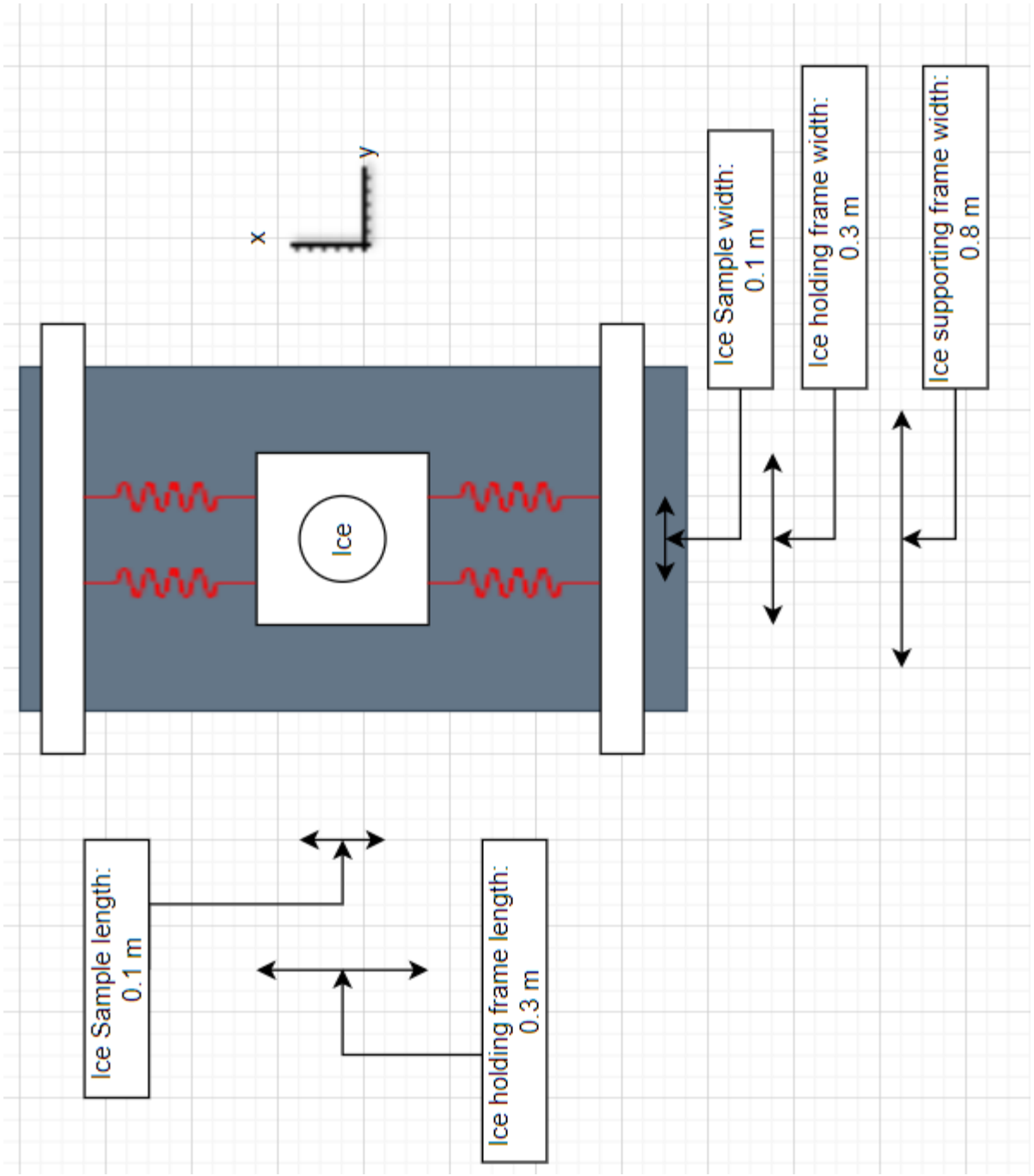

Figure C.5: Full dimensions of 2D Ice Holding Structure